Title
ELECTRONIC STRUCTURE AND DIELECTRIC PROPERTIES OF CUBIC SEMICONDUCTORS

Author
Walter, John P.

Publication Date
1970-11-01

UCRL-20377

C. 2

ELECTRONIC STRUCTURE AND DIELECTRIC PROPERTIES OF CUBIC SEMICONDUCTORS

John P. Walker
(Ph. D. Thesis)

November 1970

AEC Contract No. W-7405-eng-48

LAWRENCE RADIATION LABORATORY
UNIVERSITY of CALIFORNIA BERKELEY

UCRL-20377

DISCLAIMER

TABLE OF CONTENTS

ELECTRONIC STRUCTURE AND DIELECTRIC PROPERTIES OF CUBIC SEMICONDUCTORS

John P. Walter

Inorganic Materials Research Division, Lawrence Radiation Laboratory
and Department of Physics, University of California
Berkeley, California

ABSTRACT

The electronic structure and dielectric properties of various cubic semiconductors are explored using the empirical pseudopotential method. This thesis is concerned primarily with the semiconductors Si, Ge, GaAs, GaP, ZnS, ZnSe, and ZnTe, all of which have a face-centered cubic (zinc-blende) crystalline structure.

The empirical pseudopotential is discussed as the method exists today. The method is applied to the above semiconductors; the resultant electronic energy eigenvalues and wave-functions are used to examine several aspects of the electronic behavior of semiconductors. (1) The frequency dependence of the imaginary part of the dielectric function, of the reflectivity, and of the logarithmic derivative of the reflectivity are computed in order to analyze the optical properties of these crystals. The analysis allows the identification of the electronic transitions responsible for various peaks in the reflectivity spectra, and thus important information concerning the electronic band structure is obtained. (2) The effects of temperature changes on the reflectivity spectra are calculated for GaAs. The pressure coefficient for the fundamental gap is also calculated for this crystal. (3) The wave-vector-dependent dielectric function is calculated for Si,Ge, GaAs, and ZnSe along three symmetry lines. A comparison is made between the present results and the results of other calculations. An application of the results to the pseudopotentials of Si and Ge indicate the self-consistency of these

pseudopotentials. (4) Finally, the distribution of the valence electrons about the ion cores is calculated for Ge, GaAs, and ZnSe. The results are shown in contour plots of the electronic density. Trends in bonding and ionicity are studied for these crystals.

INTRODUCTION

A semiconducting crystal may be viewed as an orderly array of spherical ions surrounded by clouds of electrons. The inner electrons (the core electrons) are tightly bound and do not contribute significantly to the important physical and chemical properties of the crystal. Properties calculated in this thesis are reflectivity spectra, temperature shifts in the reflectivity spectra, the pressure dependence of the fundamental gap, the wave-vector-dependent and frequency-dependent dielectric functions, and the effective bonding charge densities. All of these properties are characterized by the fact that only the outer electrons, or valence electrons, contribute in a significant way. Accordingly, a method is chosen in which we need to explicitly calculate only the properties of the valence electrons. A pseudopotential represents the effective potential seen by a valence electron; it describes the interaction of a valence electron with the ion core and its surrounding cloud of valence electrons. This concept was first introduced by Phillips and Kleinman[1] and was justified theoretically by Cohen and Heine[2] and by Austin, Heine, and Sham.[3]

Several methods exist for determining pseudopotentials. They can be computed from free-atom term values,[4] from atomic wave-functions, or they may be obtained empirically from measurements of optical and dielectric properties of the crystal. This latter approach, the empirical pseudopotential method, has been successfully used to obtain fairly accurate band structures for many cubic semiconductors,[5] as well as for some hexagonal semiconductors.[6] A great deal of labor has been expended toward improving this method, by the author[7] and by other researchers,[8]

to obtain more accurate band structures for semiconductors, insulators, and metals.

In Chapts. I and II, the empirical pseudopotential method is discussed as the method exists today. The method is applied to Si, Ge, GaAs, GaP, ZnS, ZnSe, and ZnTe, all of which are semiconducting crystals with a face-centered cubic (zinc-blende) crystal structure. The resultant electronic energy eigenvalues and wave-functions are used to examine several aspects of the electronic behavior of semic-conductors. The frequency dependence of the imaginary part of the dielectric function $\varepsilon_2(\omega)$,of the reflectivity $R(\omega)$, and of the logarithmic derivative of the reflectivity, $R'(\omega)/R(\omega)$, are calculated and compared to experimental results in order to analyze the optical properties of these crystals. The analysis allows identification of the electronic transitions responsible for the major reflectivity peaks and thus yields important information concerning the electronic band structure.

In Chapt. III, the temperature and pressure effects are discussed with reference to GaAs. In particular, the effects of temperature changes on the reflectivity spectra are calculated, taking into account both thermal expansion of the lattice and thermal vibrations of the ion cores. The pressure coefficient of the fundamental gap is also calculated for GaAs.

In Chapt. IV, the wave-vector-dependent dielectric function is discussed and calculations are presented for Si,Ge GaAs, and ZnSe along various symmetry directions. A comparison is made between the present results and the results of other calculations. An application of the results to the largest pseudopotential form factors of Si and Ge indicate

the self-consistency of their potentials.

In Chapt. V, the distribution of the valence electronic charge density is calculated for the crystals, Si, Ge, GaAs, and ZnSe, Effective bonding charges are calculated and the electronic distribution is shown in contour plots.

CHAPTER I: PSEUDOPOTENTIAL CALCULATIONS WITHOUT SPIN-ORBIT INTERACTIONS

In this chapter the empirical pseudopotential method is discussed in the absence of spin-orbit interactions. In the next chapter spin-orbit interactions are included for those crystals in which it has a significant effect. The method discussed in this chapter is applicable in the next chapter. Only relatively simple changes in the method are necessary to give good results for crystals in which spin-orbit effects are included. The crystals considered in this chapter are GaAs, GaP, and ZnS. One of these semiconductors, GaAs, has significant spin-orbit splittings, and therefore the calculations are refined in Chapt. II.

Pseudopotential form factors for these crystals were first obtained by Cohen and Bergstresser[5] (CB) using the empirical pseudopotential method. These form factors were obtained by comparsion with the existing optical data.[5,9-12] New measurements of the optical properties have been made[13-19] since that time. The results of these measurements and a direct comparison between the experimental and theoretical $R(\omega)$ were used to make slight adjustments of the CB form factors.

Using a critical-point analysis, the optical structure can be identified in terms of interband transitions. The symmetries and positions in energy of the important critical points have been determined and their contributions to $\varepsilon_2(\omega)$ and $R(\omega)$ have been investigated.

A. Method of Calculation

The empirical pseudopotential method involves adjusting pseudopotential form factors to achieve good agreement with experimental results for the principal optical transitions. These form factors are then used to

determine the electronic energy bands on a fine mesh of points in the Brillouin zone. The Brillouin zone for the fcc lattice is a truncated octahedron. The zone and the principle symmetry points and lines are shown in Fig. 1.

The pseudopotential Hamiltonian has the form

$$H = \frac{-\hbar^2}{2m} \nabla^2 + V(\underset{\sim}{r}). \tag{1.1}$$

The weak pseudopotential $V(\underset{\sim}{r})$ is expanded in the reciprocal lattice

$$V(\underset{\sim}{r}) = \sum_{\underset{\sim}{G}} V(\underset{\sim}{G}) \exp(-i\underset{\sim}{G}\cdot\underset{\sim}{r}), \tag{1.2}$$

where $\underset{\sim}{G}$ is a reciprocal lattice vector. $V(\underset{\sim}{G})$ can be expressed as

$$V(\underset{\sim}{G}) = V^S(\underset{\sim}{G}^2) \cos \underset{\sim}{G}\cdot\underset{\sim}{\tau} + i\, V^A(G^2) \sin \underset{\sim}{G}\cdot\underset{\sim}{\tau}, \tag{1.3}$$

where $\underset{\sim}{\tau} = (a/8)(1,1,1)$ is the position of the metallic atom and $-\underset{\sim}{\tau}$ is the position of the non-metallic atom . V^S and V^A are equal to one-half the sum and one-half the difference, respectively, of the metallic and non-metallic potentials. In these calculations only the six form factors $V^S(3)$, $V^S(8)$, $V^S(11)$, $V^A(3)$, $V^A(4)$, and $V^A(11)$ are allowed to be non-zero; i.e., zero values are taken for $G^2 \geq 12$ and when the structure factors, $\cos \underset{\sim}{G}\cdot\underset{\sim}{\tau}$ and $\sin \underset{\sim}{G}\cdot\underset{\sim}{\tau}$, are zero.

The solution of (1.1), using the form factors in (1.3), allows a calculation of $E(\underset{\sim}{k})$ at many points in the Brillouin zone. This permits a calculation of the imaginary part of the dielectric function using

$$\varepsilon_2(\omega) = \frac{e^2\hbar^2}{3\pi m^2\omega^2} \sum_{c,v} \int \delta(E_c(\underset{\sim}{k}) - E_v(\underset{\sim}{k}) - \hbar\omega) |\langle U_{\underset{\sim}{k},v} | \nabla | U_{\underset{\sim}{k},c} \rangle|^2 \, d^3k, \tag{1.4}$$

where $U_{\underset{\sim}{k},v}$ and $U_{\underset{\sim}{k},c}$ are the periodic parts of the valence and conduction band wave functions and the integration is performed over the entire Brillouin zone. The summation is over the highest three valence bands

and the lowest six conduction bands. $\varepsilon_2(\omega)$ is calculated precisely as described by Saslow, et al.,[20] with the one modification that each cube is divided into 512 equal subcubes.

An analytic tail replaces the calculated $\varepsilon_2(\omega)$ for higher energies. This is done to account for the high energy transitions which are not represented in our nine band $\varepsilon_2(\omega)$ calculation. The tail function used is

$$\frac{\beta\omega}{(\omega^2 + \gamma^2)^2},$$

where $\gamma = 4.5$ eV and β is determined by continuity with $\varepsilon_2(\omega)$ at the energy where the transitions neglected in our band cut-off become important. The tail function begins at 8.85 eV for GaAs, 8.95 for GaP, and 10.95 for ZnS. A Kramers-Kronig transformation gives $\varepsilon_1(\omega)$; this function together with $\varepsilon_2(\omega)$ allows a calculation of the reflectivity $R(\omega)$.

The Cohen and Bergstresser pseudopotential form factors were used as the initial form factors. By the process described above, we calculated $\varepsilon_2(\omega)$ and $R(\omega)$ and then compared $R(\omega)$ with the experimental reflectivity. Much of the gross detail was the same and thus the most important identifications were easily made. By varying the form factors slightly we attempted to move the major peaks to agree more closely to experiment and to duplicate the finer structure. The CB form factors were constrained in the following way: the symmetric form factors for GaAs and ZnSe were made to agree with the Ge potential, which is in the same row of the Periodic Table; the GaP and ZnS symmetric form factors were set equal to an average of the Group IV elements corresponding to the rows involved, i.e., and average of Si and Ge. This constraint was relaxed when we made our "fine" adjustment of the form factors. The

largest variation between the CB form factors and those used in the present calculation is about 0.02 Ry. Form factors and lattice constants are shown in Table 1.

In order to shift the reflectivity peaks or shoulders in a predictable manner, we had to determine the transitions responsible for the major contributions to these structures. This was done by finding the energy of the desired peak or shoulder on the $\varepsilon_2(\omega)$ graph and then examining the contributions to ε_2 at that energy from the constituent interband transitions. When we had determined the interband transitions contributing the greatest amount, e.g., band 4 to band 5, we examined a table of energy differences for these bands throughout the Brillouin zone. Particular attention was given to locating critical points with energy in the vicinity of the energy of the optical structure, although volume effects and the relative size of the momentum matrix elements were also used to determine the probable origin of the structure; the ultimate test of the correctness of our labelling was to change the pseudopotential slightly, to note how the energy splitting changed at that transition point, and finally to see if the peak position changed by the same amount as the energy splitting. All of the prominent reflectivity structure was labelled by this procedure.

To further elucidate this procedure, let us examine the large $_2$ peak which occurs at 4.7 eV for GaAs. The value of $_2$ at that energy is 31.0. From our tables of interband transitions the major contributions to that peak are bands (4-5), 26.2, bands (3-5), 2.7, bands (4-6),1.4, with other bands contributing even smaller amounts. Thus transitions from bands (4-5) are almost totally responsible for this peak. An examination of the energy differences between bands 4 and 5 throughout the

Brillouin zone reveals that an M_2 critical point occurs along the Σ direction at 4.76 eV with large oscillator strength. Furthermore, we observe that if by varying the form factor slightly the energy splitting at that point is changed by an amount Δ, then the position of the ϵ_2 peak changes by Δ with insignificant error. We therefore conclude that the GaAs peak at 4.7 eV can be labelled by the transition $\Sigma_2 - \Sigma_1$.

For the determination of the form factors from the experimental data, six structural features of $R(\omega)$ are chosen as being particularly descriptive of that function. These structures include the basic gap and the major peaks. In order to determine how the form factors should be varied, we use the following expression:

$$E_i = E_i^\circ - \sum_{j=1}^{6} \frac{\partial E_i}{\partial F_j}^\circ (F_j - F_j^\circ) \qquad (1.5)$$

where F_j° are the six non-zero CB form factors and the E_i° are the six characteristic energy splittings. $(\partial E_i/\partial F_j)^\circ$ are the derivatives of the characteristic energy splittings with respect to the form factors, evaluated at the CB form factors. The E_i are the experimental characteristic splittings and the F_j are the new form factors. In practice this equation is useful only in the range $|F_j - F_j^\circ| \leq .01$ Ry. If we define $\Delta E_i \equiv E_i - E_i^\circ$, $\Delta F_j \equiv F_j - F_j^\circ$ and $A_{ij} \equiv (\partial E_i/\partial F_j)^\circ$, Eq. (1.5) may be written

$$\Delta E_i = \sum_{j=1}^{6} A_{ij} \Delta F_j, \quad \text{only if } |\Delta F_j| \leq .01. \qquad (1.6)$$

The terms ΔE_i are known and the terms A_{ij} can be easily calculated. This equation cannot be merely inverted because the ΔE_i are sufficiently large that for some j $|\Delta F_j| > .01$, and consequently the Eq. (1.6) no longer

correctly describes the situation. We therefore use a gradient projection method of nonlinear programming.[21] The function

$$P = \sum_{i=1}^{6} (\Delta E_i - \sum_{j=1}^{6} A_{ij} \Delta F_j)^2 W_i^2, \qquad (1.7)$$

where W_i^2 is a weighting factor for the ith characteristic splitting, is a measure of the goodness of the fit to the experimental points. P is minimized subject to the constraints $|\Delta F_j| \leq .01$. P must decrease if the matrix A is non-zero, but if P is still too large after this process is completed, the new form factors replace the old and the process is repeated. We have found it necessary to perform at least two iterations before satisfactory agreement is achieved between theory and experiment at the characteristic points. This procedure does not guarantee that P can be made equal to zero but after each iteration P can be no larger than the previous P. However, the final form factors do not necessarily constitute a unique solution to the problem.

B. Comparison of Optical Properties

The band structures in the principal symmetry directions and graphs of selected optical functions are shown in Figs. 2 - 12. Table I tabulates the pseudopotential form factors derived in this work. Tables II-IV tabulate the important critical points for the three compounds.

1. GaAs.

The threshold in $\varepsilon_2(\omega)$ at 1.46 eV is caused by $\Gamma_{15} - \Gamma_1$ transitions. The rise and peak in the 2.7 - 3.1 eV region corresponds to L_3-L_1 transitions at 2.69 eV and $\Lambda_3 - \Lambda_1$ transitions at 2.93 eV. The prominent peak at 4.7 eV is caused almost entirely by $\Sigma_2 - \Sigma_1$ transitions in the vicinity

of (.58, .58, 0) (units of $2\pi/a$). Some contribution comes from the shoulder on the left side of the peak; this shoulder is attributed to transitions $\Delta_5 - \Delta_1$ (M_o singularity) at 4.10 eV, $\Delta_5 - \Delta_1$ (M_1) at 4.23 eV, and $X_5 - X_1$ (M_1) at 4.34 eV. The (4-6) transitions are insignificant in their contribution relative to (4-5) transitions in the vicinity of this peak. The X_5-X_3 transitions at 4.59 eV and Γ_{15}-Γ_{15} transitions at 4.82 eV create no discernible structure. Changing the energy splittings for these transitions causes no noticeable change in the peak structure. The small peak at 5.7 eV is attributed to $\Delta_5 - \Delta_1$ (4-6) transitions at 5.69 eV. The last major peak at 6.35 eV is caused almost entirely by (4-6) transitions within the Brillouin zone in the vicinity (.57, .43, .29). Some contribution does come from L_3-L_3 transitions at 6.45 eV, but most of the contribution is from the volume effect. The shoulder at 6.5 eV is caused by Λ_3- Λ_3 transitions, and the last shoulder arises from a volume effect caused by (4-7) transitions.

Plots of both theoretical and experimental reflectivity appear in Fig. 4. The first peak after the small structure at threshold corresponds to the Λ peak occuring at 3.1 eV in $\varepsilon_2(\omega)$. The shoulder on the main peak in the reflectivity corresponds to the shoulder on the main ε_2 peak and in general each piece of structure in the reflectivity plot has its counterpart on the ε_2 plot, displaced by at most 0.25 eV. The experimental reflectivity shows a doublet peak at 2.90 eV and 3.14 eV which is attributed to spin-orbit splitting. In addition, this peak has greater magnitude than the theoretical peak. This can be attributed to exciton effects[22,23,24] which can occur at this band edge for all four compounds under consideration. Our theory does not take into account either spin-

orbit splitting or exciton effects. The agreement between theory and experiment in the vicinity of the main peak is excellent. A shoulder appears in both the experimental and theoretical reflectivity at 4.4 eV. Another shoulder in the theoretical reflectivity appears at 5.65 eV. This can be seen in the data of Greenaway[9] at 5.55 eV and Vishnubhatla and Woolley[18] at 5.45 eV. It is not present in the reflectivity of Ehrenreich and Phillip.[10] Beyond 6.0 eV the experimental reflectivity no longer shows the detailed structure which appears in the theoretical reflectivity.

The $\Delta R/R(\omega)$ spectrum is obtained from thermoreflectance measurements by Matatagui, et al.,[17] is compared with that obtained directly from a derivative of the theoretical reflectivity. (See Fig. 5).

2. GaP

The threshold in $\varepsilon_2(\omega)$ at 2.79 eV is caused by Γ_{15}-Γ_1 transitions. The rise and peak in the 3.4 - 4.0 eV region corresponds to L_3-L_1 transitions at 3.40 eV and Λ_3-Λ_1 transitions at 3.76 eV. The prominent peak at 5.1 eV is caused almost entirely by Σ_2-Σ_1 transitions in the vicinity of (.50, .50, 0). Some contribution comes from the shoulder on the left side of the peak. This shoulder is attributed to transitions X_5-X_1 at 4.57 eV, Δ_5-Δ_1 (M_o) at 4.50 eV, and Δ_5-Δ_1 (M_1) at 4.72 eV. Just as for GaAs, the (4-6) transitions are negligible compared to the (4-5) transitions in the vicinity of this peak. X_5-X_3 transitions at 4.96 eV and Γ_{15}-Γ_{15} transitions at 5.23 eV create no discernible structure. The peak at 6.5 eV is caused by (4-6) transitions in a volume with center at (.50, . 43, .29). The L_3-L_3 transitions at 6.57 eV also contribute to this peak; however, varying the energy splitting in the vicinity of

(.50, .43, .29) has considerably greater influence in changing the position of the peak than does a change in the L_3-L_3 energy splitting. The small peak at 6.7 eV is attributed to Λ_3-Λ_1 transitions. The shoulder at 7.3 eV is a volume effect caused by (4-7) transitions.

The experimental reflectivity shows an exciton-enhanced peak at 3.7 eV, in good agreement with the theoretical peak at 3.7 eV. The experimental data exhibits a shoulder at 4.6 eV, which corresponds to the theoretical result of 4.7 eV. The major peak occurs at the same energy for both experiment and theory, but the peak heights disagree somewhat. The experimental peak at 6.9 eV corresponds to the theoretical peaks at 6.6 and 6.9 eV. The shoulder in the experimental data at 7.4 eV corresponds to the theoretical peak at 7.5 eV.

A comparison of $\Delta R/R(\omega)$ and the thermoreflectance measurements appears in Fig. 9.

3. ZnS

The threshold in $\varepsilon_2(\omega)$ is caused by Γ_{15}-Γ_1 transitions at 3.74 eV. The rise and peak in the 5.4 - 5.7 eV region is caused by L_3 - L_1 transitions at 5.40 eV and Λ_3-Λ_1 transitions at 5.52 eV. The principal contributions to the peak at 7.0 eV comes from Σ_2 - Σ_1 transitions at 7.08 eV located near (.54, .54, 0.) and from Δ_5-Δ_1 transitions at 6.99 eV located near (.50, 0., 0.). The X_5-X_1 transitions at 6.31 eV also contribute to the peak, causing the slight bulge at 6.5 eV. The small peak at 7.5 eV is caused by (4-6) transitions in the Δ direction at 7.45 eV and 7.57 eV. The peak subsides with Γ_{15}-Γ_{15} transitions at 7.79 eV. The peak at 8.35 eV is caused by (4-6) transitions in a volume centered at (.57, .36, .14). Although L_3-L_3 transitions also occur at 8.35 eV,

changing the energy splitting has negligible effect on the peak, whereas changing the splitting in the vicinity of (.57, .36, .14) does change the position of the peak by an amount equal to the change in the splitting. The peak at 8.65 eV is caused principally by (3-6) transitions in the Λ direction. The next two pieces of structure at 8.85 and 9.5 eV are attributed to (3-6) and (4-7) volume transitions.

The data of Cardona and Harbeke[12] and of Baars[15] show a small peak at 3.7 eV. The theoretical counterpart is a bump at 3.8 eV. The experimental data shows an exciton-enhanced peak at 5.8 eV. The theoretical peak occurs at 5.6 eV, giving only fair agreement with experiment. The main theoretical peak occurs at 7.05 eV; the measured value is 6.99 eV[12] and 7.02 eV.[15] Shoulders appear in the experimental data at 7.4 and 7.9 eV for Cardona and Harbeke and at 7.5 eV for Baars. The corresponding theoretical shoulder occurs at 7.55 eV. Cardona and Harbeke find a 7.9 eV shoulder which does not appear in the theoretical results or in Baars' data, so it must remain unexplained for the present. Baars' data exhibits peaks at 8.35, 9.0, and 9.6 eV, which are in good agreement with the theoretical peaks at 8.45, 9.15, and 9.75 eV. The data of Cardona and Harbeke has only one peak in this region at 9.8 eV.

C. Discussion of Results

Good agreement has been obtained between measured and calculated reflectivity and between $R'(\omega)/R(\omega)$ and thermo-reflectance. The agreement appears good enough to indicate the identifications of the important transitions are substantially correct and that the band structure is accurate in the region near the fundamental gap.

The results for GaAs and GaP are good. One point that should be discussed in detail is that in the calculations for GaAs and GaP, the shoulder on the low energy side of the main Σ peak $\varepsilon_2(\omega)$ is caused by (4-5) transitions along Δ and at X, and that the Γ_{15}-Γ_{15} transitions do not contribute significantly. A careful study of our band structure reveals that it is consistent with photoemission yield data for GaAs[16,25] As the vacuum level[25] is lowered, the first small peak is caused by (4-6) transitions at 4.60 eV along Σ at (.15, .15, 0.). The photoemission yield peak becomes larger and shifts its center from 4.65 to 4.50 eV because of (4-6) transitions along Δ (with an average energy of 4.4 eV) and the beginning of massive (4-5) transitions along both Δ and Σ. Eden[16] estimates that Γ_{15}-Γ_{15} lies in the range of 4.6 to 4.8 eV for GaAs, in good agreement with our value of 4.8 eV, and he estimates a value in the range of 4.8 to 5.2 eV for GaP, as compared with our value of 5.2 eV. If we allow for a small spin-orbit splitting of bands 3 and 4 along the Δ direction, our band structure is also consistent with the electroreflectance measurements of Thompson, et al.[13]

For ZnS the fitting procedure was difficult because the experiments differ by a fair amount. In fact, the differences between experiments is greater than that between the theory and either experiment. The agreement is only fair.

For all three crystals the caclulated reflectivity at high energies has greater magnitude than the measured reflectivity. Assuming the experimental measurements are accurate in this region, one possibility is that the pseudowave-functions might not give accurate oscillator strengths at higher energies. Another possibility is that the high-

energy set of calculated ε_2 peaks (located at 6-7 eV for GaAs and GaP and at 8-10 eV for ZnS) should be smaller in magnitude and smeared over a slightly larger area, which might occur if we were to include indirect transitions and life-time effects. (The steep slope followed by the small magnitude of $\varepsilon_2(\omega)$ on the high-energy side of these peaks is essentially what causes the high reflectivity.)

A comparison shows that the pseudopotentials for gallium and zinc are in reasonable agreement with the model potentials of Animalu and Heine.[4] The agreement is not precise because our pseudopotential takes into account crystalline effects and is constrained equal to zero for $G^2 \geq 12$.

CHAPTER II: PSEUDOPOTENTIAL CALCULATIONS WITH SPIN-ORBIT INTERACTIONS

In this chapter the empirical pseudopotential method is extended to those crystals in which spin-orbit interactions are significant. The semiconductors considered in this chapter are ZnTe, ZnSe, and GaAs. Although the spin-orbit effects in Si are small, Si is discussed in conjunction with GaAs because of the similarity of the experimental measurements on these two crystals.

Pseudopotential form factors for these crystals were originally obtained by Cohen and Bergstresser[5] by comparison of their band structure with the existing optical data.[5,11,26] Refined measurements of the optical properties[17,27-29] have since been made. The results of these measurements and a direct comparison between the experimental and the theoretical $R(\omega)$ (for ZnTe and ZnSe) and $R'(\omega)/R(\omega)$ (for GaAs and Si) were used to make small adjustments in the form factors. The spin-orbit form factor was determined by adjusting the valence band splitting at Γ_{15} to agree with the experimental value.

A. Method of Calculation

The pseudopotential form factors are initially adjusted by the procedure described in Chapt. I. Only slight over-all adjustments are necessary, as can be seen by comparing Table I with the pseudopotentials of Ref. 5.

In the initial adjustment, one must consider carefully the effects that spin-orbit splitting will have on the band structure and the resulting optical properties. A comparison of the band structure of GaAs, without and with spin-orbit interactions, is shown in Figs. 2 and 13, respectively.[30] When the spin-orbit parameter is added to the calculation,

the three bands at Γ split apart by an energy Δ_o, the top two moving upwards by 1/3 Δ_o and band 2 moving downwards by $2/3\Delta_o$. Accordingly, in the spin-free calculation the $\Gamma(4\text{-}5)$ splitting must be fitted to the experimental value plus one-third of Δ_o. Similarly, the Λ (4-5) splitting (near L) must be fitted to the experimental value plus one-half the spin-orbit splitting at L, which is denoted by Δ_1. In the case of GaAs, the effect of this procedure for fitting is most noticeable for the peak at about 3 eV (Figs. 4 and 5). The theoretical Λ peak lies halfway in energy between the two experimentally measured spin-orbit split peaks. More subtle effects must be considered in the splitting of the Δ peaks in the vicinity of 4.5 eV. The choice of this method of first fitting for the spin-free case and then adding spin-orbit interactions is made necessary by the great amount of computer time used in spin-orbit calculations.

In adding spin-orbit interactions we use the model introduced by Weisz[31] for white tin and modified by Bloom and Bergstresser[32] for grey tin, CdTe, and InSb. The Hamiltonian matrix element in the plane wave representation is

$$\begin{aligned}\langle \underset{\sim}{k}+\underset{\sim}{G}', s' |\mathcal{H}| \underset{\sim}{k}+\underset{\sim}{G}, s\rangle &= (2m)^{-1} |\underset{\sim}{k}+\underset{\sim}{G}|^2 \delta_{\underset{\sim}{G}',\underset{\sim}{G}}\delta_{s',s} \\ &+ S^S(\underset{\sim}{G}-\underset{\sim}{G}')\left[V^S(|\underset{\sim}{G}-\underset{\sim}{G}'|^2)\,\delta_{s',s} - i\lambda^S(\hat{k+G'}\times\hat{k+G})\cdot\underset{\sim}{\delta}_{s',s}\right] \\ &+ iS^A(\underset{\sim}{G}-\underset{\sim}{G}')\left[V^A(|\underset{\sim}{G}-\underset{\sim}{G}'|^2)\delta_{s',s} - i\lambda^A(\hat{k+G'}\times\hat{k+G})\cdot\underset{\sim}{\delta}_{s',s}\right]\end{aligned} \qquad (2.1)$$

S^S and S^A are the symmetric and antisymmetric structure factors and V^S and V^A are the symmetric and antisymmetric pseudopotentials (See Ref. 5). λ^S and λ^A are defined as follows:

$$\lambda^S = 1/2(\lambda_1+\lambda_2), \quad \lambda^A = 1/2(\lambda_1-\lambda_2). \tag{2.2}$$

$$\lambda_1 = \mu\, B_{n\ell}(G)\, B_{n\ell}(G') \quad \text{and} \quad \lambda_2 = \alpha\,\mu\, B_{n\ell}(G)\, B_{n\ell}(G') \tag{2.3}$$

where λ_1 and λ_2 are the metallic and non-metallic contributions, the $B_{n\ell}$ are the orthogonalization integrals for the metal in λ_1 and for the non-metal in λ_2, μ is the spin-orbit parameter, and α is the ratio of the non-metallic contribution to the metallic contribution for $\underset{\sim}{G} = \underset{\sim}{G}' = 0$.[33] The $B_{n\ell}$ are defined as follows:

$$B_{n\ell}(k) = C \int_0^\infty j_\ell(kr)\, R_{n\ell}(r)\, r^2\, dr, \tag{2.4}$$

where C is determined by the conditions

$$\lim_{k\to 0} k^{-\ell} B_{n\ell}(k) = 1, \tag{2.5}$$

and the $R_{n\ell}$ are tabulated Hartree-Fock-Slater orbitals.[33] In our calculation $n\ell$ is 3p for Zn and Se and 4p for Te. The d contributions are neglected, as well as contributions from lower-lying p states.

The spin-orbit parameter μ is varied to give the correct splitting of the valence band at Γ_{15}. This splitting is denoted by Δ_0. The experimental values of Δ_0 are 0.93, 0.45, 0.35 and 0.04 eV for ZnTe, ZnSe, GaAs and Si, respectively.[5,34] The spin-orbit splittings we obtain are shown in Table V.

The calculation of $\epsilon_2(\omega)$, the addition of the tail function, and the calculation of $R(\omega)$ are all performed as described in Chapter I.

B. Comparison of Optical Properties of ZnTe and ZnSe

The band structures in the principal symmetry directions and graphs of selected optical functions are shown in Figs. 14-21. Table I lists the form factors derived in this thesis, and Table V presents the

important critical points for ZnTe and ZnSe.

1. ZnTe

The threshold in $\varepsilon_2(\omega)$ at 2.21 eV is caused by $\Gamma_8 - \Gamma_6$ transitions. $\Gamma_7 - \Gamma_6$ transitions at 3.14 eV cause a slight rise in ε_2, but it is of the same magnitude as fluctuations at 2.60 eV and 3.25 eV. The start of the rise at 3.45 eV is caused by L_4, $L_5 - L_6$ (M_0) transitions at 3.45 eV. The first peak at 3.7 eV corresponds to $\Lambda(8\text{-}10)(M_1)$ transitions[35] at 3.64 eV. The rise and peak in the 4.05 - 4.27 eV region correspond to $L_6 - L_6(M_0)$ transitions at 4.03 eV and $\Lambda(6\text{-}10)M_1$ transitions at 4.21 eV. The small bulge at 4.58 eV is caused by $X_7 - X_6(M_0)$ transitions at 4.59 eV. The shoulder at 4.92 eV is caused by $\Delta(8\text{-}10)$ M_1 transitions at 4.93 eV. Another small bulge at 5.10 eV is caused by $X_6 - X_6(M_0)$ transitions at 5.05 eV. The main peak is slightly split into two peaks at 5.22 eV and 5.32 eV and is caused chiefly by transitions (7-9), (7-10), (8-9), and (8-10) along the Σ and Δ directions. In particular the peak at 5.22 eV is caused by (8-9) transitions in a volume near K. The peak at 5.32 eV is caused by (7-10) transitions in a volume near K, with $\Delta(6\text{-}10)$ (M_1) transitions at 5.39 eV and $\Sigma(7\text{-}10)(M_2)$ transitions at 5.50 eV contributing to a smaller extent. The shoulder at 6.07 eV is caused by $\Delta(6\text{-}12)(M_2)$ transitions at 6.13 eV. The peak at 6.72 eV is caused by (7-12) and (8-11) transitions, both located in a volume centered at (0.6, 0.4, 0.3) (units of $2\pi/a$). The peak at 7.28 eV is caused by (6-11) transitions in a volume centered at (0.6, 0.4, 0.3). The peak at 7.57 eV is caused by (5-12) transitions in a volume centered at (0.6, 0.4, 0.3). The shoulder at 7.57 eV is caused by $\Lambda(6\text{-}13)(M_2)$ transitions at 7.57 eV. The peak at 7.82 eV is caused by (6-13) transitions in a volume centered at

(0.5, 0.3, 0.1).

A comparison of $\varepsilon_2(\omega)$ with and without spin-orbit contributions shows the principal consequences of "turning off" the spin-orbit interaction. (Fig. 15). For the spin-free ε_2, the threshold occurs $1/3\Delta_0$ higher in energy. The two Λ peaks at 3.72 eV and 4.27 eV move together to form one Λ peak at 4.02 eV. The Δ transitions at 4.93 eV and 5.39 eV move together to form the main peak at 5.22 eV. The transitions near K move to 5.35 eV and the Σ transitions at 5.38 eV and 5.50 eV move to 5.48 eV to cause the shoulder at 5.42 eV. Δ transitions at 5.67 (barely discernible shoulder in the spin ε_2) and at 6.13 move together to form the peak at 6.78 eV. In addition, the bending of the bands when the interaction is turned off introduces a critical point in the Λ direction which contributes a major portion to the 6.78 eV peak. The (6-11) and (5-12) transitions in the vicinity of (0.6, 0.4, 0.3) move together at 7.22 eV and the Λ transition at 7.57 eV also moves to 7.24 eV.

The experimental and theoretical reflectivity at 300°K appear in Fig. 16, and details of the reflectivity structure are shown in Table VI. The theoretical Λ peak at 3.70 eV corresponds to the experimental peak at 3.58 eV. The second Λ peak at 4.30 eV corresponds to the experimental peak at 4.18 eV. A small shoulder appears on the low-energy side of the peak for both theory and experiment. The shoulder at 4.65 eV does not appear in the experimental reflectivity. The shoulder at 4.95 eV is caused by Δ(8-10) transitions and corresponds to the experimental shoulder at 4.92 eV. The shoulder at 5.25 eV does not appear in the experimental measurements 300°K. The main peak occurs at 5.45 eV for theory and at 5.51 eV for experiment. The experimental reflectivity from 5.6 eV to 6.5 eV

is remarkably linear, except for a practically imperceptible bulge at 5.9 eV. The calculated $R(\omega)$ has slight shoulders at 5.85 eV and 6.10 eV. The next peak occurs at 6.85 eV for theory and at 6.87 eV for experiment, but the two differ considerably in amplitude. The next peak occurs at 7.65 eV for theory and 7.58 eV for experiment. The theoretical $R(\omega)$ shows two shoulders at 7.35 eV and 7.55 eV which do not appear in the experiment. The last theoretical peak shows absolutely no correlation with experiment; it is caused by the steep negative slope of $\varepsilon_2(\omega)$ in the region 7.9-8.6 eV. The amplitude of the theoretical $R(\omega)$ in this region is considerably greater than that of the experimental $R(\omega)$; this will be discussed in more detail later. However, the overall agreement between experiment and theory, especially with regard to peak positioning, is good for ZnTe.

A comparison of $R'(\omega)/R(\omega)$ and thermo-reflectance data appears in Fig. 17.

2. ZnSe

The threshold in $\varepsilon_2(\omega)$ at 2.77 eV is caused by Γ_8-Γ_6 transitions. Γ_7-Γ_6 transitions at 3.22 eV cause a slight rise in ε_2. The start of the rise at 4.57 eV is caused by L_4, L_5-$L_6(M_0)$ transitions at 4.53 eV. The peak at 4.72 eV is caused by $\Lambda(8\text{-}10)(M_1)$ transitions at 4.64 eV. The rise and peak in the 4.75 eV to 5.02 eV region corresponds to L_6-$L_6(M_0)$ transitions at 4.82 eV and $\Lambda(6\text{-}10)M_1$ transitions at 4.94 eV. These are the two spin-orbit split Λ peaks. The start of the rise of the main peak is caused by X_7-$X_6(M_0)$ transitions at 5.92 eV. A small bulge at 6.2eV corresponds to $\Delta(8\text{-}10)(M_1)$ transitions at 6.11 eV. The slight shoulder at 6.6 eV is caused by $\Sigma(7\text{-}9)$ and $\Sigma(8\text{-}10)(M_2)$ transitions at 6.62 eV. The sum of the $\Delta(8\text{-}10)$, $\Sigma(7\text{-}9)$, and $\Sigma(8\text{-}10)$ transitions, plus that of $\Delta(6\text{-}10)$ transitions

at 6.37 eV causes the main peak at 6.42 eV. The next two peaks are spin-orbit split Δ peaks; the one at 7.07 eV is caused by $\Delta(8\text{-}12)(M_1)$ transition at 7.02 eV and the one at 7.32 eV is caused by $\Delta(6\text{-}12)(M_1)$ transitions at 7.28 eV. The shoulder at 7.63 eV is attributed to $\Sigma(6\text{-}12)(M_2)$ transitions at 7.60 eV. The peak at 8.13 eV is caused by (8-12) and (7-11) transitions, both in a volume centered at (0.6, 0.5, 0.2). The small peak at 8.52 eV is attributed to L(8-12) transitions at 8.51 eV. The peak at 8.77 eV is caused by (5-12), (6-11), (5-11), and (6-12) transitions, all centered at (0.6, 0.5, 0.2). Λ(8-14) transitions at 8.69 eV also contribute. The shoulder at 9.27 eV is caused by (5-14) and (6-13) transitions from a volume centered at (0.5, 0.2, 0.1).

If the spin-orbit interaction is turned off (Fig. 19), the threshold for $\varepsilon_2(\omega)$ occurs 1/3 Δ_0 higher in energy. The two Λ peaks at 4.72 eV and 5.02 eV move togehter. The base of the main peak on its low-energy side becomes narrower because of the bands at X are not as flat. The Δ(8-10) and Δ(6-10) transitions move together causing the main peak to become larger and also serving to narrow the base of the main peak on its low-energy side. The Δ(8-12) peak at 7.07 eV and the Δ(6-12) peak at 7.32 eV also move together. The strength of the Γ transitions at 7.9 eV becomes less because the bands are not as flat. Finally, the small L peak at 8.51 eV moves to a slightly higher energy at 8.65 eV.

The experimental and theoretical reflectivity at 300°K appear in Fig. 20, and details of the reflectivity structure are shown in Table VII. Excellent agreement exists between experiment and theory in the range 4.2 eV to 5.9 eV. The experimental peak at 6.0 eV corresponds to a slight bulge in the theoretical $R(\omega)$, which is caused by X_7-X_6 transi-

tions. The main peak has the same shape and peak positions agree, but the amplitudes differ. The next two experimental shoulders agree in positioning with theory, but the theoretical structure looks somewhat different. The Σ peak at 7.67 eV could also be the cause of the 7.60 eV experimental shoulder. The bands did flatten somewhat at Γ to produce a broader valley at 7.9 eV, but it did not duplicate the experimental peak at 7.8 eV.

The identifications in the region 8.0 eV to 10.0 eV are speculative because the shapes of the experimental and theoretical peaks do not agree. The experimental $R(\omega)$ structures at 8.28 eV and 8.46 eV are attributed to volume transitions near L from bands 7 and 8 to bands 11 and 12. The experimental structures at 8.97 eV and 9.25 eV are attributed to volume transitions centered at (0.6, 0.5, 0.2) from bands 5 and 6 to bands 11 and 12. The experimental peak at 9.7 eV is attributed to volume transitions centered at (0.5, 0.2, 0.1) from bands 5 and 6 to bands 13 and 14.

The agreement between theory and experiment is excellent between 4.2 eV and 7.8 eV. The agreement becomes progressively worse for higher energies.

A comparison of $R'(\omega)/R(\omega)$ and thermo-reflectance data appears in Fig. 21.

3. Low Temperature Reflectivity

The reflectivity for ZnTe and ZnSe at 15°K (Fig. 21) differs in several respects from the room temperature reflectivity. Certain of the peaks are greater in magnitude; all peaks are positioned at higher energies and the resolution of the spectrum is slightly better. For both crystals the Λ doublet is much sharper and larger in magnitude at low temperatures.

This phenomenon occurs in other similiar semicon ductors such as GaAs, GaSb,InAs, InSb, and Ge.[29,37] The Λ doublet is significantly greater in amplitude than it is possible to achieve in the theoretical calculations. This low-temperature sharpening is thought to be caused by exciton effects. Moreover, electro-reflectance line shapes also indicate exciton effects at Λ.[24] Thus the sharpening of the Λ doublet may be explained in terms of the reduction of lifetime broadening of the hyperbolic excitons associated with Λ. No other clear evidence of exciton effects can be seen in the reflectivity. The Σ peaks do become slightly larger at low temperatures, but the sharpening is not sufficient to indicate the presence of excitons.

The general increase in the energies of the reflectivity peaks at low temperature can easily be explained in terms of contraction of the lattice and the Debye-Waller effect. Both of these effects cause the effective electronic potential to become stronger at low temperatures, which causes the spacing between energy bands to increase and the positions of the peaks to shift to higher energies.

In Chapt. III it will be shown that the temperature dependence of the Λ doublet peak and the major Σ peak can be calculated accurately from a knowledge of the lattice expansion coefficient and the Debye-Waller factors. Since both ZnTe and ZnSe are in many respects similar to GaAs, the temperature dependence observed in the present measurements should be accurately explained by similar calculations.

Finally, slightly better resolution is possible at low temperatures because of decreased phonon emission and absorption. The lifetime broadenin is reduced from about 0.15 eV at room temperature to about 0.05 eV at

low temperatures.[37,29] Consequently, in the low temperature data for ZnTe a new shoulder appears at 5.23 eV, which corresponds to the shoulder at 5.25 eV in the theoretical calculation. For ZnSe, the only significant change in structure is the splitting of the major Σ peak, causing it to agree closely with the shape of the theoretical peak.

4. Discussion of Results

We have obtained good agreement between measured and calculated reflectivity and between $R'(\omega)/R(\omega)$ and thermo-reflectance. The agreement appears good enough to indicate that our identifications of the important optical structures are substantially correct and that our band structure is accurate in the region near the fundamental gap.

Significant disparity between experimental and theoretical reflectivity occurs for higher energy transitions, typically for transitions with energy greater than 2.5 to 3 times the fundamental gap. As pointed out in Chapt. I this disparity results essentially because of the rapidly decreasing $\varepsilon_2(\omega)$ at these energies. In addition, a comparison of the experimental and calculated values of the static dielectric constant reveals that the calculated value is usually 10% to 20% lower than the experimental value, indicating that the $\varepsilon_2(\omega)$ contributions are again too low. However, the inclusion of many-body effects has been shown to increase $\varepsilon_2(\omega)$ at higher energies.[38] Bardasis and Hone suggest that the dominant scattering process for a high-energy conduction electron is an Auger-type effect, i.e., a two-electron process that need not conserve momentum. The threshold for this type of scattering is approximately twice the fundamental gap.

We attempt to account for these many-body effects with a simple model for adding contributions from indirect transitions at energies greater than twice the fundamental gap. We define a function

$$I(\omega) = \frac{A}{\omega^2} \int_0^{\omega} D(\omega') D(\omega'-\omega)d\omega', \qquad (2.6)$$

where $D(\omega)$ is the electronic density of states with the top of the valence band defined as $\omega = 0$. A is a normalization factor, defined such that the Kramers-Kronig transformation of $I(\omega)$ yields the experimental value of the static dielectric constant. $I(\omega)$ can be interpreted to be the imaginary part of the dielectric function for indirect transitions. For the case of ZnSe, we take the static dielectric constant to be 5.9 and define a new $\varepsilon_2(\omega)$:

$$\varepsilon_2(\omega) = \begin{cases} \varepsilon_2(\omega) & \omega \leq 6.4 \text{ eV} \\ [(12.0\omega)\varepsilon_2(\omega) + (\omega-6.4)I(\omega)]/5.6 & 6.4 \text{ eV} \leq \omega \leq 12.0\text{eV} \\ I(\omega) & 12 \text{ eV} < \omega < 14.\text{ev} \\ \beta\omega/(\omega^2+\gamma^2)^2 & \omega \geq 14.\text{eV} \end{cases} \qquad (2.7)$$

In other words, we let $\varepsilon_2(\omega)$ change linearly from entirely direct transitions at 6.4 eV (about twice the fundamental gap) to entirely indirect transitions at 12.0 eV. A tail function is added at 14 eV.

The resulting $\varepsilon_2(\omega)$ and $R(\omega)$ are shown in Figs. 23 and 24. This new $\varepsilon_2(\omega)$ is larger at high energies, and this has two desirable effects. First, the calculated static dielectric constant is raised from 4.7 to its experimental value of 5.9. The second consequence is that the agreement between experimental and calculated reflectivity is much better at higher energies, although some agreement is sacrificed at lower energies.

C. Comparison of the Optical Properties of GaAs and Si

Among the many different schemes for differential spectroscopy,[39] the wavelength modulation technique is the most attractive. In this technique the crystal is not perturbed by external fields, as it is in the electro-reflectance and thermoreflectance techniques. The fact that the wavelength modulation spectrum is simply the derivative of the normal reflectivity spectrum leaves no ambiguity in its interpretation. Also, the method magnifies the contribution of each peak and shoulder in the reflectivity spectrum. For these reasons the wavelength modulation spectrum ($R'(\omega)/R(\omega)$) is particularly desirable for comparison purposes. In this section the theoretical calculations of $R'(\omega)/R(\omega)$ for GaAs and Si are compared to experimental measurements obtained using the wavelength modulation technique.[29]

The pseudopotential form factors for GaAs and Si are listed in Table I. Because the agreement between theory and experiment for Si is found to be good with the initial form factors, further adjustment of the Si form factors is not necessary. Furthermore, since the spin-orbit splitting at $\Gamma_{25'}$ for Si is only 0.04 eV, the spin-orbit parameter is assigned the value zero. For GaAs, the spin-orbit parameter is adjusted so that the spin-orbit splitting at Γ_{15} is 0.35 eV.

1. GaAs

The calculated band structure of GaAs appears in Fig. 13, and identifications of the important reflectivity structure are tabulated in Table VIII. A comparison of the theoretical and experimental derivative spectra appears in Fig. 25. The positions of the important reflectivity peaks are given by those zeroes of $R'(\omega)/R(\omega)$ at which the slope is

negative. The other structure appearing in the derivative spectrum is much finer; some of these details are practically imperceptible when seen in the reflectivity spectrum.

The fundamental gap occurs at Γ at 1.52 eV in both theory and experiment.[40] The major structure in the 2.8 to 3.3 eV region is a double reflectivity peak caused by the spin-orbit split Λ transitions. The first peak at 3.02 eV is caused by $\Lambda(4\text{-}5)$ transitions and the second peak at 3.24 eV is caused by $\Lambda(3\text{-}5)$ transitions. The theoretical peaks occur at 3.05 and 3.25 eV, giving excellent agreement with the experiment. Although no such structure is apparent in the experimental spectrum,[41] a fine structure caused by $L(4\text{-}5)$ transitions does appear in the theoretical spectrum at 2.90 eV. The next major reflectivity structure occurs at 5.11 eV in the experimental measurements and at 4.94 eV in the theoretical calculations. It is caused by a combination of $\Sigma(4\text{-}5)$, $\Delta(3\text{-}5)$, and $\Delta(4\text{-}5)$ transitions, all with large matrix elements. The fine structure in this region (4.2 to 5.1 eV) consists of three peaks in the experimental derivative spectrum. The structure in the 4.2 to 4.7 eV region appears in the reflectivity spectrum only as two small bulges on the low-energy side of a much larger peak. These are located at 4.44 and 4.60 eV and are caused by $\Delta(4\text{-}5)$ and $\Delta(3\text{-}5)$ transitions. The major peak at 5.11 eV in the experimental spectrum is caused by $\Sigma(4\text{-}5)$ transitions but does not show the fine structure present in the theoretical spectrum. Both experiment and theory show a broad ($\sim$1/2 eV) structure immediately above the $\Sigma(4\text{-}5)$ peak. This is caused by $\Delta(4\text{-}6)$ and $\Delta(3\text{-}6)$ transitions.

2. Si

The band structure for Si is identical to the one appearing in Ref. 5. A comparison of the theoretical and experimental derivative spectra appears in Fig. 26. Identifications of the important reflectivity structures are tabulated in Table IX.

No structure corresponding to the fundamental gap of 3.13 eV at L appears either in the theoretical or the experimental spectrum, however, the agreement between experiment and theory in this region is good enough to suggest that the first direct gap is at L. The first major peak in the reflectivity appears at 3.45 eV in the experimental spectrum and at 3.46 eV in the theoretical spectrum and is caused mainly by Λ(4-5) transitions and by Δ(4-5) transitions. A small dip occurs in the spectra at 3.40 eV for the experiment and at 3.35 eV for the theory. This structure is attributed to (4-5) transitions in a volume centered at (0.3, 0.3, 0.2) (units of $2\pi/a$) and to Δ(4-5) transitions close to Γ. A small peak caused by Λ(3-5) transitions appears in the theoretical reflectivity at 3.68 eV, but it does not appear in the experimental spectrum. The major reflectivity peak occurs at 4.57 eV in the experimental measurements and at 4.51 eV in the theoretical calculations. It is caused almost entirely by Σ(4-5) transitions near (0.4, 0.4, 0.). The small experimental structure at 4.32 eV is attributed to (3-5) transitions near (0.3, 0.2, 0.1) and to (4-5) transitions in the vicinity of X. The next reflectivity peak occurs at 5.48 eV for the experiment and at 5.38 eV for the theory and is caused by (4-6) transitions in a volume centered at (0.6,0.4, 0.3) (near Λ).

The location in the zone of transitions responsible for a particular reflectivity structure is somewhat speculative for Si. The reason for this is that there are many critical points in the joint density of states and it is difficult to distinguish which of these are the more important for a particular structure. Other authors[42] have made similar comments as to the great density of critical points in the Si band structure.

For both GaAs and Si, the $\Lambda(4-5)$ peaks are much sharper in the experimental spectra than in the theoretical spectra. The theoretical structure in this region more closely resembles the room temperature spectrum than the low temperature spectrum. This ame low-temperature sharpening of the Λ peaks consistently occurs in other III-V cubic semiconductors,[29] and it is thought to be cause by exciton effects. Furthermore, electroreflectance line shapes also indicate exciton effects are present.[24] Thus, the sharpening of the Λ peaks can be explained in terms of the reduction of lifetime broadening of the hyperbolic excitons associated with Λ.

The low-temperature derivative spectra for GaAs and Si by Zucca and Shen[29] show clear improvement in spectral resolution over other techniques. Consequently, it is heartening to observe that the spectra computed from the pseudopotential band structures are in excellent agreement with the experimental measurements. The extent of this agreement gives one confidence that the above identifications of the important optical transitions are substantially correct.

CHAPTER III: TEMPERATURE EFFECTS ON THE ELECTRONIC BAND STRUCTURE

A. Theory

The principal factors governing the temperature dependence of the energy bands are the thermal expansion of the lattice and the thermal vibrations of the nuclei (the Debye-Waller effect). The first effect accounts for 10-20% of the temperature shifts of energy levels and the Debye-Waller effect accounts for the remainder.[43]

An increase in temperature generally causes an expansion of the lattice, which, in turn, reduces the kinetic energy of an electron, as well as the average potential seen by an electron. The kinetic energy varies as $(h^2/2m)(a)^{-2}$ and consequently it decreases as the lattice constant a increases. The pseudopotential may be written in the form

$$V(q) = 1/\Omega \int V_a(r) \exp(-iq\cdot r)\, d^3r \qquad (3.1)$$

where Ω is the volum of the primitive cell and $V_a(r)$ is the atomic pseudopotential, i.e., the effective potential of an isolated atom. Obviously, $V_a(r)$ is not altered by a change in the lattice constant, but $V(q)$ is altered. The new pseudopotential $V_n(q)$ must be evaluated at new reciprocal lattice vectors G'. This may be written

$$V_n(G') = 1/\Omega' \int V_a(r) \exp(-iG'\cdot r)\, d^3r = \Omega/\Omega'\, V(G') \qquad (3.2)$$

where Ω' is the new volume of the primitive cell. To evaluate $V_n(G')$ when $V(q)$ is known only for a discrete number of values, it is necessary to interpolate between known values, but this can be done with negligible error. Since (Ω/Ω') is usually the dominant factor in (3.2), $V_n(G')$ is

smaller than V(G), and therefore the potential for an expanded lattice is weaker. And since the energy differences between bands are a measure of the strength of the potential, the energy splittings for an expanded lattice at higher temperatures are less, except in special cases, such as the lead salts.[44]

The thermal vibrations of the nuclei act to reduce the effective potentials by the Debye-Waller factor e^{-W}. This may be seen by using the formalism of Glauber[45] for time-dependent displacement correlations in crystals. The idea is that the vibrating atoms may be viewed as a displacement field of collective excitations (phonons), and the thermal averaging can be performed over this field. The α- component of the displacement field may be written

$$u_\alpha(\underset{\sim}{r},t) = \sum_{\underset{\sim}{k},p} e_\alpha^{(p)} \left(\frac{\hbar}{2NM\omega}\right)^{1/2} (a_{\underset{\sim}{k},p} \exp(i\underset{\sim}{k}\cdot\underset{\sim}{r}-i\omega t) + a_{\underset{\sim}{k},p}^{+} \exp(-i\,\underset{\sim}{k}\cdot\underset{\sim}{r} + i\omega t)) \tag{3.3}$$

$\underset{\sim}{e}^{(p)}$ (p=1,2,3) are the three unit polarization vectors for waves of propagation vector $\underset{\sim}{k}$ and angular frequency $\omega=\omega^{(p)}(\underset{\sim}{k})$. The amplitudes $a_{k,p}$ and $a_{k,p}^{+}$ are destruction and creation operators for phonons. In this formulation, two bilinear combinations of $a_{k,p}$ and $a_{k,p}^{+}$ have non-vanishing expectation values,

$$\langle a_{k,p}^{+} a_{k,p}\rangle = n_{k,p}, \quad \langle a_{k,p}\, a_{k,p}^{+}\rangle = n_{k,p} + 1, \tag{3.4}$$

where $n_{k,p}$ is the average number of quanta in the mode specified by $\underset{\sim}{k}$ and $\underset{\sim}{p}$. The average quantum populations are given by

$$n_{k,p} = [\exp(\hbar\omega^{(p)}(\underset{\sim}{k})/KT) - 1]^{-1}, \tag{3.5}$$

in which K is the Boltzmann constant and T the temperature.

The crystal potential may be written

$$V(\underset{\sim}{r},t) = N^{-1} \sum_{m=1}^{N} V_a(\underset{\sim}{r} - \underset{\sim}{R}_m - \underset{\sim}{u}(\underset{\sim}{R}_m,t)), \tag{3.6}$$

which is based on the assumption that the individual potentials are shifted rigidly along with their lattice points $\underset{\sim}{R}_m$. This potential may be Fourier analyzed to give

$$V(q,t) = N^{-1} \sum_{m} V(q) \exp(i\underset{\sim}{q}\cdot\underset{\sim}{R}_m + i\underset{\sim}{q}\cdot\underset{\sim}{u}(R_m,t)) \tag{3.7}$$

This expression must now be averaged over an ensemble of states at temperature T. The only term which must be considered is $\exp(i\underset{\sim}{q}\cdot\underset{\sim}{u})$. It is shown by Glauber[45] that the ensemble average for a zero-quantum process (essentially a thermal averaging) is

$$\langle \exp(i\underset{\sim}{q}\cdot\underset{\sim}{u})\rangle_T = \exp(-1/2\langle(\underset{\sim}{q}\cdot\underset{\sim}{u})^2\rangle_T) \tag{3.8}$$

Therefore, the thermally averaged potential is

$$V_T(q) = N^{-1} \sum_{m} V(q) \exp(i\underset{\sim}{q}\cdot\underset{\sim}{R}_m) \exp(-1/2\langle(\underset{\sim}{q}\cdot\underset{\sim}{u})^2\rangle_T \tag{3.9}$$

$$V_T(q) = \begin{cases} V(q)\exp(-1/2\langle(\underset{\sim}{G}\cdot\underset{\sim}{u})^2\rangle_T), \\ 0, \text{ otherwise} \end{cases} \tag{3.10}$$

for $\underset{\sim}{q}=\underset{\sim}{G}$, a reciprocal lattice vector,

Thus, the net effect of the Debye-Waller factor is to reduce the values of the pseudopotential V(G). The thermal vibrations do not smear the potentials, that is, they do not mix in other nearby Fourier components. This effect is what is observed in X-ray scattering.[46]

These two effects, the thermal expansion of the lattice and the thermal vibrations of the nuclei, are applied to the calculation of the energy band of GaAs in the next section.

B. Application to GaAs

The theory of the preceding section is used to calculate the temperature dependence of the energy bands for GaAs. GaAs is chosen because of the availability of excellent wavelength-modulation spectra[47] at 5, 80, 150, 225, and 300°K. In this section, attention is focused on the temperature dependence of the Λ_3-Λ_1 and Σ_2-Σ_1 transitions, which are responsible for the E_1 doublet peak and E_2 peak in the reflectivity.

The wavelength modulation spectra for the five temperatures in the regions of the E_1 doublet peak and the E_2 major peak are shown in Fig. 27. The positions of the peaks and valleys of the reflectivity are given by the zeroes of the modulated spectra. The temperature shifts of the E_1 and E_2 peaks are plotted in Fig. 28.

To calculate the theoretical temperature dependence of the GaAs spectrum it is necessary to know the electronic band structure, the transitions which cause the reflectivity peaks, the thermal expansion function, and the phonon spectrum of the crystals. The band structure of GaAs is the one obtained in Chapt. II.

The temperature dependence of the lattice constant is obtained from the thermal-expansion function[48] for GaAs. The lattice constants used at 5, 80, 150, 225, and 300°K are 5.640, 5.640, 5.641, 5.643 and 5.645A, respectively. As described in the preceding section, changes in the lattice constants necessitate scaling the pseudopotential form factors.

The Debye-Waller factor can be calculated from the experimental phonon spectrum, and since this calculation is greatly simplified for a monatomic crystal, the phonon spectrum of germanium is used instead of GaAs. This is a reasonable approximation because the GaAs phonon spectrum is nearly identical to that of germanium,[49] and the average density of GaAs is within 0.5% that of germanium. Immediate simplification of (3.10) can be made for a monatomic cubic crystal, since for this case the phonon polarization vectors are mutually perpendicular. From this fact and from (3.3) and (3.4), one obtains

$$\langle (G\cdot u)^2 \rangle = 3\langle G_\alpha^2 \rangle \langle u_\alpha^2 \rangle = G^2 \langle u_\alpha^2 \rangle, \qquad (3.11)$$

where

$$\langle u_\alpha^2 \rangle = \sum_{k,p} \left(\frac{\hbar}{2NM\omega}\right)(2n_{k,p} + 1) \qquad (3.12)$$

Using (3.12) and (3.5), (3.11) may be written in a more convenient form:

$$W \equiv 1/2 \langle (\underset{\sim}{G}\cdot\underset{\sim}{u})^2 \rangle = \frac{hG^2}{8\pi^2 M} \frac{\int \rho(\nu)\nu^{-1} \left[1/2 + \frac{1}{e^x - 1}\right] d\nu}{\int \rho(\nu) d\nu} \qquad (3.13)$$

where $x = h\nu/kT$, $\rho(\nu)$ is the density of phonon modes for Ge,[49] G is a reciprocal lattice vector, and M is the mass of the nucleus. The values of (W/G^2) we obtain by using (3.13) at 5, 80, 150, 225, and 300°K are 0.0010, 0.0015, 0.0024, 0.0034, and 0.0044, respectively.[50] Using X-ray measurements on germanium, Batterman and Chipman[51] obtain a value of $(W/G^2) = 0.0043$ at 300°K.

The Debye-Waller and lattice expansion effects are incorporated in a pseudopotential calculation of the band structure to give the temperature shifts of selected transitions in the Brillouin zone. In Table X,

the resulting theoretical temperature dependence at Γ (the fundamental gap) is compared to the experimental temperature dependence obtained by Oswald[52] and by Sturge.[53] The calculated result at Γ agrees closely with that of Oswald. The Debye-Waller and lattice expansion effects can be calculated separately to show that the major part of the energy shift is caused by Debye-Waller effect, with only a small fraction caused by lattice expansion. At Γ the total calculated energy change between 5° and 300°K is -0.158 eV of which -0.020 eV is caused by lattice expansion, or about 13% of the total.

An additional check on the accuracy of the theoretical calculations using this pseudopotential band structure is provided by a calculation of the variation of the fundamental gap with respect to a slight change in the lattice constant. This calculation gives a value of $V(\partial E/\partial V) = -7$ eV, a result which agrees exactly with the experimentally measured value.[54]

The theoretical temperature dependence of the $\Lambda(4-5)$, $\Lambda(3-5)$, and $\Sigma(4-5)$ transitions is shown in Fig. 28. The comparison between theory and experiment for the E_2 peak is good, and for the E_1 doublet the comparison is excellent.

The temperature shifts of the reflectivity peaks in GaSb, InAs, and InSb are found to be approximately of the same magnitude as in GaAs.[29] Similar theoretical calculations of the temperature dependence in these crystals should also yield good results.

CHAPTER IV: WAVE-VECTOR-DEPENDENT DIELECTRIC FUNCTION

In this chapter a calculation is presented of the longitudinal wave-vector-dependent dielectric function $\varepsilon(\underset{\sim}{q})$ for the semiconductors, Si, Ge, GaAs, and ZnSe. Explicit results are given in the (1,0,0), (1,1,0) and (1,1,1) directions in the range $0 \leq q \leq (4\pi/a)$. A comparison is made between the present results and the results of other calculations. Some comparisons with experiment are also made.

$\varepsilon(\underset{\sim}{q})$ describes the response of a crystal to an electric field parallel to $\underset{\sim}{q}$:

$$\underset{\sim}{D}\ e^{i\underset{\sim}{q}\cdot\underset{\sim}{r}} = \varepsilon(\underset{\sim}{q})\ \underset{\sim}{E}\ e^{i\underset{\sim}{q}\cdot\underset{\sim}{r}}. \tag{4.1}$$

For most applications one is interested in either static fields or fields varying with phonon frequencies; in this frequency region the frequency-dependent dielectric function may be replaced with the static dielectric function $\varepsilon(\underset{\sim}{q})$, an approximation which is accurate to within 0.1%.

Using the expression for $\varepsilon(\underset{\sim}{q})$ given by Ehrenreich and Cohen,[54a] one obtains

$$\varepsilon(\underset{\sim}{q}) = 1 + \frac{8\pi e^2}{q^2} \sum_{k,c,v} \frac{|(\underset{\sim}{k}+\underset{\sim}{q},v|\underset{\sim}{k},c)|^2}{E_c(\underset{\sim}{k})-E_v(\underset{\sim}{k}+\underset{\sim}{q})}, \tag{4.2}$$

where $\underset{\sim}{k}$ is summed over the first Brillouin zone, v over the valence bands and c over the conduction bands. In these calculations the electronic wave functions and energy eigenvalues have been calculated using the empirical pseudopotential method. Spin-orbit effects have not been included.

Calculations of $\varepsilon(\underset{\sim}{q})$ for semiconductors were first performed by Penn,[55] using a 2-band model isotropic semiconductor. These calculations

have recently been redone by Srinivasan.[56] The present calculations agree farily well with Srinivasan's calculations except that our results exhibit a slight anisotropy. Calculations based on more realistic band models for Si and Ge have been performed by Nara.[57] Despite the fact that his model is almost identical to ours, his results disagree to some extent with our results. In particular, he finds a strong anisotropy in $\varepsilon(\underset{\sim}{q})$ at small q which is missing from our results. In addition, our calculations show $\varepsilon(\underset{\sim}{q})$ to be a monotonically decreasing function of $|q|$, a feature which is not present in the results of Srinivasan or of Nara. (See Fig. 29).

$\varepsilon(\underset{\sim}{q})$ has had many applications; it has been used to calculate the lattice vibration spectrum of silicon,[58] screened pseudopotential form factors,[59] and screened impurity potentials.[60]

A. Method of Calculation

For the purposes of calculation Eq. (1.1) is written as follows:

$$\varepsilon(\underset{\sim}{q}) = 1 + \frac{8\pi e^2}{q^2} \frac{2}{(2\pi)^3} \sum_{\Delta k,c,v} \frac{|\langle \underset{\sim}{k}+\underset{\sim}{q},v|\underset{\sim}{k},c\rangle|^2 (\Delta k)^3}{E_c(\underset{\sim}{k}) - E_v(\underset{\sim}{k}+\underset{\sim}{q})} \qquad (4.3)$$

where the summation is over cubes of volume $(\Delta k)^3$ in the first Brillouin zone, with suitable truncations at the zone boundaries. The summation index v spans the top four valence bands and the index c spans the bottom eleven conduction bands. For the semiconductors we consider, $E_c(\underset{\sim}{k})$ is always greater than $E_v(\underset{\sim}{k}+\underset{\sim}{q})$, and thus each contribution to $\varepsilon(\underset{\sim}{q})$ is positive. Energy eigenvalues and eigenvectors are computed for each of 3360 points in the first Brillouin zone. The coordinates of the grid of calculated points are given by $(1/16)(2s+1, 2m+1, 2n+1)$ in units of $(2\pi/a)$, where s, m, and n are integers.

For an arbitrary direction of $\underset{\sim}{q}$ the summation in Eq. (4.3) must be performed over the entire Brillouin zone. Fortunately, symmetry properties can be exploited to reduce the computation time by a factor of eight in the (1,0,0) direction, by six in the (1,1,1) direction, and by four in the (1,1,0) direction. The computation time for a particular value of $\underset{\sim}{q}$ can be reduced by an additional factor of fifteen is $\underset{\sim}{q}$ is chosen such that $(\underset{\sim}{k}+\underset{\sim}{q})$ also lies on the grid of calculated points.

The 3360 points in the summation over the Brillouin zone provide sufficiently accurate convergence. Other calculations[61] of $\varepsilon(0)$ using over three million points in the Brillouin zone differ from our values of $\varepsilon(0)$ by less than 3%.

B. Results of Calculations

The calculated dielectric functions of Si, Ge, GaAs, and ZnSe appear in Figs. 30-33. For all four crystals $\varepsilon(\underset{\sim}{q})$ is a smooth monotonically decreasing function of $|\underset{\sim}{q}|$, with zero gradient at $\underset{\sim}{q} = 0$. $\varepsilon(\underset{\sim}{q})$ was calculated at several points for small $\underset{\sim}{q}$ to make certain it exhibited no maximum (for $\underset{\sim}{q} \neq 0$). Such maxima do occur in the results of Srinivasan[56] and of Nara.[57]

$\varepsilon(\underset{\sim}{q})$ in the (1,1,0) direction is practically indistinguishable from $\varepsilon(\underset{\sim}{q})$ in the (1,0,0) direction. The values of $\varepsilon(\underset{\sim}{q})$ in the (1,1,1) direction are slightly less than in the other directions. A possible reason for this slight anisotropy is that the (1,1,1) direction is the direction to the nearest neighboring atoms in the crystal. Between nearest neighbors there is good evidence for localized bonding charges. This has been confirmed by X-ray diffraction experiments for diamond.[62] This localized electronic charge constrains the electronic charge dis-

tribution and seems to prevent the screening from being as effective. Consequently, $\varepsilon(\underset{\sim}{q})$ is lower in magnitude in the (1,1,1) direction than in the other directions.

C. Comparison of Results

As stated above, our calculations show that $\varepsilon(\underset{\sim}{q})$ decreases as $|q|$ increases, and there exists little anisotropy for small q. This decrease in $\varepsilon(\underset{\sim}{q})$ is in contrast to the results of Srinivasan,[56] who finds that $\varepsilon(\underset{\sim}{q})$ increases in this region. However, he does not that this increase is sensitive to his choice of matrix elements.

Our results for small q also contrast with the results of Nara.[57] Nara finds that $\varepsilon(\underset{\sim}{q})$ increases rapidly and is remarkably anisotropic for small q. From our experience with these calculations, we find that great care must be taken when we calculate the inner products for small q. The inner product of two Bloch wave functions $u_n(\underset{\sim}{k})$ and $u_m(\underset{\sim}{k}+\underset{\sim}{q})$ should go smoothly to zero as $\underset{\sim}{q} \to 0$, but for certain points $\underset{\sim}{k}$ in the zone there occur discontinuities in the inner products as $\underset{\sim}{q} \to 0$. The reason for such a discontinuity is that in the pseudopotential method the wave functions $u_n(\underset{\sim}{k})$ and $u_m(\underset{\sim}{k}+\underset{\sim}{q})$ are expanded in two different sets of planes waves, the first set satisfying the criterion $|\underset{\sim}{k}+\underset{\sim}{G}|^2 < 7$ and the second set satisfying $|\underset{\sim}{k}+\underset{\sim}{q}+\underset{\sim}{G}|^2 < 7$. The immediate effect is to cause the absolute values of these inner products to increase much too rapidly. The overall effect does produce sizeable errors in $\varepsilon(\underset{\sim}{q})$, especially for small q, and in particular, it produces a hump-like effect similar to the results of Nara at small q. When we use the proper approach of expanding the wave function $u_m(\underset{\sim}{k}+\underset{\sim}{q})$ in the same set of plane waves as

for $u_n(\underset{\sim}{k})$, we obtain no maxima for non-zero q and little anisotropy for small q. It should be noted that for larger q, good agreement exists between our results and the results of Nara.

In Fig. 29 we compare our calculation of the dielectric function of silicon with the calculations by Srinivasan and by Nara. We obtain a value for $\varepsilon(0)$ of 11.3 for Si, while Nara obtains a value of 10.8. The measured value is 11.7±0.2,[63] a value which Srinivasan uses as a parameter in his model. For Ge, GaAs, and ZnSe we obtain values for $\varepsilon(0)$ of 14.0, 8.9, and 4.8, respectively, while the measured values are Ge 15.8,[63] GaAs 10.9[64] and ZnSe 5.9.[65]

D. Applications

An immediate application of our results is a more precise calculation of screened pseudopotential form factors, as suggested by Phillips[59] and by Srinivasan.[56] In particular, our calculations allow us to evaluate the pseudopotential form factor $V_p(G_1)$ for Si. (G_1 is the magnitude of the first reciprocal lattice vector $(2\pi/a)(1,1,1)$). Now the screened pseudopotential form factors for Si have already been calculated by Animalu and Heine,[66] but they used the Hartree free-electron dielectric function $\varepsilon_f(\underset{\sim}{q})$[67] to screen the ion-core instead of the correct dielectric function $\varepsilon(\underset{\sim}{q})$. We propose to demonstrate that by using our $\varepsilon(\underset{\sim}{q})$ as the screening function, we obtain a value of $V_p(G_1)$ for Si remarkably close to the empirically determined value (Table I), provided we include an exchange correction term of the form suggested by Hubbard.

Animalu and Heine screened the atomic form factor $V_a(q)$ for Si with the function $X_f(q)$:

$$V_p(\underset{\sim}{q}) = V_a(\underset{\sim}{q})/X_f(\underset{\sim}{q}), \tag{4.4}$$

where

$$X_f(\underset{\sim}{q}) = 1 + [\varepsilon_f(\underset{\sim}{q}) - 1]\,[1 - 1/2\; q^2(q^2+k_s^2+k_F^2)^{-1}]. \tag{4.5}$$

The quantity in the second bracket is an approximation suggested by Hubbard[68] to accout for the exchange correction on a free-electron gas. (Animalu and Heine chose $k_s = 2k_F/\pi$). For $\underset{\sim}{q} = \underset{\sim}{G}_1$ the value of this exchange term is (0.77). For a free-electron gas with the density of the valence electrons of Si, $\varepsilon_f(G_1) = 1.98$, so that $X_f(G_1) = 1.76$. If the correct $X(q)$ is defined in an analogous manner to $X_f(q)$, with $\varepsilon(q)$ replacing $\varepsilon_f(q)$, our value of $\varepsilon(G_1) = 1.43$ gives $X(G_1) = 1.33$.

The complete pseudopotential $V_p(G_1)$ must also account for the bonding charges. Since $\varepsilon(0) = 11.7$ for Si, there is a charge of $(2e/\varepsilon(0))$ in each of the bonding charges located midway between nearest Si atoms. The total expression is

$$V_p(q) = V_a(q) + (S_b(q)/S_a(q))\; V_b(q), \tag{4.6}$$

where V_a and V_b are the properly screened pseudopotentials for the Si atoms and the bonding charges, respectively, and (S_b/S_a) is the ratio of the structure factors of the bonding charges to the Si atoms.

$V_a(G_1)$ is just equal to Animalu and Heine's value of (-0.18ry), corrected by a factor $X_f(G_1)/X(G_1)$. Therefore, $V_a(G_1) = (-0.18)(1.76/1.33) = -0.238$ry. $V_b(q)$ may be calculated from Poisson's equation:

$$V_b(q) = \left(\frac{4\pi e}{\Omega q^2}\right)\left(\frac{8e}{\varepsilon(0)}\right) \tag{4.7}$$

The exchange correction reduces $V_b(G_1)$ by a factor (0.77). Thus we have $(S_b/S_a)\; V_b(G_1) = 0.031$ry. Consequently,

$$V_p(G_1) = -0.238 + 0.031 = -0.207\text{ry}. \qquad (4.8)$$

This value is in excellent agreement with the value of $V_p(G_1) = -0.21$ry obtained by Brust, Cohen, and Phillips.[69]

We can make similar arguments for germanium. $V_a(G_1)$ is equal to Animalu and Heine's value of (-0.19ry), corrected by a factor $X_f(G_1)/X(G_1)$, which gives $V_a(G_1) = -0.251$ry. V_b is reduced because $\varepsilon(0) = 15.8$ for Ge, and thus $(S_b/S_a)\, V_b(G_1) = 0.022$ry. Consequently,

$$V_p(G_1) = -0.251 + 0.022 = -0.229\text{ry}. \qquad (4.9)$$

This value is in excellent agreement with the value of $V_p(G_1) = -0.23$ry obtained by Cohen and Bergstresser.[5]

It should be noted that the comments by Srinivasan on Nara's results do not hold for our results. We have used a large number of interband transitions (1-4) → (5-15) in our calculations. The convergence at large q is satisfactory in view of the very small contribution to $\varepsilon(q)$ from the transitions (4→14), (4→15),etc. Furthermore, our value of $\varepsilon(0) = 11.3$ is obtained without the necessity of adding more sampling points for the case q = 0.

CHAPTER V: CHARGE DISTRIBUTION IN SEMICONDUCTORS

The wavefunctions given by the pseudopotential method may be used to calculate the distribution of valence charge within semiconductors. One may investigate how the charge distribution varies in the different energy bands and whether different crystals show trends with respect to bonding of the atoms. The variation of the charge distribution with band index or with changes in elements may not yield accurate quantitative results, but observation of trends occuring in a series of crystals can yield some physical reason for why crystals behave as they do. One can envision many "gedanken" experiments that might help to answer such questions as why substances crystallize in certain structures or why certain energy levels are more sensitive to pressure than others. Questions of this type are explored in this chapter.

A. Method of Calculation

The probability of finding an electron in a certain spatial region of volume $d\Omega$ is given by $|\Psi_{n,\underset{\sim}{k}}(\underset{\sim}{r})|^2 d\Omega$, where n is the index of the energy eigenvalue associated with the state $\underset{\sim}{k}$. When many different electronic states k are considered, it becomes meaningful to speak of a charge distribution for the electrons. In particular, the charge density for each valence band may be written

$$\rho(\underset{\sim}{r}) = \sum_{\underset{\sim}{k}} e\, |\Psi_{n,\underset{\sim}{k}}(\underset{\sim}{r})|^2, \qquad (5.1)$$

where the summation is over all states in the Brillouin zone.

To obtain adequate convergence in calculating $|\Psi_{n,k}|^2$, it is necessary to represent each $\Psi_{n,k}$ in an expansion of at least 85 plane waves. The wavefunctions are evaluated on a grid of 3360 points in the Brillouin

zone. The coordinates of the grid points are given by (1/16)(2s+1, 2m+1, 2n+1) in units of ($2\pi/a$), where s, m, and n are integers.

By using (5.1) the charge density $\rho(\underset{\sim}{r})$ is evaluated at over 1500 points in a plane which intersects both atoms in the primitive cell (a(1,-1,0) plane). A diagram of this plane and its orientation with respect to the surrounding atoms is shown in Fig. 34. The values of $\rho(\underset{\sim}{r})$ are shown in contour plots. The density is plotted in units of (e/Ω) where Ω is the volume of the primitve cell ($\Omega=1/4a^3$).

B. Results of Calculations for Ge, GaAs and ZnSe

The charge density distribution is calculated for Ge, GaAs, and ZnSe; the elements in these semiconductors are all in the fourth row of the Periodic Table. This choice allows us to look at the ionic trends for crystals that are otherwise expected to have nearly the same properties. The results of the calculations are shown in detailed contour maps of the valence charge density (Figs. 35-43). The contours are striking and can be used to describe selected physical properties of crystals to a more general audience. One can definitely see tetrahedral covalent bonding in germanium, where the charge density piles up halfway between the two atoms (Figs. 35, 38, 39). The tetrahedral structure comes from the structure factors originally put into the Hamiltoniam from (1.3). The large charge density peaks (the covalent bonds) are caused by the quantum mechanical effects of sharing electrons.

Ionic trends in the bonding may be seen by looking at the total valence change density for GaAs and ZnSe (Figs. 36-37). For GaAs the center of the bonding charge moves toward the anion (the As atom), and

for ZnSe the bonding charge moves even closer to the anion (the Se atom). Another trend that is noticeable is that the amount of bonding charge decreases in the sequence Ge to GaAs to ZnSe. Thus the covalent bonding becomes less noticeable as the crystals become more ionic.

The trend in the charge distribution in going from band 1 to band 4 is to pile up charge in the bonds. In band 1 the charge accumulates around the atoms and in band 4 there is much more charge in the bonds. In band 1 of Ge most of the charge is distributed around the atoms with a very slight build-up between the atoms (Fig. 38). In band 4 there is negligible charge at the Ge atoms and there is a substantial build-up between the atoms (Fig. 39). This says that those electrons less tightly bound to the Ge atoms are more likely to be engaged in covalent bonding.

In band 1 of GaAs almost all the charge density is centered about the As ion (Fig. 40). The reason for this becomes clear if one considers a hypothetical crystal of GaAs which lacks electrons. If enough electrons are put into the crystal to fill the first band, the electrons will be more attracted to the As^{+5} ion than to the Ga^{+3} ion, causing the As ion now to appear as As^{+3}. This distribution clearly has s-like character. In band 2 the charge distribution shows much more covalent character and is now displaced toward the Ga ion slightly (Fig. 41). This distribution appears to be a mixture of s and p character, i.e., there is charge at both the ion sites and the bonding sites. In bands 3 and 4 the covalent charge build-up is even greater and the charge distribution clearly favors the As ion (Fig. 42). This is clearly p-like bonding, since there is negligible charge density at the ion sites and a high

charge density at the bonding sites.

It is also interesting to consider what the charge distribution would be if there were enough electrons to fill band 5, the first conduction band. Molecular orbital theory[70] predicts that the excited states will be anti-bonding, i.e., a charge build-up will occur in an opposite direction from the bonding charge. This is precisely what is seen in the charge distribution for band 5 in the three crystals; such a distribution is particularly striking for ZnSe (Fig. 43). There is a pronounced build-up in the lower left portion of the figure, and this anti-bonding site is exactly opposite in direction to the normal bonding site. There is also a peak in the charge density at the site of the Se ion, but there is no appreciable build-up at the site of the normal bonding charge.

C. Application to Crystal Structure

Recently Phillips[71] has proposed a simple method of classifying the ionicity of binary crystals of the formula $A^N B^{8-N}$. His ionicity factor f_i varies between zero and one: $f_i=0$ designates a completely covalent-bonded crystal and $f_i=1$ designates a completely ionic crystal. The interesting aspect of Phillips' scale is that a value of $f_i=0.785$ neatly separates the more covalent crystals with 4-fold coordination (zincblende and wurtzite structures) from the more ionic crystals with 6-fold coordination (rocksalt structure). This value of f_i is completely empirical. However, the results presented below suggest that this critical value of f_i can be calculated using the band structures from known crystals.

The idea is that the atoms in crystals of 4-fold coordination form directed covalent bonds through hybridization of (sp^3) orbitals, and that crystals of 6-fold coordination no longer form directed bonds but are held together by eletrostatic forces. In looking at binary crystals of increasing ionicity, the covalent bonding becomes weaker and the ionic bonding becomes stronger. When the amount of charge in the covalent bond goes to zero, there is no longer any particular need to form tetrahedrally directed bonds. Consequently, it is reasonable to speculate that a phase transition to a different crystalline structure occurs as the covalent bonding charge goes to zero. To test this hypothesis, the amount of covalent bonding charge for Ge, GaAs and ZnSe in plotted against Phillips' scale. The integral of the charge density in the bonds above the background value is called the bonding charge Z_b. This can be written as follows:

$$Z_b = \int (\rho(\underset{\sim}{r}) - \rho_o)\, d^3r, \qquad (5.2)$$

where ρ_o is the charge density at the outermost closed contour of the bonding charge density.[72] The integrations is also over the volume defined by this outermost contour.

The values obtained for Z_b are 0.146e for Ge, 0.080e for GaAs and 0.026e for ZnSe. As a check on these results, recall from Chapt. IV that the bonding charge in Ge can be approximated by $(2e/\varepsilon_o)$. The value of ε_o obtained from the band structure calculations is 14.0. This gives a bonding charge of 0.143e, which agrees with the above value of Z_b.

When the calculated values of Z_b are plotted against Phillips' ionicity scale and the points are connected by a smooth curve, the

extrapolated curve gives zero bonding at an ionicity of $f_c = 0.78$ (Fig. 44). A similar curve for the series Sn, InSb, and CdTe gives a critical ionicity of $f_c = 0.79$. These two values of the critical ionicity ($f_c = 0.78$ and $f_c = 0.79$) should be compared with Phillips' empirical value of the critical ionicity, namely, $f_c = 0.785 \pm 0.01$. Thus the calculated values of the crticial ionicity give complete separation of crystal types, just as Phillips' empirical value does.

When the bonding charge Z_b is plotted against Pauling's ionicity scale,[73] the curve passing through the series Ge, GaAs, and ZnSe gives a zero-covalent-bonding ionicity of 0.80, which is the empirically determined critical ionicity on Pauling's scale. The curve passing through the series Sn, InSb, and CdTe gives a critical ionicity of 0.61, which does not agree with Pauling's empirical value. For the crystals I have studied it appears that the ionicity scale of Phillips and Van Vechten is in better agreement with my results than the ionicity scale of Pauling.

ACKNOWLEDGEMENTS

I am grateful to my thesis adviser, Professor Marvin Cohen, for his guidance and encouragement throughout the entire course of this work. I am also grateful to Professor Ching-Yao Fong for the many helpful discussions which have helped to resolve problems arising in the course of my research.

I express my thanks to Professors Leo Falicov, Ron-Yuen Shen, Charles Kittel and Dr. J. C. Phillips for helpful discussions during various phases of my research. I also thank the many graduate students and post-doctoral fellows with whom I have discussed many problems. Among these I especially thank Pieter Visscher, Robert Cahn, Dr. Yvonne Tsang, and Dr. Phillip Allen.

I appreciate the help of Mary Horney and Jane Ball in preparing this manuscript. I gratefully acknowledge the computer support given by the Inorganic Materials Research Division, of the Lawrence Radiation Laboratory and the four years of financial support given to me as a National Science Foundation Graduate Fellow.

REFERENCES

1. J. C. Phillips and L. Kleinman, Phys. Rev. 116, 287 (1959); L. Kleinman and J. C. Phillips, Phys. Rev. 118, 1153 (1960).
2. M. H. Cohen and V. Heine, Phys. Rev. 122, 1821 (1961).
3. B. J. Austin, V. Heine, and L. J. Sham, Phys. Rev. 127, 276 (1962).
4. V. Heine and I. Abarenkov, Phil. Mag. 9, 451 (1964); A.O.E. Animalu, ibid. 11, 379 (1965); I. Abarenkov and V. Heine, ibid. 529 (1965); A.O.E. Animalu and V. Heine, ibid. 12, 1249 (1965).
5. M. L. Cohen and T. K. Bergstesser, Phys. Rev. 141, 789 (1966).
6. T. K. Bergstresser, Ph.D. Thesis, University of California, Berkeley 1966.
7. J. P. Walter and M. L. Cohen, Phys. Rev. 183, 763 (1969); J. P. Walter, M. L. Cohen, Y. Petroff, and M. Balkanski, Phys. Rev. B1, 2261 (1970).
8. R. N. Cahn and M. L. Cohen, Phys. Rev. B1, 2569 (1970); Y. W. Tung and M. L. Cohen, Phys. Rev. 180, 823 (1969); C. Y. Fong and M. L. Cohen, Phys. Rev. 185, 1168 (1969).
9. D. L. Greenaway, Phys. Rev. Letters 9, 97 (1962).
10. H. R. Phillip and H. Ehrenreich, Phys. Rev. 129, 1550 (1963).
11. M. Aven, T. F. Marple, and B. Segall, J. Appl. Phys. (Suppl.) 32, 2261 (1961).
12. M. Cardona and G. Harbeke, in Proceedings of the Seventh International Conference on the Physics of Semiconductors, (Dunod, Paris, 1964), p. 127.

13. A. G. Thompson, M. Cardona, K. L. Shaklee, and J. C. Wolley, Phys. Rev. 146, 601 (1966).

14. F. H. Pollak, M. Cardona, and J. Barber, to be published.

15. J. W. Baars, II-VI Semiconducting Compounds, 1967 International Conference, edited by D. G. Thomas, (W. A. Benjamin, Inc., New York, 1967), p. 631.

16. R. C. Eden, Stanford Electronics Laboratory, Tech. Rep. 5222-1,1967.

17. E. Matatagui, A. G. Thompson, and M. Cardona, Phys. Rev. 176, 950 (1968).

18. S. S. Vishnubhatla and J. C. Woolley, Can. J. Phys. 46, 1769 (1968).

19. Y. Petroff, M. Balkansii, J. P. Walter, and M. L. Cohen, Solid State Commun. 7, 459 (1969).

20. W. Saslow, T. K. Bergstresser, C. Y. Fong, M. L. Cohen, and D. Brust, Solid State Comm. 5, 667 (1967).

21. J. B. Rosen, J. Soc. Indust. Appl. Math. 8, 181 (1960).

22. C. Y. Fong, W. Saslow, and M. L. Cohen, Phys. Rev. 168, 992 (1968).

23. J. C. Phillips, in Solid State Physics, edited by F. Seitz and D. Turnbull (Academic Press Inc., New York, 1965), Vol. 18.

24. K. L. Shaklee, J. E. Rowe, and M. Cardona, Phys. Rev. 174, 828 (1968).

25. The experimental data of G. Gobeli and F. Allen appears in M. L. Cohen and J. C. Phillips, Phys. Rev. 139, A912(1965).

26. M. Cardona and D. L. Greenaway, Phys. Rev. 131, 98 (1963).

27. Y. Petroff, M. Balkanski, J. P. Walter, and M. L. Cohen, Solid State Comm. 7, 459 (1969).

28. M. Cardona, K. L. Shaklee, and F. H. Pollak, Phys. Rev. 154, 696 (1967).

29. R. R. L. Zucca and Y. R. Shen, Phys. Rev. B 1, 2668 (1970).

30. The symmetry notations for the bands are different because the spin-free symmetry is in single-group notation, whereas the spin-orbit symmetry is in double-group notation.

31. G. Weisz, Phys. Rev. 149, 504 (1966).

32. S. Bloom and T. K. Bergstresser, Solid State Comm. 6, 465 (1968); T. K. Bergstresser, (private communication).

33. F. Herman and S. Skillman, Atomic Structure Calculations, (Prentice-Hall, Inc., Englewood Cliffs, N.J., 1966).

34. P. Eckelt, Solid State Comm. 6, 489 (1968), and references therein.

35. This particular notation will be used only for ZnTe and ZnSe. These two crystals have large spin-orbit splittings, which can split normally spin-degenerate bands by as much as 0.2 eV. The bands are numbered consecutively, with the highest energy valence band numbered 8. The bands are doubly degenerate in Δ and Λ directions, except for an extremely small splitting at L_4, L_5. Accordingly, a label (8-10)in one of these directions also includes transitions (7-9), (7-10), and (8-9). The proper group notation is used only where such labeling is unambiguous.

36. J. P. Walter, M. L. Cohen, Y. Petroff and M. Balkanski, Phys. Rev. B1, 2661 (1970).

37. D. L. Greenaway and M. Cardona, in Proceedings: International Conference on the Physics of Semiconductors (The Institute of Physics and the Physical Society, London, 1962), p. 666.

38. A. Bardasis and D. Hone, Phys. Rev. 153, 849 (1967).

39. M. Cardona, Modulation Spectroscopy, Solid State Physics, Suppl. 11 (Academic Press, New York, 1969).

40. M. D. Sturge, Phys. Rev. 127, 768 (1962).

41. R. R. L. Zucca, J. P. Walter , Y. R. Shen, M. L. Cohen, Solid State Commun. 8, 627 (1970).

42. L. R. Saravia and D. Brust; Phys. Rev. 171, 916 (1968).

43. This result is true for GaAs and is generally true for all cubic semiconductors because of their similarity to GaAs.

44. See C. Keffer, T. M. Hayes, and A. Bienenstock, Phys. Rev. Letters, 21, 1676 (1968).

45. R. J. Glauber, Phys. Rev. 98, 1692 (1955). Some important points are not easily understood without reference to his earlier paper: Ibid. 84, 395 (1951).

46. See, for example, C. Kittel, Introduction to Solid State Physics, 3rd edition. (J. Wiley and Sons, Inc., New York, 1966), p. 68-70.

47. J. P. Walter, R. R. L. Zucca, M. L. Cohen, and Y. R. Shen, Phys. Rev. Letters 24, 102 (1970).

48. S. I. Novikova, Fiz. Tverd. Tela 3, 178 (1961), [translation: Soviet Phys. Solid State 3, 129 (1961)].

49. J. C. Phillips, Phys. Rev. 113, 147 (1959).

50. G. is in units of $(2\pi/a)$.

51. B. W. Batterman and D. R. Chipman, Phys. Rev. 127, 690 (1962).

52. F. Oswald, Z. Naturforsch. 10a, 927 (1955).

53. M. D. Sturge, Phys. Rev. 127, 768 (1962).

54. W. Paul, J. Appl. Phys. Suppl. 32, 2082 (1961).

54a. H. Ehrenreich and M. H. Cohen, Phys. Rev. 115, 786 (1959).

55. D. R. Penn, Phys. Rev. 128, 2093 (1962).

56. G. Srinivasan, Phys. Rev. 178, 1244 (1969).

57. H. Nara, J. Phys. Soc. Japan 20, 778 (1965); H. Nara, J. Phys. Soc. Japan 20, 1097 (1965).

58. R. M. Martin , Phys. Rev. Letters 21, 536 (1968).

59. J. C. Phillips, Phys. Rev. 166, 832 (1968).

60. A. Morita and H. Nara, J. Phys. Soc. Japan 21 (Suppl), 234 (1966).

61. The calculations of $\varepsilon(0)$ were done in conjunction with the reflectivity calculations of Chapts.I and II.

62. M. Renninger, Acta. Cryst. 8, 606 (1955).

63. W. C. Dunlop, Jr., and R. L. Watters, Phys. Rev. 92,1396 (1953).

64. K. G. Hambleton, C. Hilsum, and B. R. Holeman, Proc. Phys. Soc. (London) 77, 1147 (1961).

65. E. Bernstein, Proceedings of the Conference on the Physics of Semimetals and Narrow Gap Semiconductors, Dallas 1970,to be published.

66. A. O. E. Animalu and V. Heine, Phil. Mag. 12, 1249 (1965).

67. V. Heine and I. Abarenkov, Phil. Mag. 9, 451 (1964).

68. J. Hubbard, Proc. Roy. Soc. (London) A243, 336 (1958).

69. D. Brust, M. L. Cohen and J. C. Phillips, Phys. Rev. Letters 9, 389 (1962).

70. A. Streitweiser, Jr., Molecular Orbital Theory for Organic Chemists (Wiley, New York, 1961).

71. J. C. Phillips, Rev. Modern Phys. 42, 317 (1970).

72. The chief difficulty is obtaining a measure of the bonding charge against a complicated background. The method used here is simple

simple and gives the expected value of the bonding charge for Ge.

73. L. Pauling, The Nature of the Chemical Bond, (Cornell Univ. Press, Ithaca, New York), 1939. Discussion of Pauling's ionicity scale is also included in Ref. 71.

Table I. The lattice constants and form factors (in Ry) for the semiconductors discussed in this thesis. They should be compared with those used in Ref. 5.

	Lattice Constant	$V^S(3)$	$V^S(8)$	$V^S(11)$	$V^A(3)$	$V^A(4)$	$V^A(11)$	Metallic Spin-Orbit Factor
GaAs	5.640	-0.246	-0.001	0.074	0.058	0.051	0.001	0.0009
GaP	5.44	-0.225	0.024	0.076	0.128	0.053	0.020	...
ZnS	5.41	-0.249	0.038	0.053	0.195	0.116	0.015	...
ZnTe	6.07	-0.217	-0.018	0.069	0.116	0.073	-0.011	0.0010
ZnSe	5.65	-0.213	-0.011	0.067	0.203	0.107	0.015	0.0006
Si	5.43	-0.21	0.04	0.08	0.	0.	0.	...
Ge	5.66	-0.23	0.01	0.06	0.	0.	0.	...

Table II. Theoretical and experimental reflectivity structure and their identifications, including the location in the Brillouin zone, energy, and symmetry of the calculated critical points for GaAs. The experimental results are due to H. Philipp and H. Ehrenreich and appear in Ref. 16.

Reflectivity Structure (eV)		Associated Critical Points		
Theory	Experiment	Location in Zone	Symmetry	CP Energy(eV)
-	1.48	$\Gamma_{15} - \Gamma_1$(0.,0.,0.)	M_o	1.46
2.95	2.88, 3.15 (spin orbit)	$L_3 - L_1$ (.5,.5,.5)	M_o	2.69
		$\Lambda_3 - \Lambda_3$ (.21,.21,.21)	M_1	2.93
4.45	4.55	$\Delta_5 - \Delta_1$ (.60,0.,0.) (band 4 to band 5)	M_o	4.10
		$X_5 - X_1$ (1.,0.,0.)	M_1^o	4.34
4.85	5.00	$\Delta_5 - \Delta_1$ (.35,0.,0.) (band 4 to band 5)	M_1	4.23
		$\Sigma_2 - \Sigma_1$ (.58,.58,0.)	M_2	4.76
5.65	5.55*	$\Delta_5 - \Delta_1$ (.50,0.,0.) (band 4 to band 6)	M_1	5.69
6.45	6.6	Volume effect from region around (.57,.43,.29) (band 4 to band 6)	-	6.35
		$L_3 - L_3$(.5,.5,.5)	M_2	6.45
6.75	6.6	$\Lambda_3 - \Lambda_3$ (.43,.43,.43) (band 3 to band 6 and band 4 to band 7)	M_1	6.51
		$\Lambda_3 - \Lambda_3$ (.43,.43,.43) (band 4 to band 6)	M_3	6.51

* This shoulder appears in data of Greenaway (Ref. 9).

Table III. Theoretical and experimental reflectivity structure and their identifications, including the location in the Brillouin zone, energy, and symmetry of the calculated critical points for GaP. The experimental results are due to H. Philipp and H. Ehrenreich and appear in Ref. 16.

Reflectivity Structure(eV)		Associated Critical Points		
Theory	Experiment	Location in Zone	Symmetry	CP Energy (eV)
-	2.80	$\Gamma_{15} - \Gamma_1$ (0.,0.,0.)	M_o	2.79
3.70	3.70	$L_3 - L_1$ (.5,.5,.5)	M_o	3.40
		$\Lambda_3 - \Lambda_1$ (.15,.15,.15)	M_1	3.76
4.7	4.6	$\Delta_5 - \Delta_1$ (.71,0.,0.) (band 4 to band 5)	M_o	4.50
		$X_5 - X_1$ (1., 0., 0.)	M_1	4.57
5.3	5.3	$\Delta_5 - \Delta_1$ (.30,0,0.) (band 4 to band 5)	M_3	4.72
		$\Sigma_2 - \Sigma_1$ (.50,.50,0.)	M_2	5.20
6.7	6.9	volume effect from region around (.50,.43,.29) (band 4 to band 6)	-	6.5
		$L_3 - L_3$ (.5,.5,.5)	M_2	6.57
6.9	6.9	$\Lambda_3 - \Lambda_3$ (.37,.37,.37) (band 3 to band 6 and band 4 to band 7)	M_1	6.68
		$\Lambda_3 - \Lambda_3$ (.37,.37,.37) (band 4 to band 6)	M_3	6.68

Table IV. Theoretical and experimental reflectivity structure and their identifications, including the location in the Brillouin zone, energy, and symmetry of the calculated critical points for ZnS. Experiment 1 refers to Cardona and Harbeke (Ref. 12). Experiment 2 refers to J. W. Baars (Ref. 15).

Reflectivity Structure (eV)			Associated Critical Points		
Theory	Experiment 1	Experiment 2	Location in Zone	Symmetry	CP Energy(eV)
3.8	3.66, 3.76 (spin orbit)	3.68, 3.75 (spin orbit)	$\Gamma_{15} - \Gamma_1$ (0.,0.,0.)	M_o	3.74
5.55	5.79	5.78	$L_3 - L_1$ (.5,.5,.5)	M_o	5.40
			$\Lambda_3 - \Lambda_1$ (.32,.32,.32)	M_1	5.52
6.6	-	-	$X_5 - X_1$ (1.,0.,0.)	M_o	6.31
7.05	6.99	7.02	$\Delta_5 - \Delta_1$ (.50,0.,0.) (band 4 to band 5)	M_1	6.99
			$\Sigma_2 - \Sigma_1$ (.53,.53,0.)	M_2	7.08
7.55	7.41	7.5	$\Delta_5 - \Delta_1$ (.37,0.0.) (band 4 to band 6)	M_o	7.45
			$\Delta_5 - \Delta_1$ (.51,0.,0.) (band 4 to band 6)	M_1	7.57
-	-	-	$\Gamma_{15} - \Gamma_{15}$	degenerate	7.79
8.45	-	8.35	Volume effect from region around (.57,.36,.14) (band 4 to band 6)	-	8.35
9.15	-	9.0	$\Lambda_3 - \Lambda_3$ (.29,.29,.29) (band 3 to band 6)	M_1	8.64
			Volume effect (bands 3 to 6 and bands 4 to 7)	-	8.85
9.75	9.8	9.6	Volume effect (bands 3 to 6 and bands 4 to 7)	-	9.5

Table V. Calculated spin-orbit splitting (in eV) in the single-group notation for ZnTe, ZnSe and GaAs. Si was deleted because of its negligible spin-orbit splittings. The single spin-orbit parameter was determined by adjusting the 15V splitting to agree with experiment.

	ZnTe	ZnSe	GaAs
Γ_{15V}	0.92	0.45	0.35
L_{3V}	0.58	0.29	0.23
X_{5V}	0.46	0.25	0.12
Γ_{15C}	0.16	0.05	0.15
L_{3C}	0.07	0.02	0.06

Table VI. Theoretical and experimental reflectivity structure at 300°K and their identifications, including location in the Brillouin zone, energy and symmetry of the calculated critical points for ZnTe. See Ref. 35 for an explanation of the notation

Reflectivity Structure (eV)		Associated Transitions		
Theory	Experiment	Location in Zone	Symmetry	Transition Energy (eV)
2.20	---	Γ_8-Γ_6	M_0	2.21
---	---	Γ_7-Γ_6	M_0	3.14
3.70	3.58	L_4,L_5-L_6	M_0	3.45
		Λ(8-10)(0.3,0.3,0.3)	M_1	3.64
4.15	3.99	L_6-L_6	M_0	4.03
4.30	4.18	Λ(6-10)(0.3,0.3,0.3)	M_1	4.21
4.65	---	X_7-X_6	M_0	4.59
4.95	4.92	Δ(8-10)(0.5,0.,0.)	M_1	4.93
5.25	---	K(8-9)	M_0	5.26
5.45	5.51	K(7-10)	M_0	5.35
		Δ(6-10)(0.5,0.,0.)	M_1	5.39
		Σ(7-10)(0.6,0.6,0.)	M_2	5.50
5.85	5.9	Δ(8-12)(0.6,0.,0.)	M_1	5.67
6.10	---	Δ(6-12)(0.6,0.,0.)	M_2	6.13
6.85	6.87	Vol. effect (7-12) and (8-11) from region around (0.6,0.4,0.3)	--	6.72
		Vol. effect (6-11)(0.6,0.4,0.3)	--	7.28
7.65	7.58	Vol. effect (5-12)(0.6,0.4,0.3)	--	7.47
		Λ(6-13)(0.4,0.4,0.4)	M_1	7.57

Table VII. Theoretical and experimental reflectivity structure at 300°K and their identifications, including location in the Brillouin zone, energy, and symmetry of the calculated critical points for ZnSe. See Ref. 35 for an explanation of the notation.

Reflectivity Structure (eV)		Associated Transitions		
Theory	Experiment	Location Zone	Symmetry	Transition Energy (eV)
2.80	---	Γ_8-Γ_6	M_0	2.77
3.20	---	Γ_7-Γ_6	M_0	3.22
4.72	4.75	L_4,L_5-L_6	M_0	4.53
		Λ(8-10)(0.3,0.3,0.3)	M_1	4.64
5.00	5.05	L_6-L_6	M_0	4.82
		Λ(6-10)(0.3,0.3,0.3)	M_1	4.94
5.97	6.00	X_7-X_6	M_0	5.92
6.20	---	Δ(8-10)(0.6,0.,0.)	M_1	6.11
6.47	6.50	Δ(6-10)(0.6,0.,0.)	M_1	6.37
		Comes chiefly from the sum of Δ(8-10),Σ(7-9), and Σ(8-10) transitions		
6.62	6.63	Σ(7-9) and (8-10), both at (0.6,0.6,0.)	M_2	6.62
7.10	7.15	Δ(8-12)(0.6,0.,0.)	M_1	7.02
7.42	7.60	Δ(6-12)(0.6,0.,0.)	M_1	7.28
7.67		Σ(6-12)(0.2,0.2,0.)	M_2	7.60
7.88	7.80	Γ_8-Γ_8	---	7.80
8.20	8.46	Vol. effect (8-12) and (7-11) (0.6,0.5,0.2)		8.13
8.50		L(8-12)	---	8.51
8.85	8.97	Vol. effect (5-12),(6-11),(5-11) and (6-12)(0.6,0.5,0.2)		8.80
		Λ(8-14)(0.3,0.3,0.3)		8.69

Table VIII. Theoretical and experimental reflectivity structure at 5°K and their identifications, including the location in the Brillouin zone, energy, and symmetry of the calculated critical points for GaAs.

Reflectivity Structure (eV)		Associated Critical Points		
Theory	Experiment	Location in Zone	Symmetry	CP Energy(eV)
1.52	1.52[a]	Γ_8-Γ_6 (0.,0.,0)	M_0	1.52
2.90	---	L(4-5) (0.5,0.5,0.5)	M_0	2.83
3.05	3.02	Λ(4-5) (0.2,0.2,0.2)	M_1	3.02
3.25	3.24	Λ(3-5) (0.2,0.2,0.2)	M_1	3.25
4.35	4.44	Δ(4-5) (0.6,0.,0.)	M_0	4.23
4.50	4.60	Δ(3-5) (0.6,0.,0.)	M_0	4.36
4.60		Δ(4-5) (0.2,0.,0.)	M_1	4.38
4.78		Δ(3-5) (0.2,0.,0.)	M_1	4.55
4.94	5.11	Σ(4-5) (0.6,0.6,0.)	M_2	4.88
5.85	5.91	Δ(4-6) (0.5,0.,0.)	M_1	5.67
		Δ(3-6) (0.5,0.,0.)	M_1	5.81

[a]M. D. Sturge, Phys. Rev. 127, 768 (1962).

TABLE IX. Theoretical and experimental reflectivity structure at 5°K and their identifications, including the location in the Brillouin zone, energy, and symmetry of the calculated critical points for Si.

Reflectivity Structure (eV)		Associated Critical Points		
Theory	Experiment	Location in Zone	Symmetry	CP Energy (eV)
3.13	---	L(4-5) (0.5,0.5,0.5)	M_0	3.13
3.35	3.40	(4-5) transitions near	--	
		(0.3,0.3,0.2)	--	3.26
		Δ(4-5) (0.1,0.,0.)	--	3.42
3.46	3.45	Λ(4-5) (0.1,0.1,0.1)	M_1	3.46
3.68	3.66	(3-5) transitions near		
		(0.2,0.1,0.1)	M_2	3.77
4.11		(4-5) transitions near		
		(1.0,0.,0.)	M_1	3.97
4.22	4.30	(3-5) transitions near		
		(0.3,0.2,0.1)	--	4.10
4.51	4.57	Σ(4-5) (0.4,0.4,0.)	M_2	4.41
5.38	5.48	(4-6) transitions near		
		(0.6,0.4,0.3)	--	5.29

Table X. Fundamental gap of GaAs as function of temperature. Experiment 1 is due to F. Oswald (Ref. 52). Experiment 2 is due to M. D. Sturge (Ref. 53).

Temperature (°K)	Theory (eV)	Experiment 1 (eV)	Experiment 2 (eV)
5	1.52	1.53	1.52
80	1.50	1.49	1.51
150	1.46	1.45	1.49
225	1.41	1.42	1.46
300	1.36	1.38	1.43

FIGURE CAPTIONS

1. Brillouin zone for fcc lattice with symmetry points and lines.
2. Band structure of GaAs along the principle symmetry directions.
3. Theoretical $\varepsilon_2(\omega)$ for GaAs. The tail function begins at 8.85 eV.
4. A comparison of theoretical and experimental $R(\omega)$ for GaAs. The experimental results are due to Phillip and Ehrenreich and appear in Ref. 10. The tail function begins at 8.85 for $\varepsilon_2(\omega)$.
5. A comparison for GaAs of theoretical $\Delta R/R(\omega)$ with thermoreflectance measurements by Matatagui, et al. (Ref. 17).
6. Band structure of GaP along the principle symmetry directions.
7. Theoretical $\varepsilon_2(\omega)$ for GaP. The tail function begins at 8.95 eV.
8. A comparison of theoretical and experimental $R(\omega)$ for GaP. The experimental results are due to Phillip and Ehrenreich and appear in Ref. 10. The tail function begins at 8.95 eV for $\varepsilon_2(\omega)$.
9. A comparison for GaP of theoretical $\Delta R/R(\omega)$ with thermoreflectance measurements by Matatagui, et. al. (Ref. 17).
10. Band structure for ZnS along the principle symmetry directions.
11. Theoretical $\varepsilon_2(\omega)$ for ZnS. The tail function begins at 10.95 eV.
12. A comparison of theoretical and experimental $R(\omega)$ for ZnS. Experiment 1 refers to Cardona and Harbeke (Ref. 12). Experiment 2 refers to J. W. Baars (Ref. 15). The tail function begins at 10.95 eV.
13. Band structure of GaAs along the principal symmetry directions. Spin-orbit interactions have been included.
14. Band structure of ZnTe along the principal symmetry directions. Spin-orbit interactions have been included.

15. Theoretical $\varepsilon_2(\omega)$ for ZnTe, with and without spin-orbit contributions. The tail function begins at 8.83 eV.

16. A comparison of theoretical and experimental $R(\omega)$ for ZnTe at 300°K. The tail function begins at 8.83 eV. Experimental results are due to Y. Petroff and M. Balkanski (Ref. 36).

17. A comparison for ZnTe of theoretical $R'(\omega)/R(\omega)$ with thermo-reflectance measurements by Matatagui, et al. (Ref. 17). The experimental measurements are multiplied by a constant scale factor.

18. Band structure for ZnSe along the principal symmetry directions. Spin-orbit interactions have been included.

19. Theoretical $\varepsilon_2(\omega)$ for ZnSe, with and without spin-orbit contributions. The tail function begins at 9.93 eV.

20. A comparison of theoretical and experimental $R(\omega)$ for ZnSe at 300°K. The experimental results are due to Y. Petroff and M. Balkanski (Ref. 27). The tail function begins at 9.93 eV.

21. A comparison for ZnSe of theoretical $R'(\omega)/R(\omega)$ with thermo-reflectance measurements by Matatagui, et al. (Ref. 17). The experimental measurements are multiplied by a constant scale factor.

22. The experimental reflectivity (percent) for ZnTe and ZnSe at 15°K. (Due to Petroff and Balkanski, Ref. 36).

23. A composite $\varepsilon_2(\omega)$ of direct transitions from 0.to 6.4 eV, of indirect transitions from 12.0 to 14.0 eV, and of a linear combination of direct and indirect transitions from 6.4 to 12.0 eV.

24. The theoretical reflectivity is calculated from $\varepsilon_2(\omega)$ shown in Fig. 23. The experimental $R(\omega)$ is due to Y. Petroff and M. Balkanski (Ref. 27).

25. A comparison of theoretical and experimental modulated reflectivity for GaAs. The transitions which cause the major reflectivity peaks are identified. The experimental results are due to Zucca and Shen (Ref. 41).

26. A comparison of theoretical and experimental modulated reflectivity for Si. The transitions which cause the major reflectivity peaks are identified. The experimental results are due to Zucca and Shen (Ref. 41).

27. Plots of $R'(\omega)/R(\omega)$ in the regions of the E_1 doublet peaks and the E_2 major peak. Plots 1 through 5 refer to temperatures of 5, 80, 150, 225, and 300K, respectively. (Due to Zucca and Shen, Ref. 47).

28. Plots of the explicit temperature dependence of the experimental E_1 and E_2 reflectivity peaks and of the corresponding theoretically calculated, $\Lambda(4\text{-}5)$, $\Lambda(3\text{-}5)$ and $\Sigma(4\text{-}5)$ transitions.

29. Our calculation of the microscopic longitudinal dielectric function of silicon is compared with the calculations by Srinivasan (Ref. 56) and by Nara (Ref. 57).

30. Calculated microscopic dielectric function of Si along two symmetry directions. $\varepsilon(\underset{\sim}{q})$ for $\underset{\sim}{q}$ along (1,1,0) is essentially the same as for $\underset{\sim}{q}$ along (1,0,0).

31. Calculated microscopic dielectric function of Ge along two symmetry directions. $\varepsilon(\underset{\sim}{q})$ for $\underset{\sim}{q}$ along (1,1,0) is essentially the same as for $\underset{\sim}{q}$ along (1,0,0).

32. Calculated microscopic dielectric function of GaAs along two symmetry directions. $\varepsilon(\underset{\sim}{q})$ for $\underset{\sim}{q}$ along (1,1,0) is essentially the same as for $\underset{\sim}{q}$ along (1,0,0).

33. Calculated microscopic dielectric function of ZnSe along two symmetry directions. $\varepsilon(\underset{\sim}{q})$ for $\underset{\sim}{q}$ along (1,1,0) is essentially the same as for $\underset{\sim}{q}$ along (1,0,0).

34. Orientation of contour plane with respect to the primitive cell and the surrounding atoms.

35. Contour plot for Ge of the total valence electron density in units of (e/Ω).

36. Contour plot for GaAs of the total valence electron density in units of (e/Ω).

37. Contour plot for ZnSe of the total valence electron density in units of (e/Ω).

38. Contour plot for Ge of the electron density in the first valence band.

39. Contour plot for Ge of the electron density in the fourth valence band.

40. Contour plot for GaAs of the electron density in the first valence band.

41. Contour plot for GaAs of the electron density in the second valence band.

42. Contour plot for GaAs of the electron density in the fourth valence band.

43. Contour plot for ZnSe of the hypothetical electron density in the first conduction band.

44. Bonding charge versus Phillips' ionicity scale. The bonding charge is in units of e per bond.

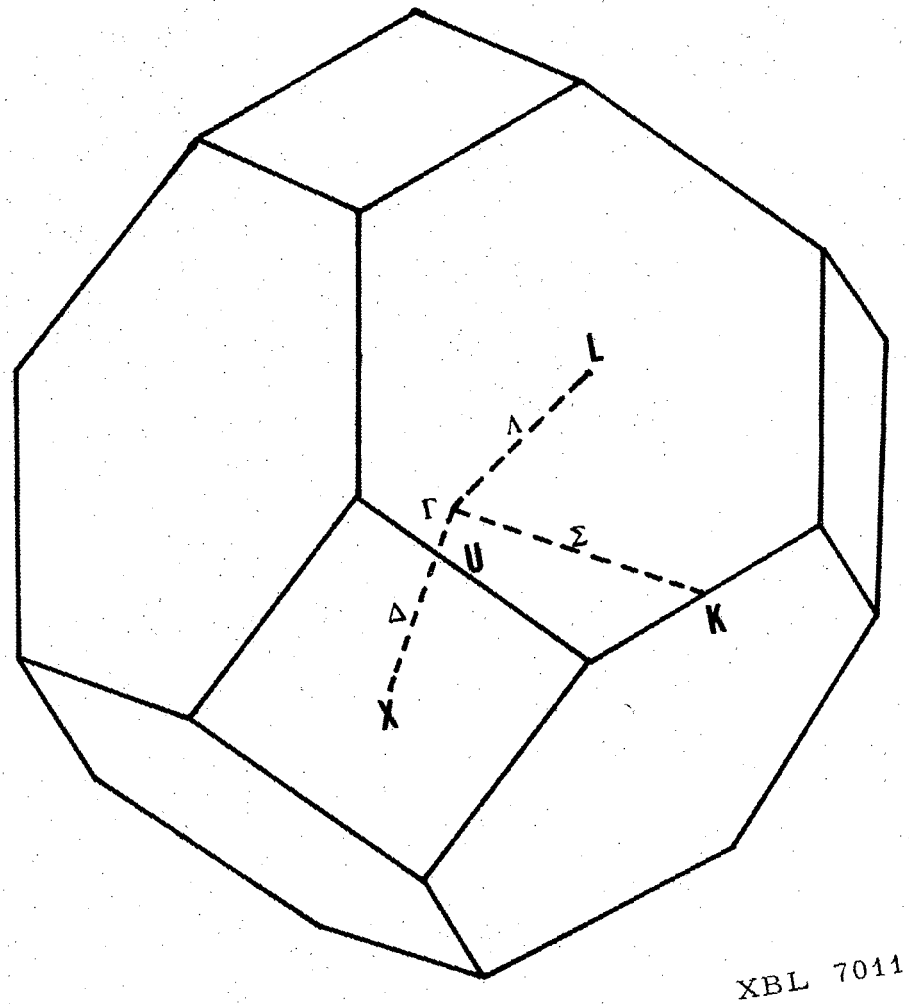

XBL 7011-6982

Figure 1

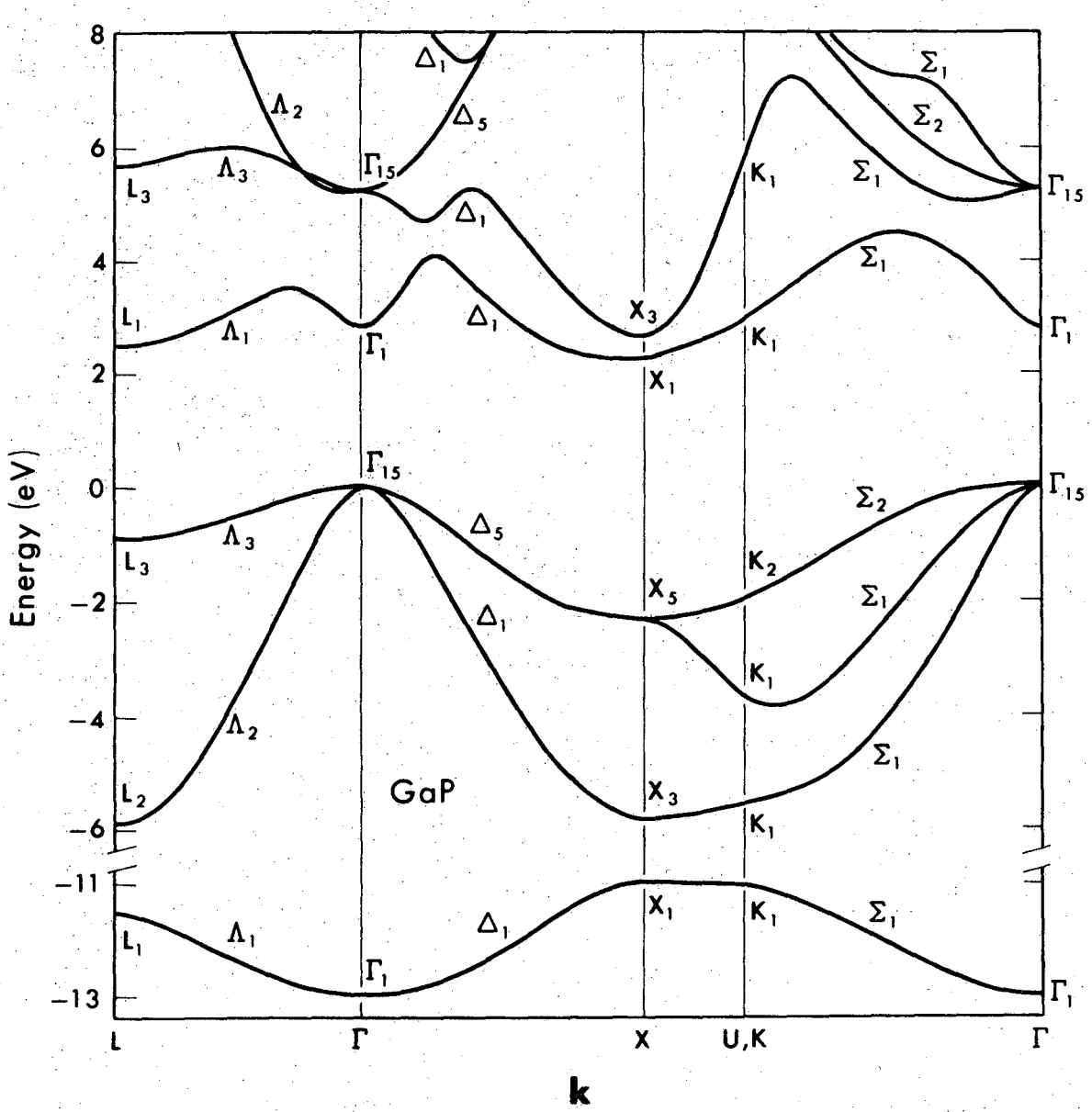

XBL 7011-6991

Figure 2

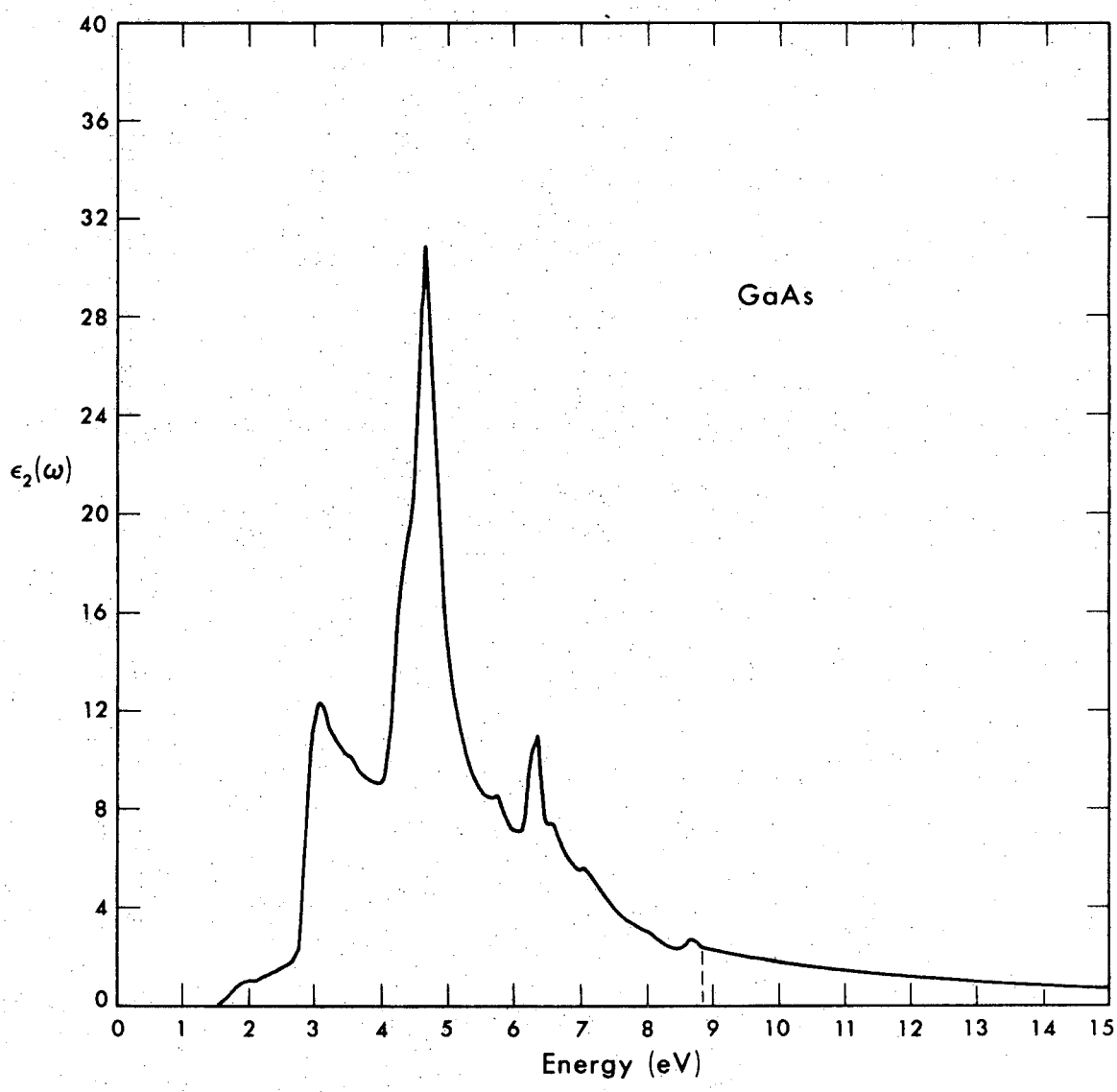

XBL 7011-6974

Figure 3

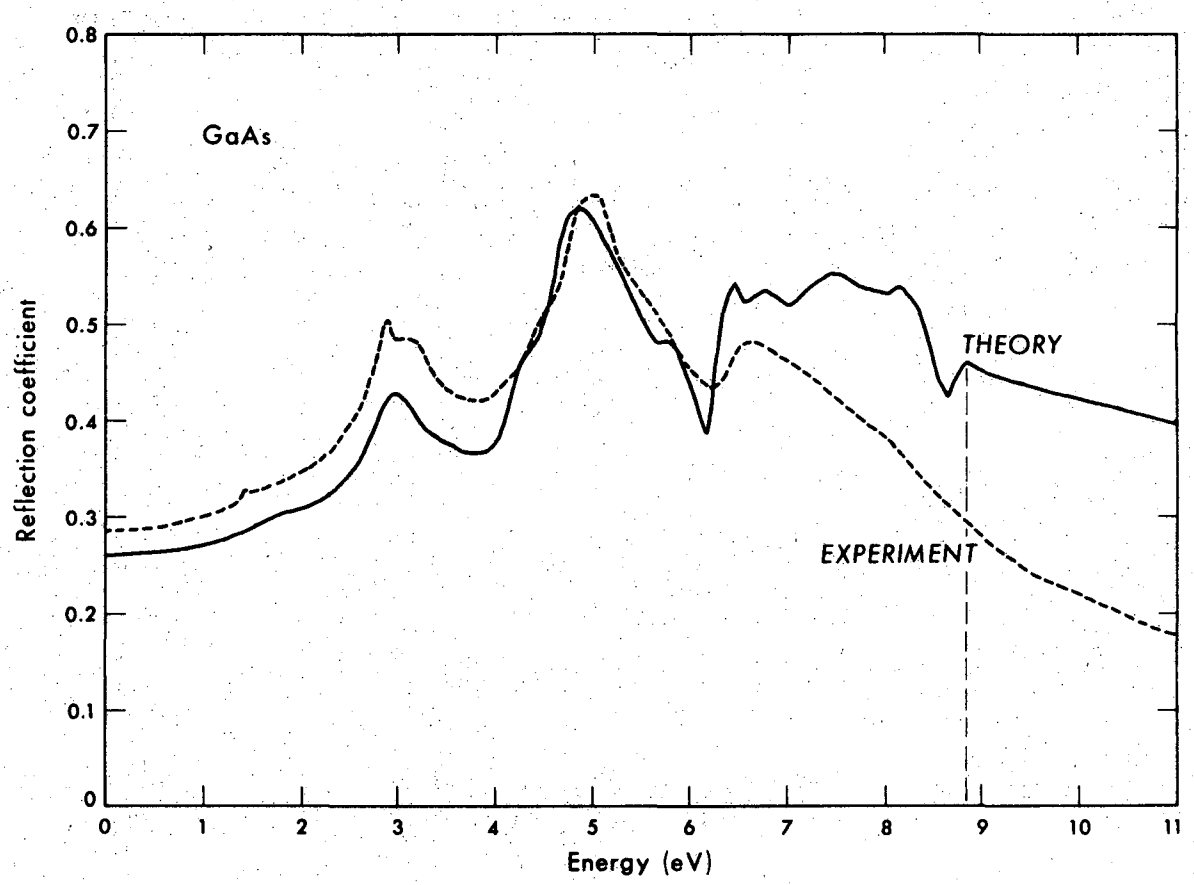

XBL 7011-6976

Figure 4

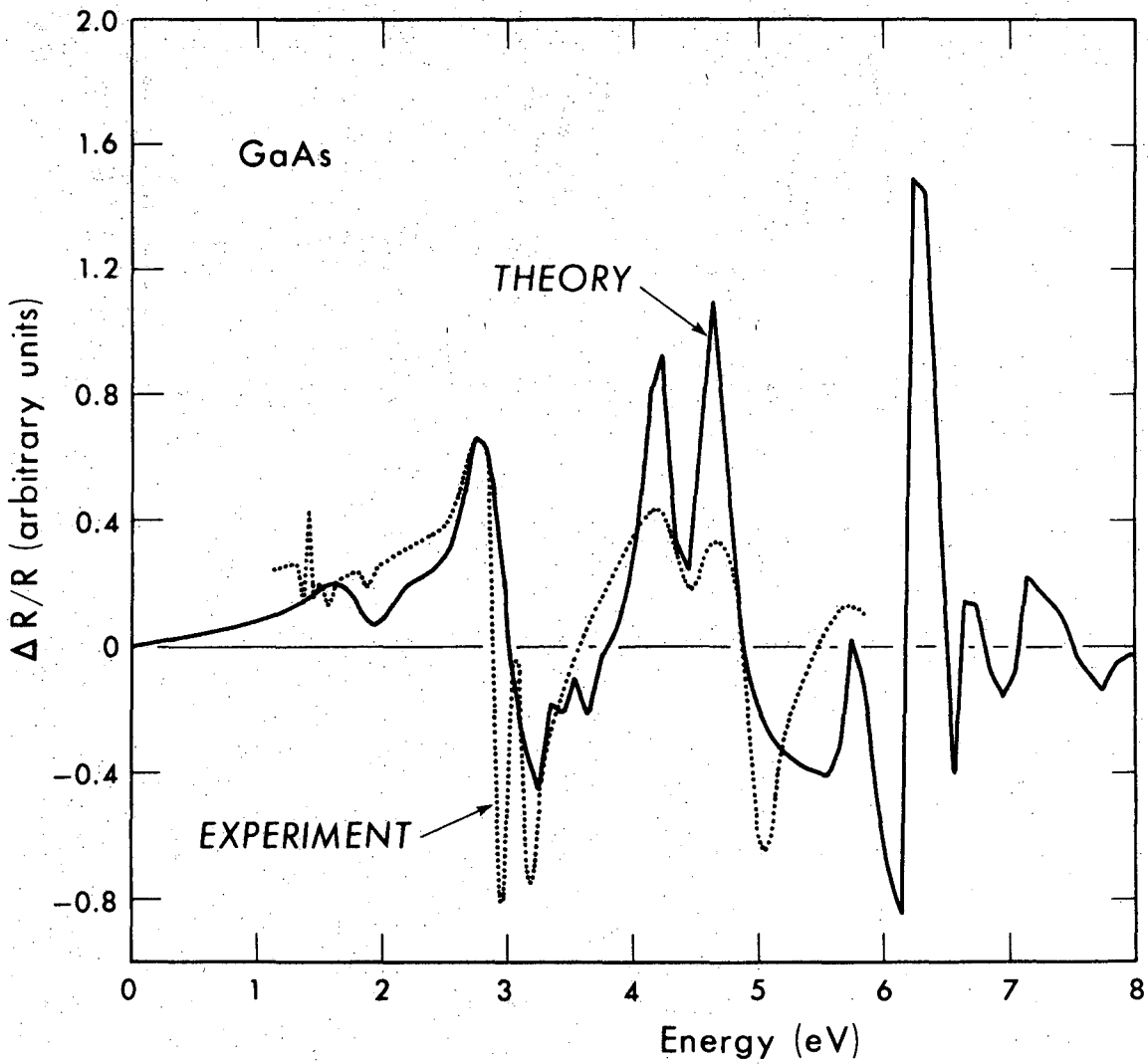

XBL 7011-6990

Figure 5

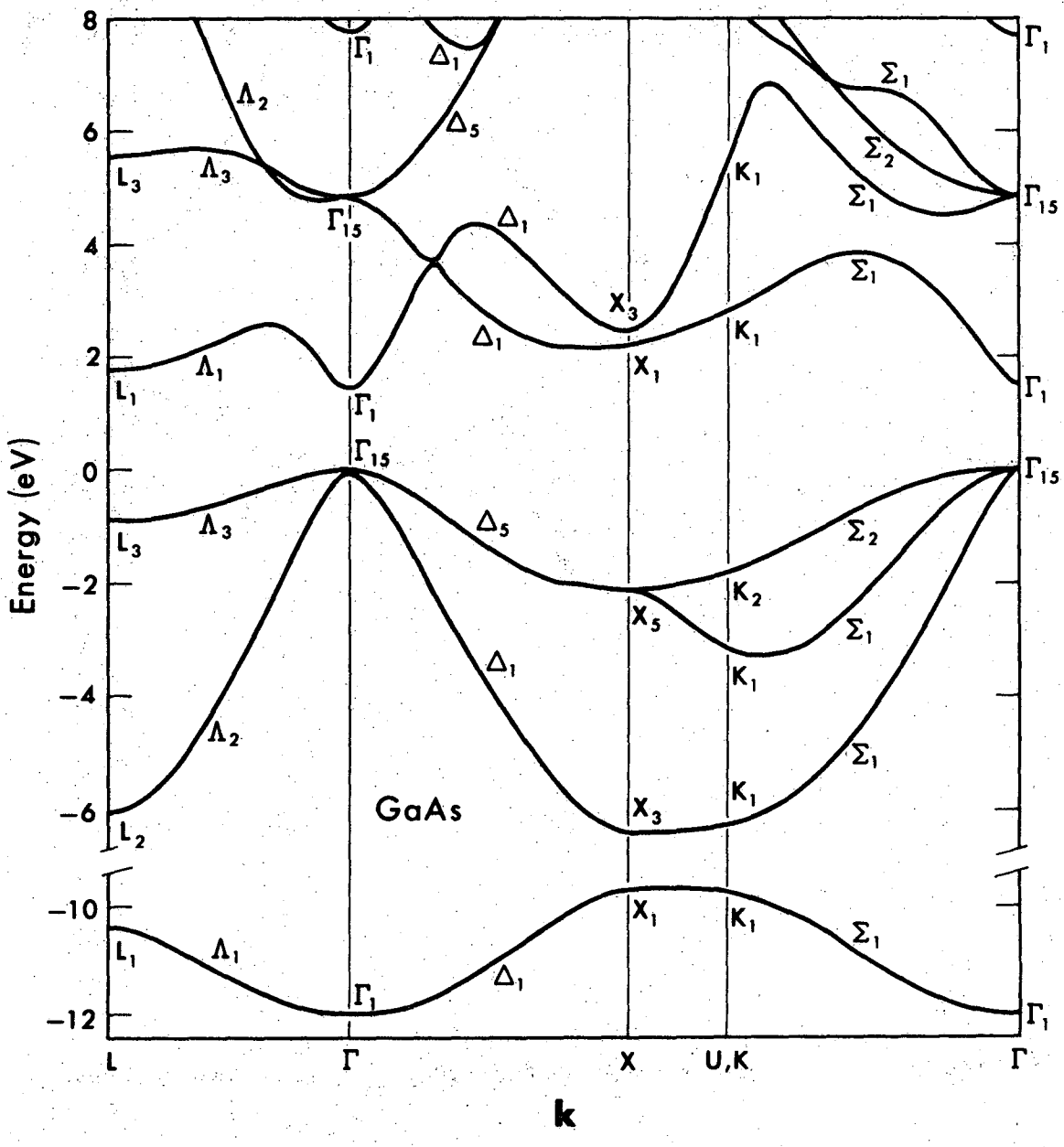

XBL 7011-6977

Figure 6

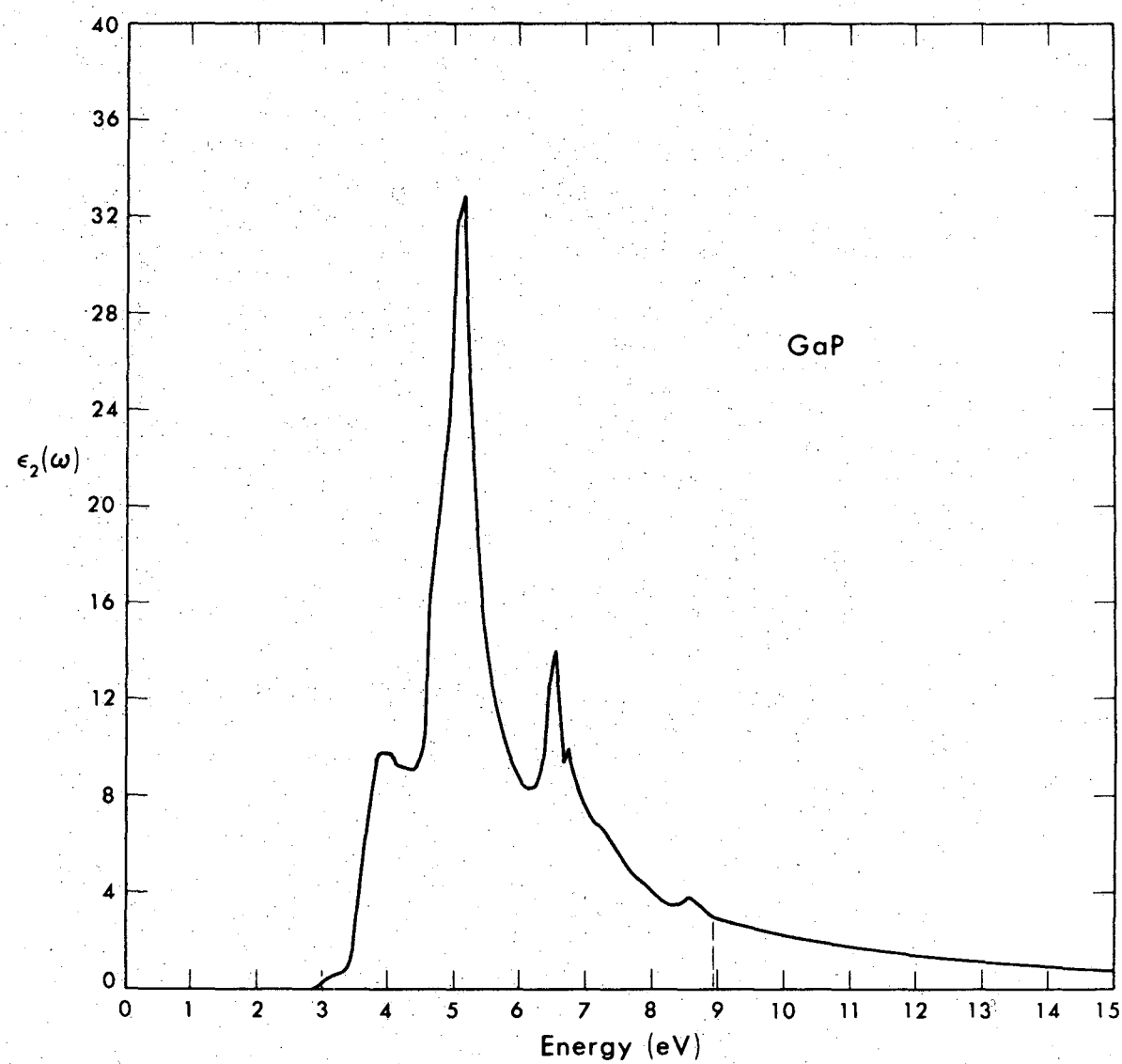

XBL 7011-6992

Figure 7

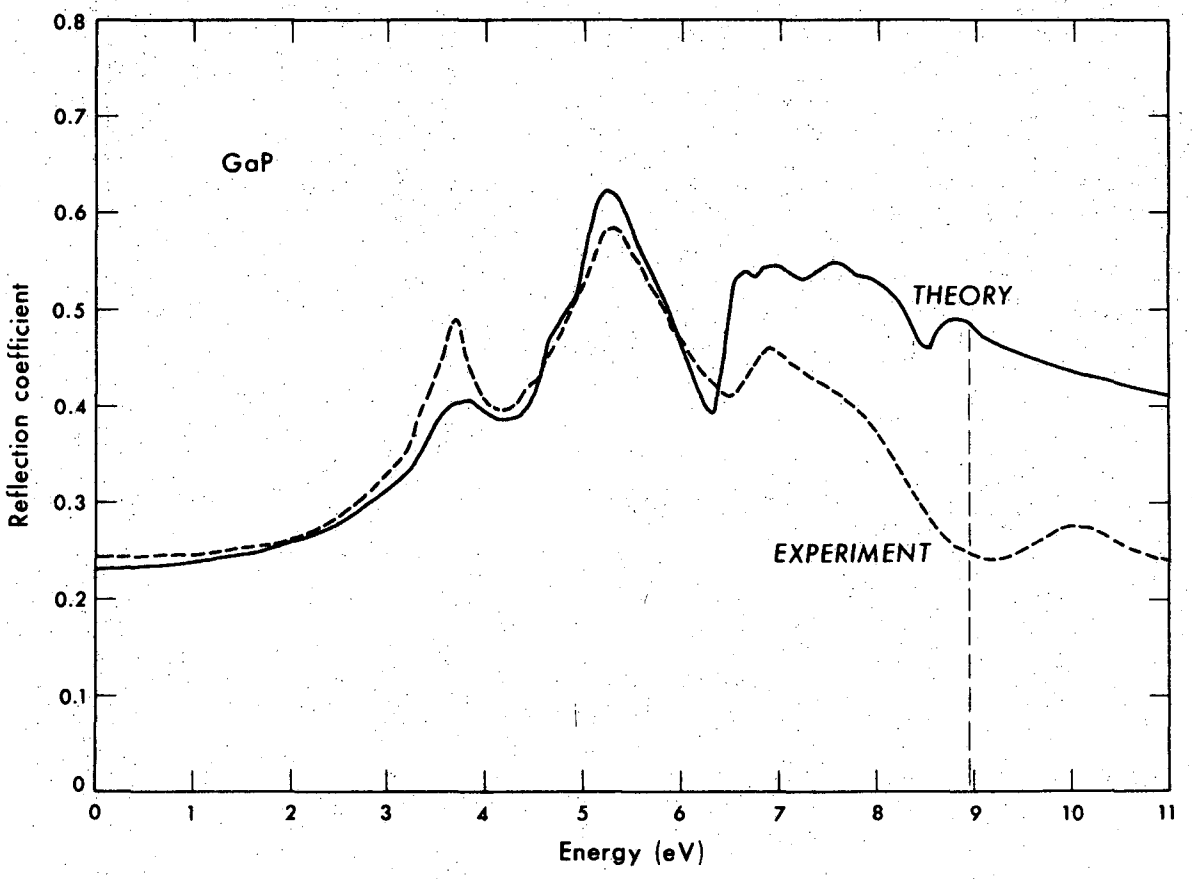

XBL 7011-6978

Figure 8

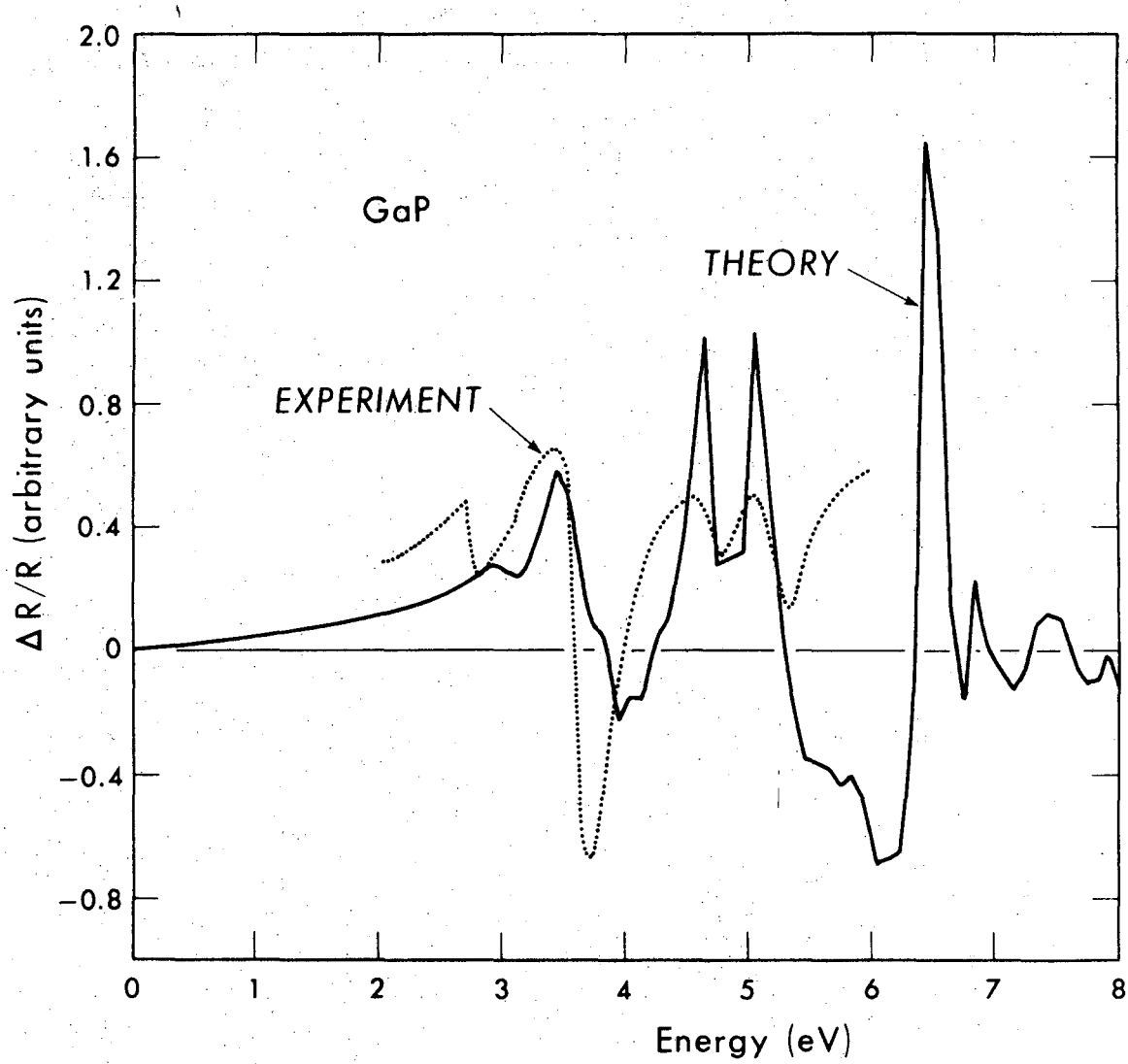

XBL 7011-6993

Figure 9

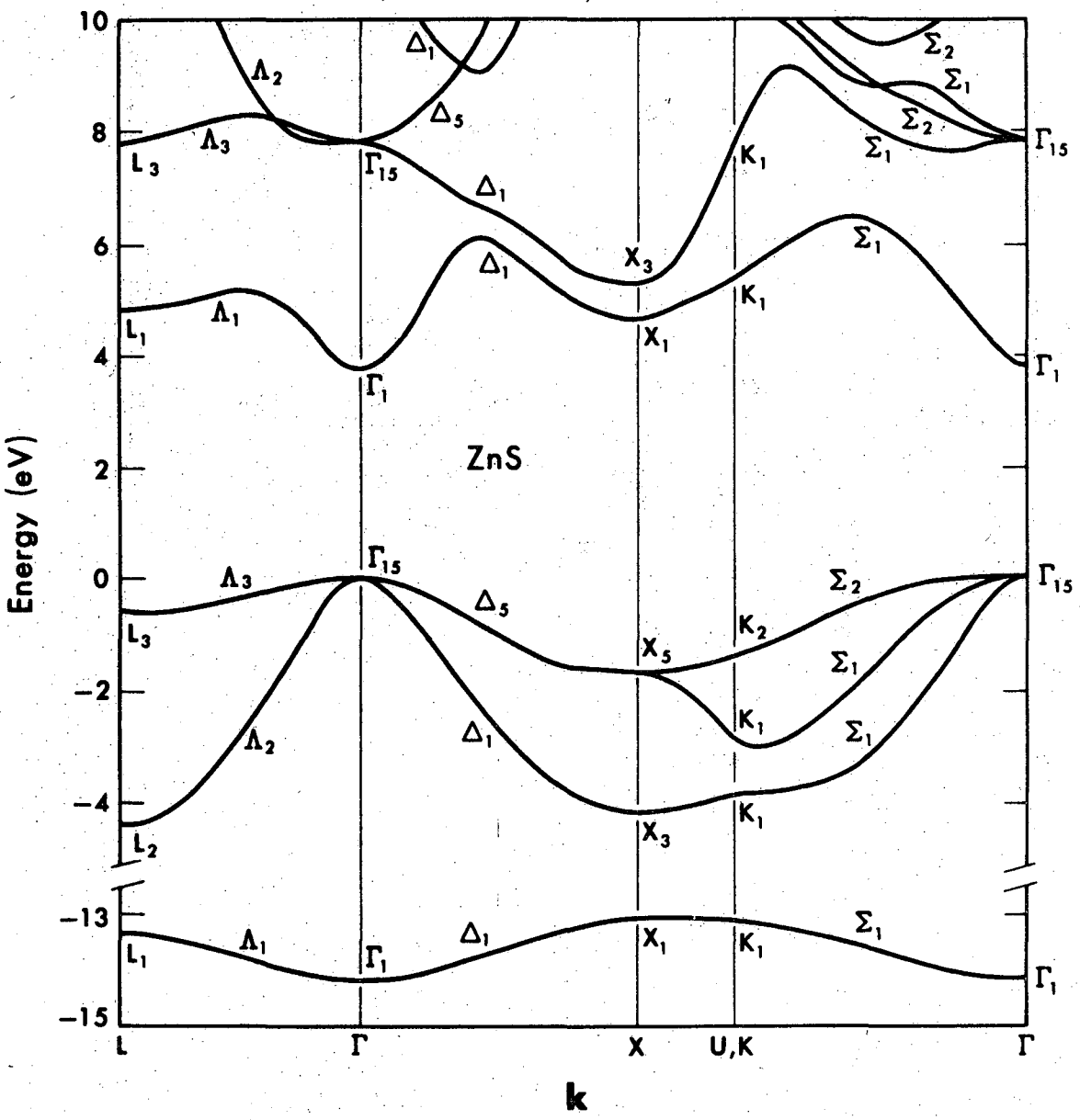

XBL 7011-6981

Figure 10

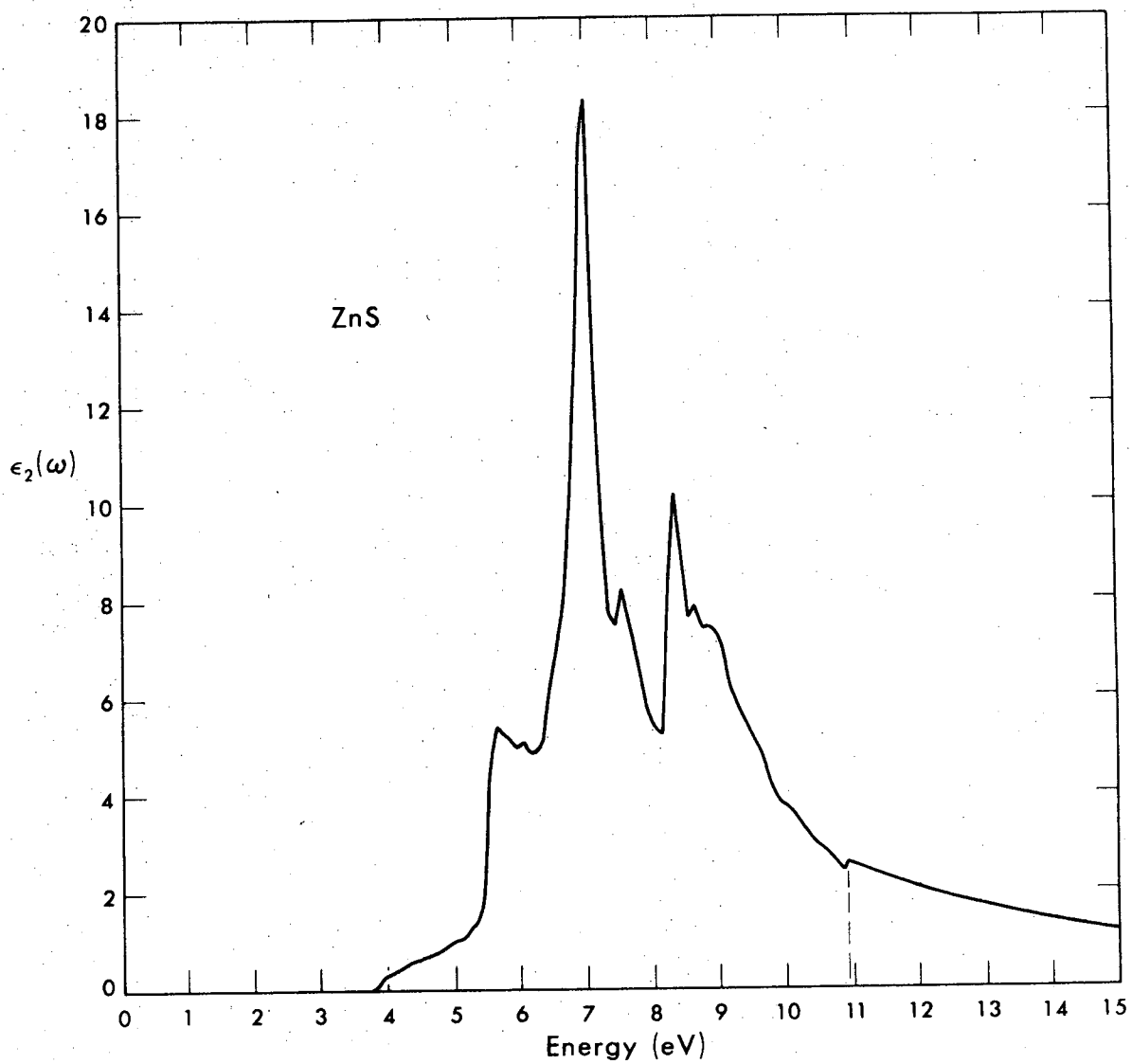

XBL 7011-6995

Figure 11

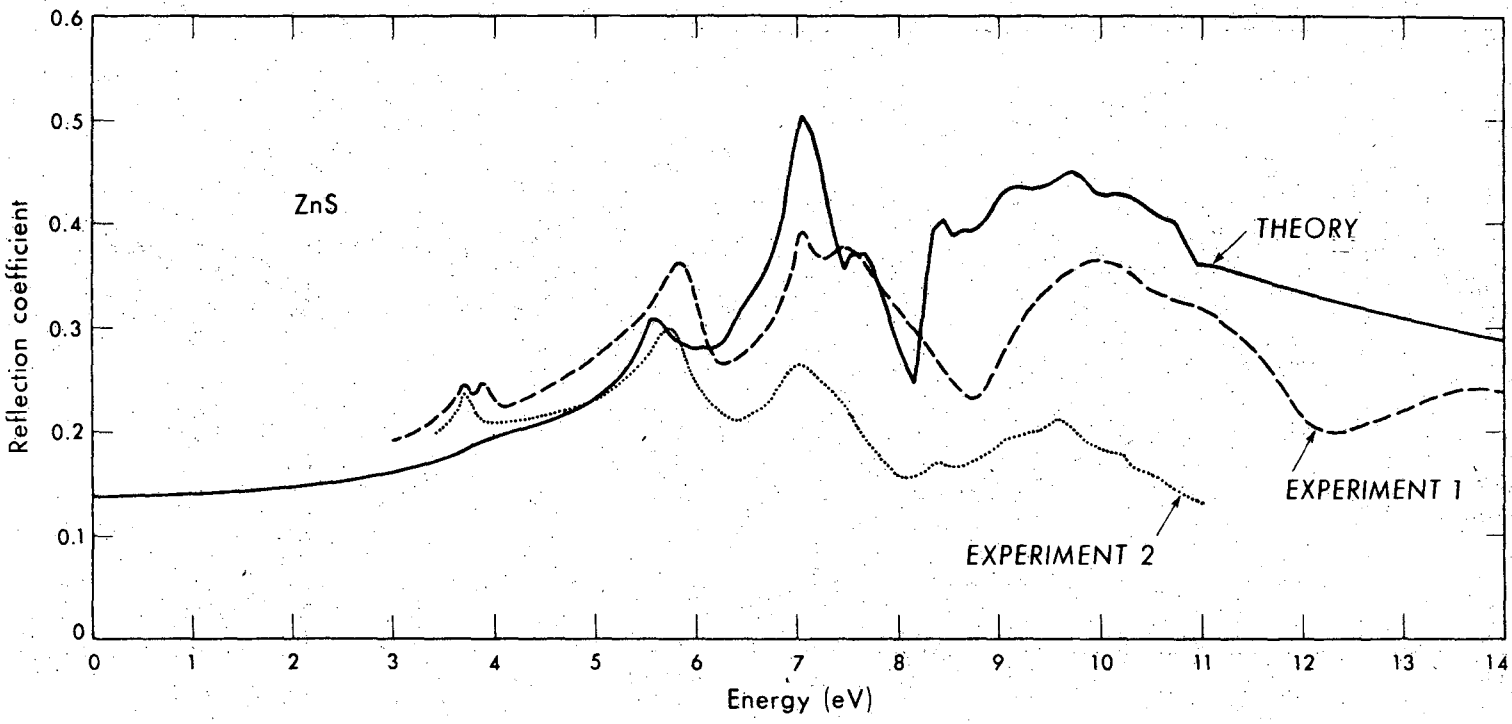

XBL 7011-6994

Figure 12

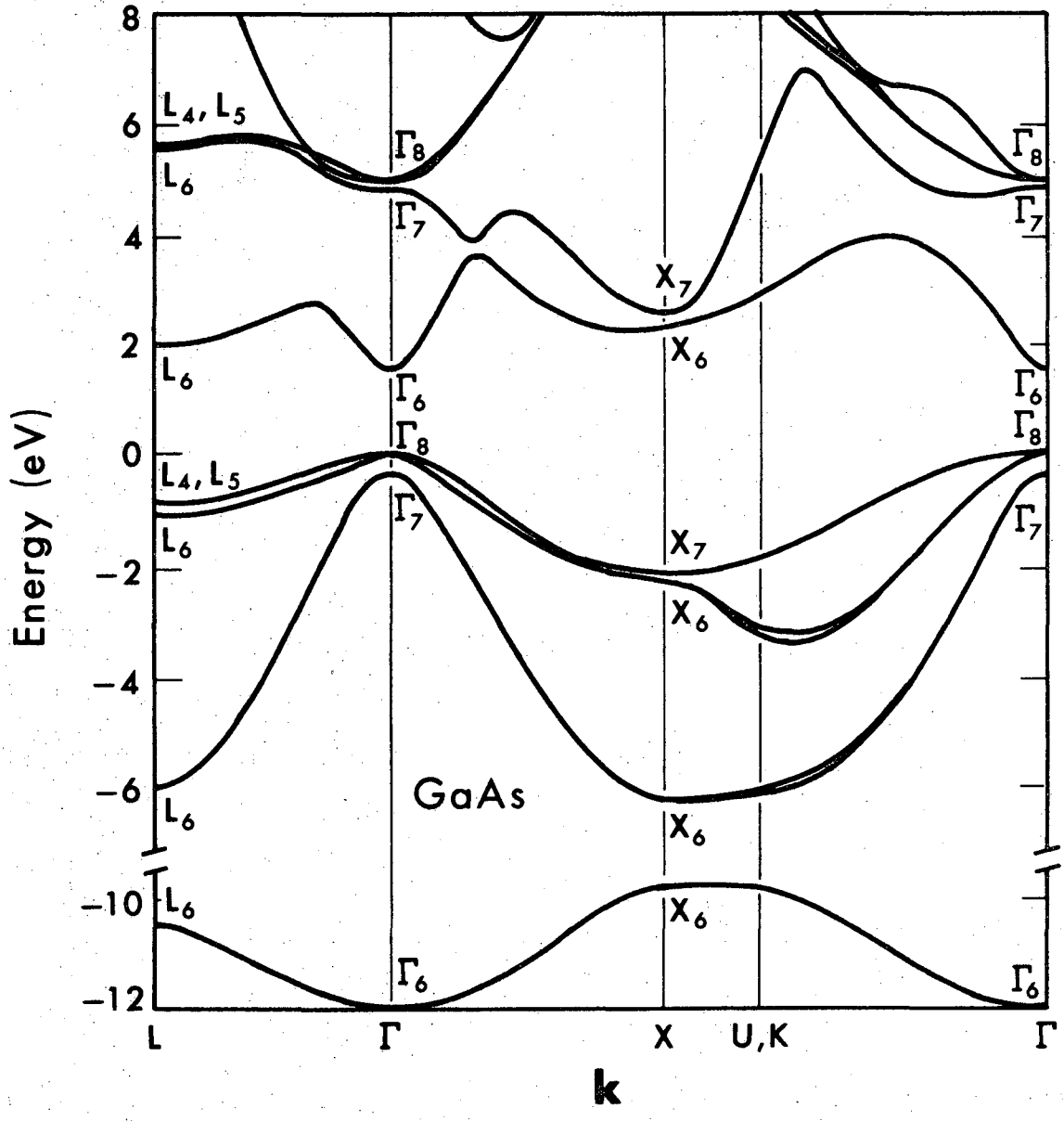

XBL 7011-6975

Figure 13

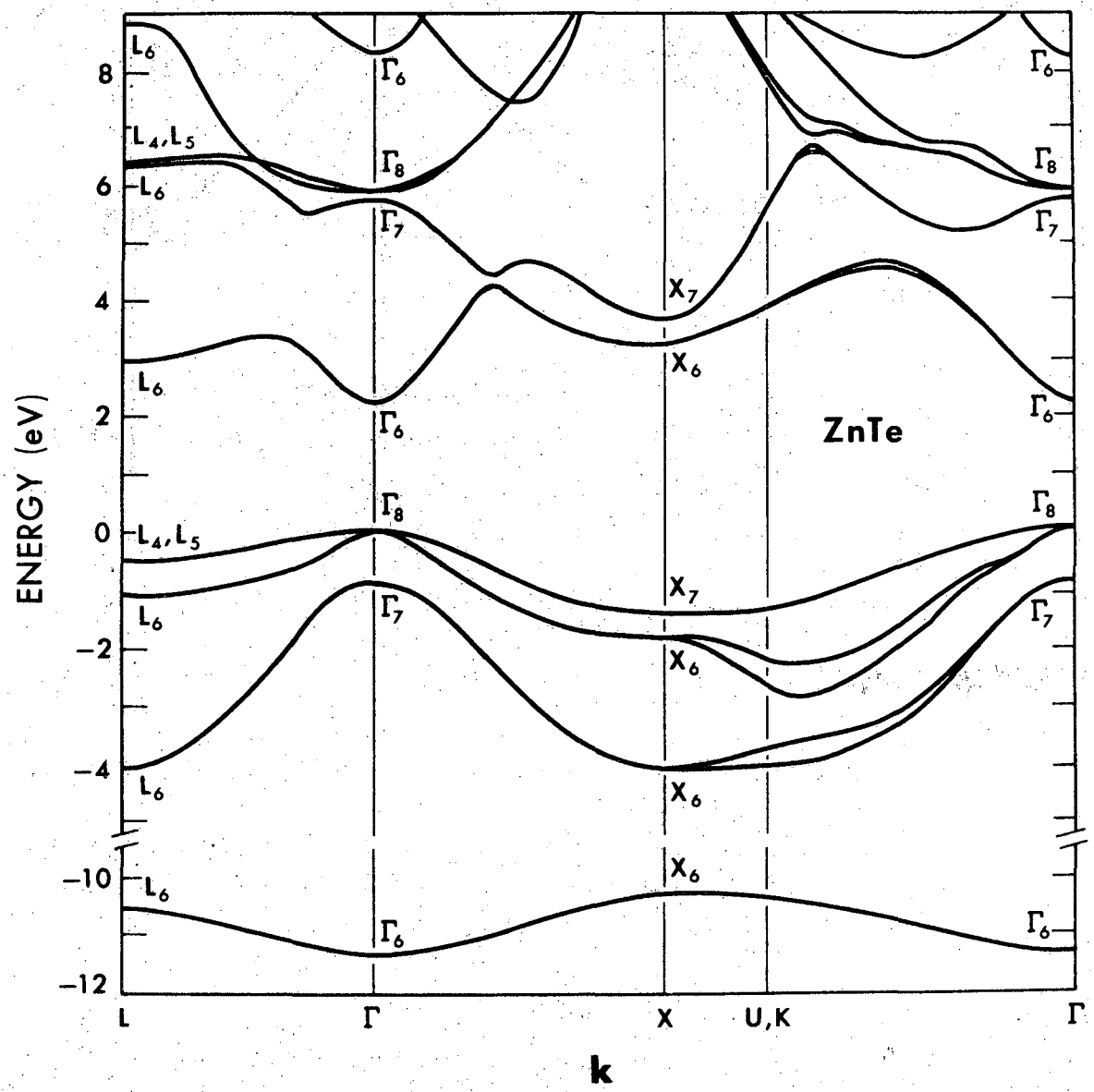

XBL 7011-6996

Figure 14

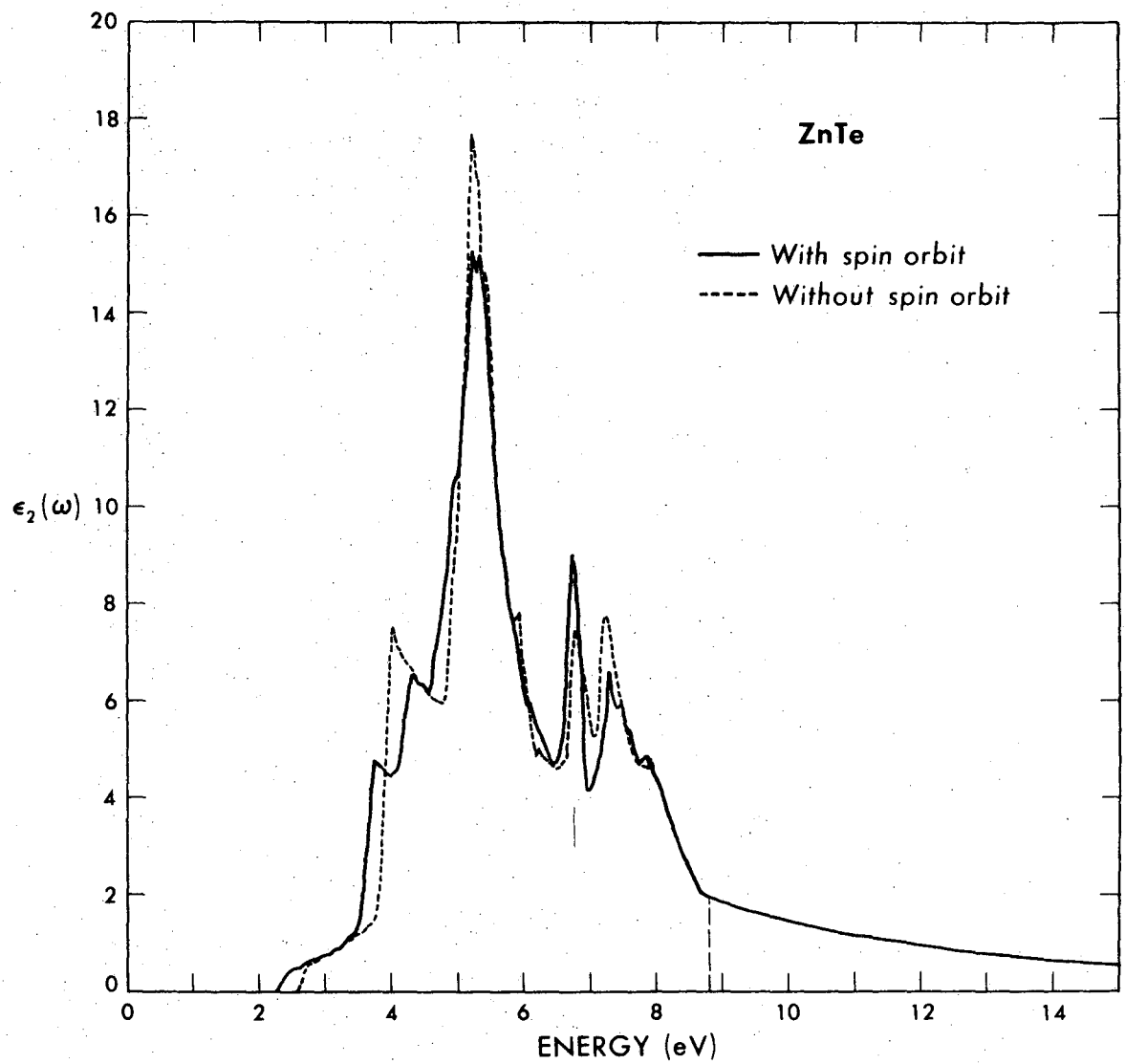

XBL 7011-6997

Figure 15

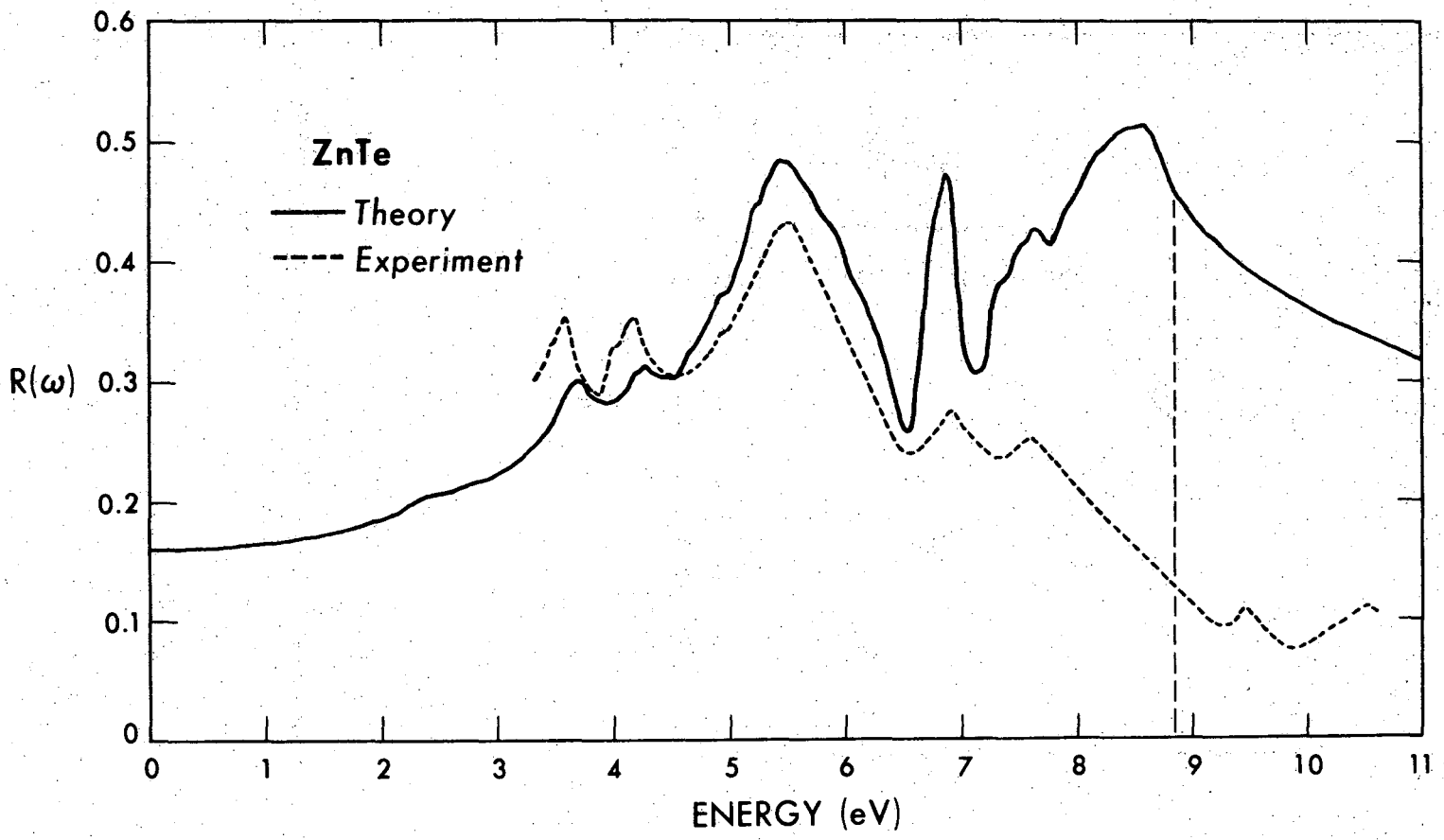

XBL 7011-6998

Figure 16

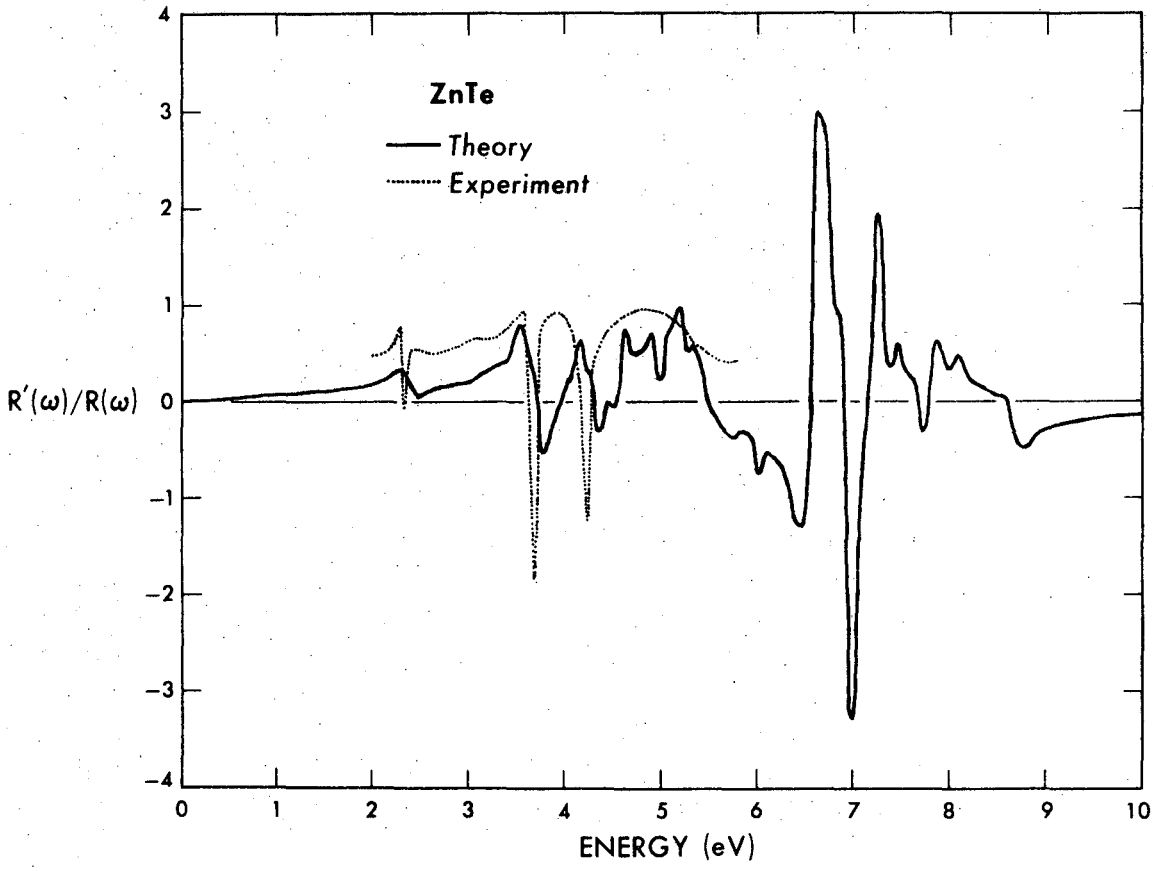

XBL 7011-6999

Figure 17

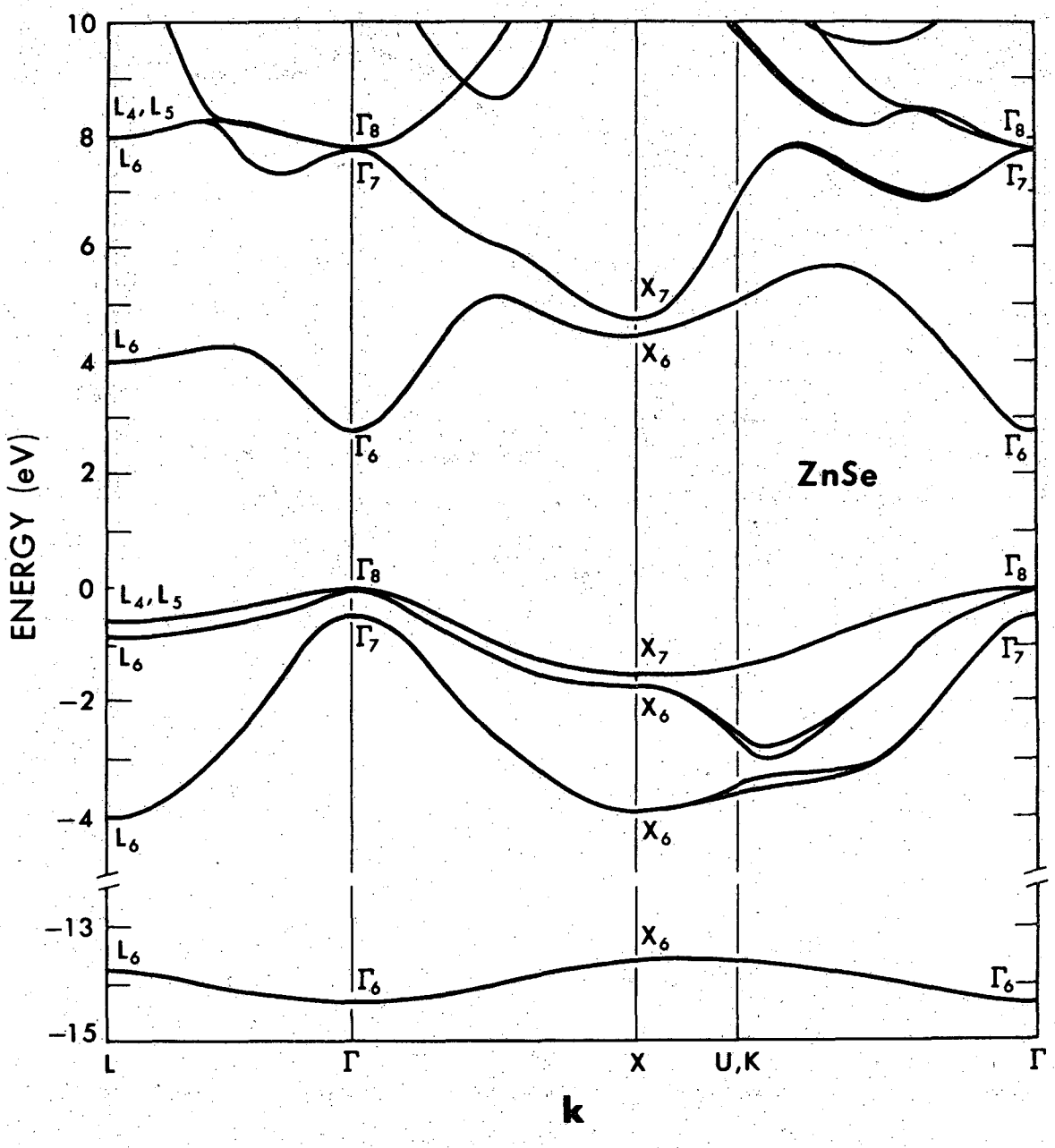

XBL 7011-7000

Figure 18

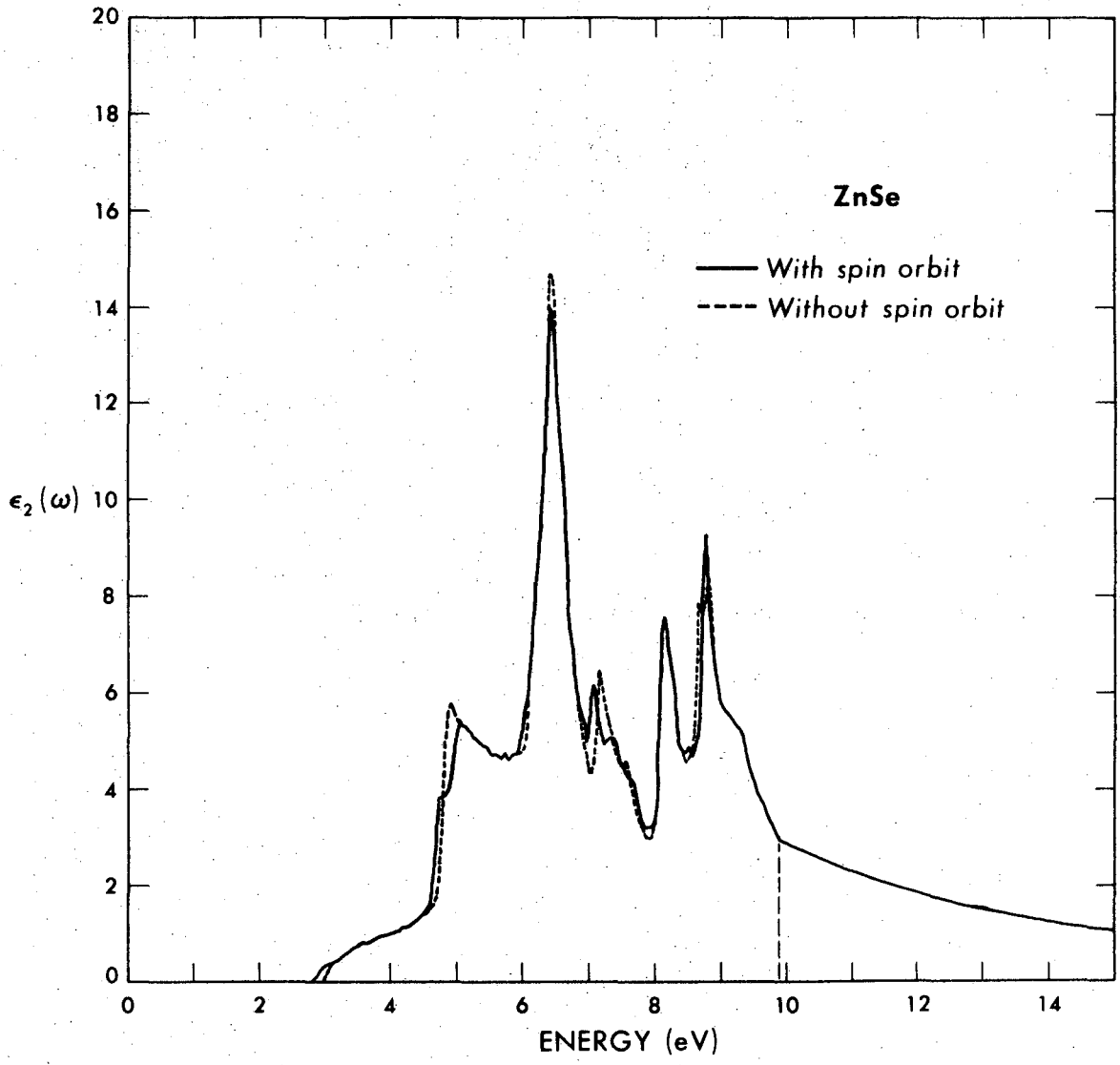

XBL 7011-7001

Figure 19

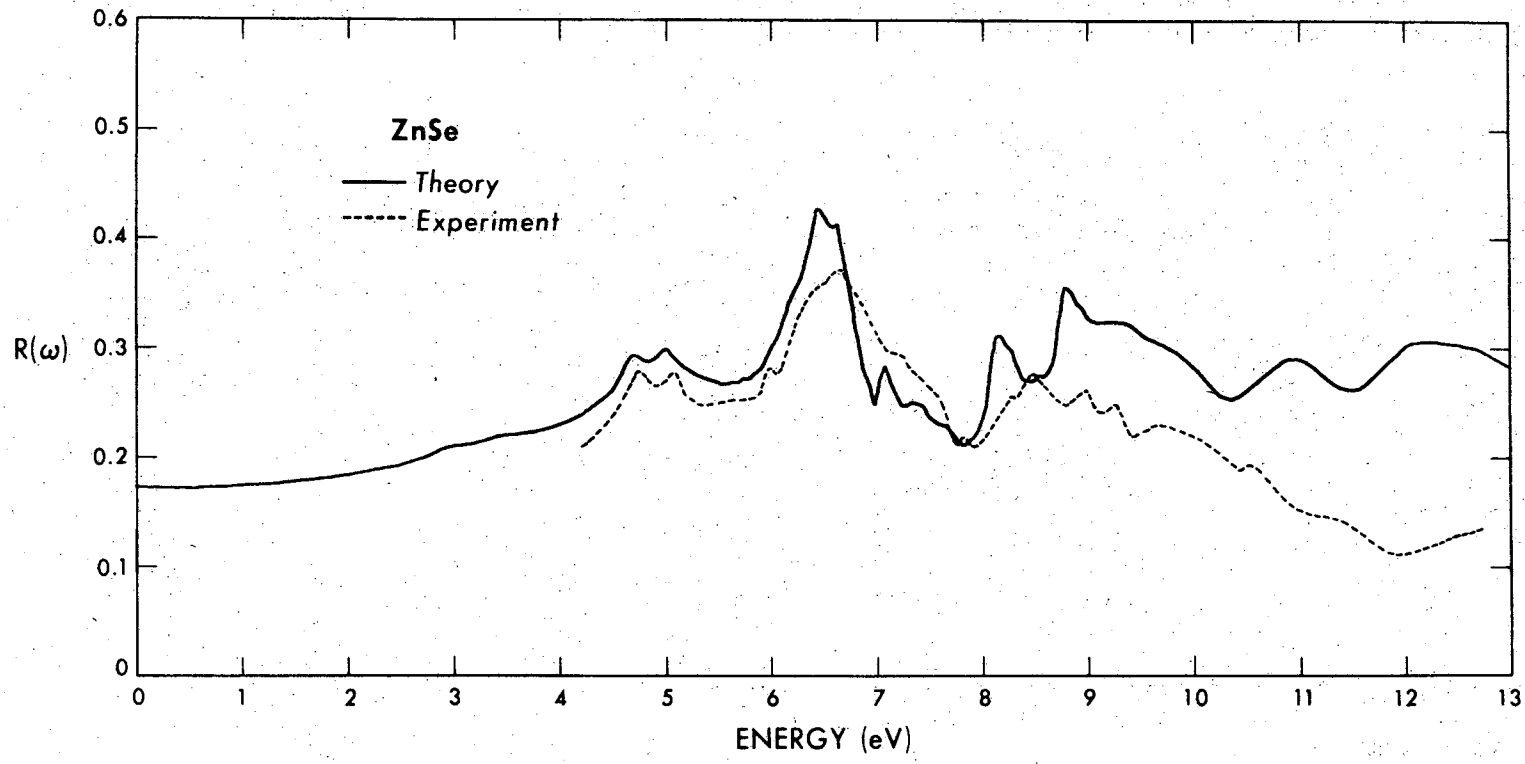

XBL 7011-7006

Figure 20

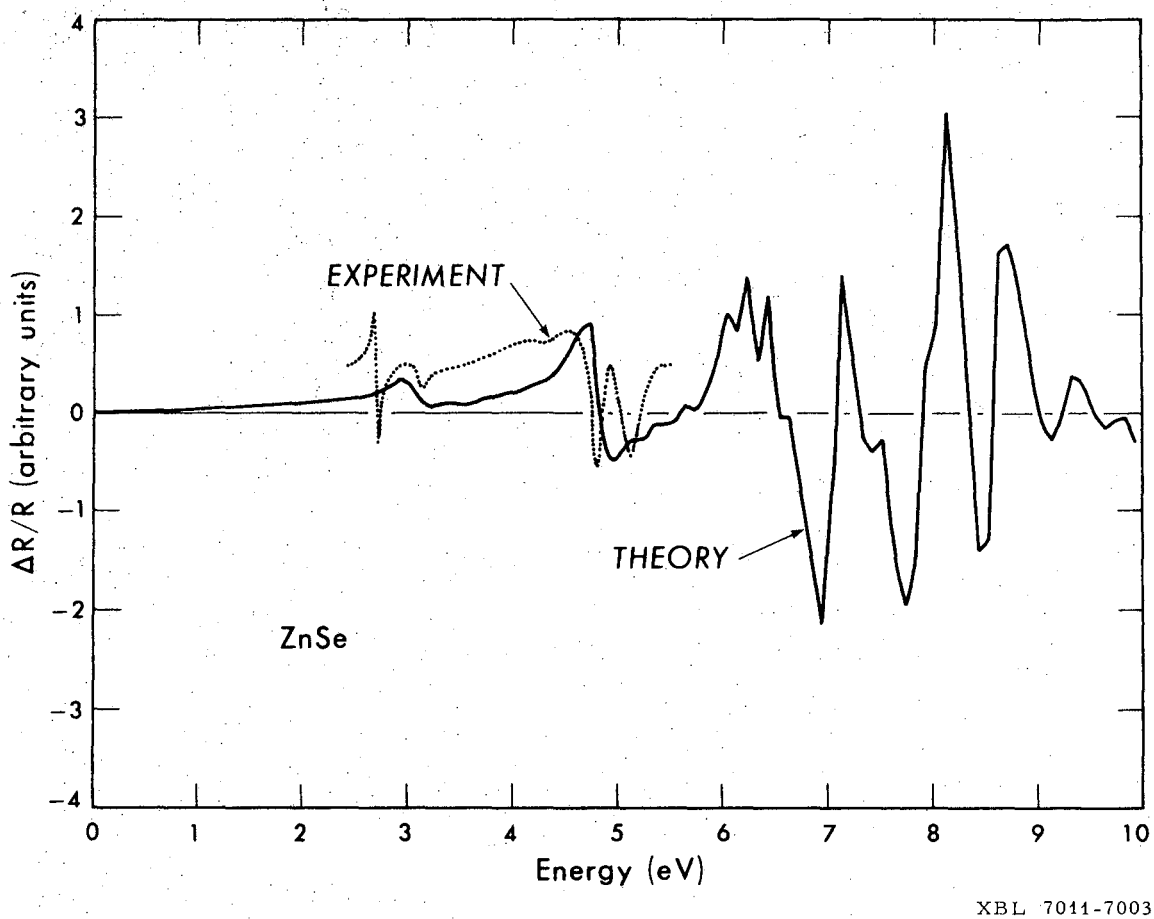

XBL 7011-7003

Figure 21

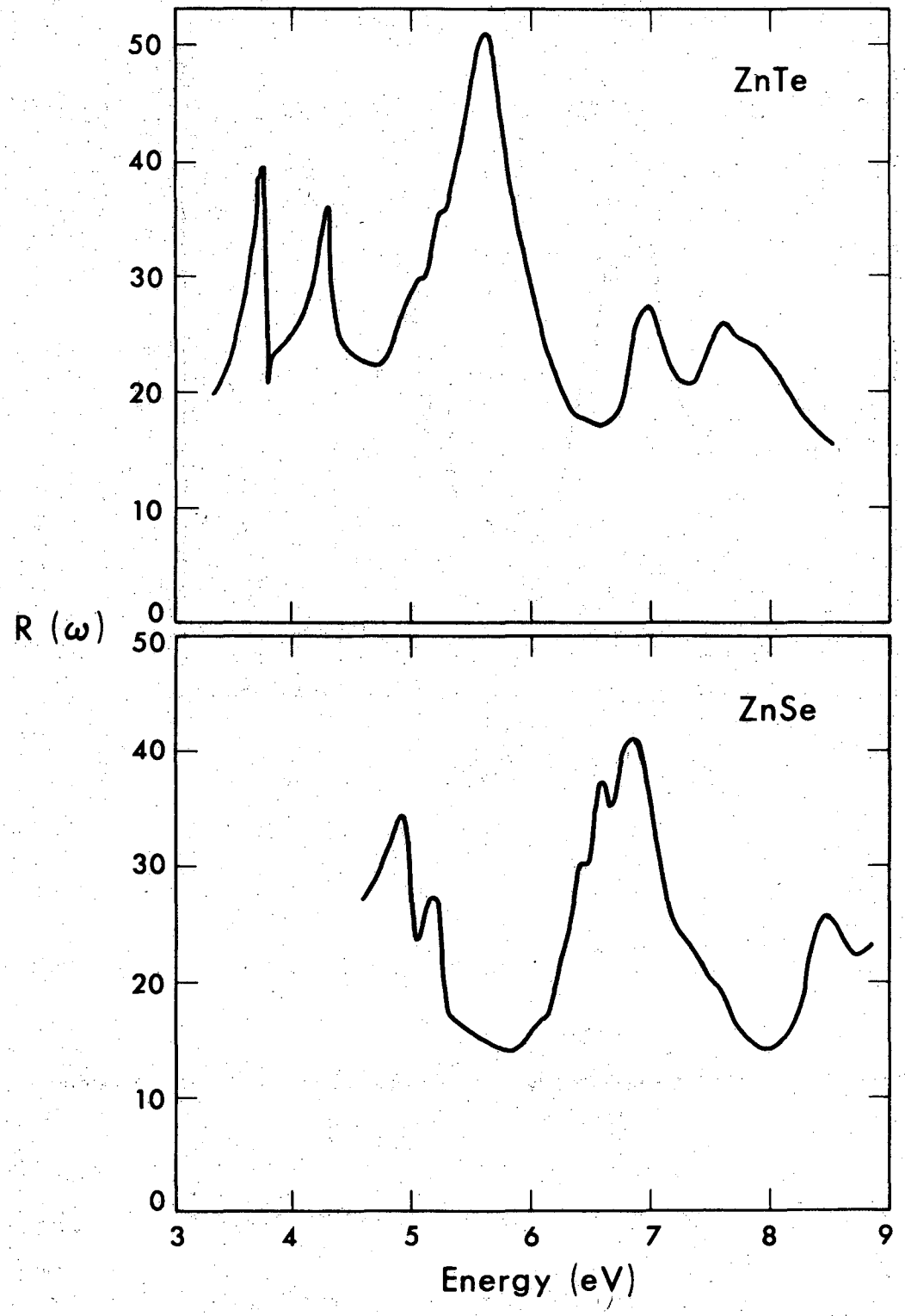

XBL 7011-7004

Figure 22

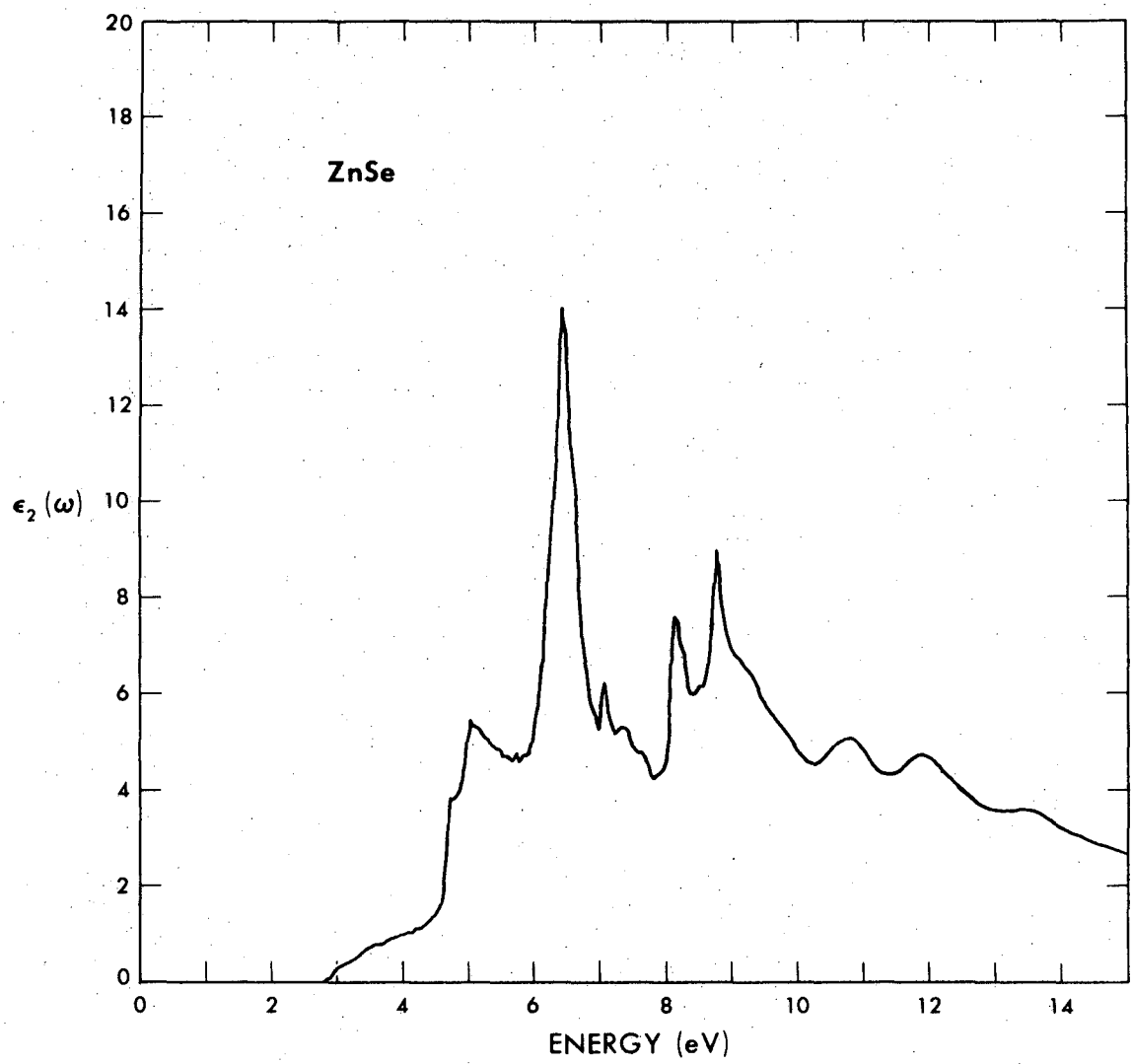

XBL 7011-7005

Figure 23

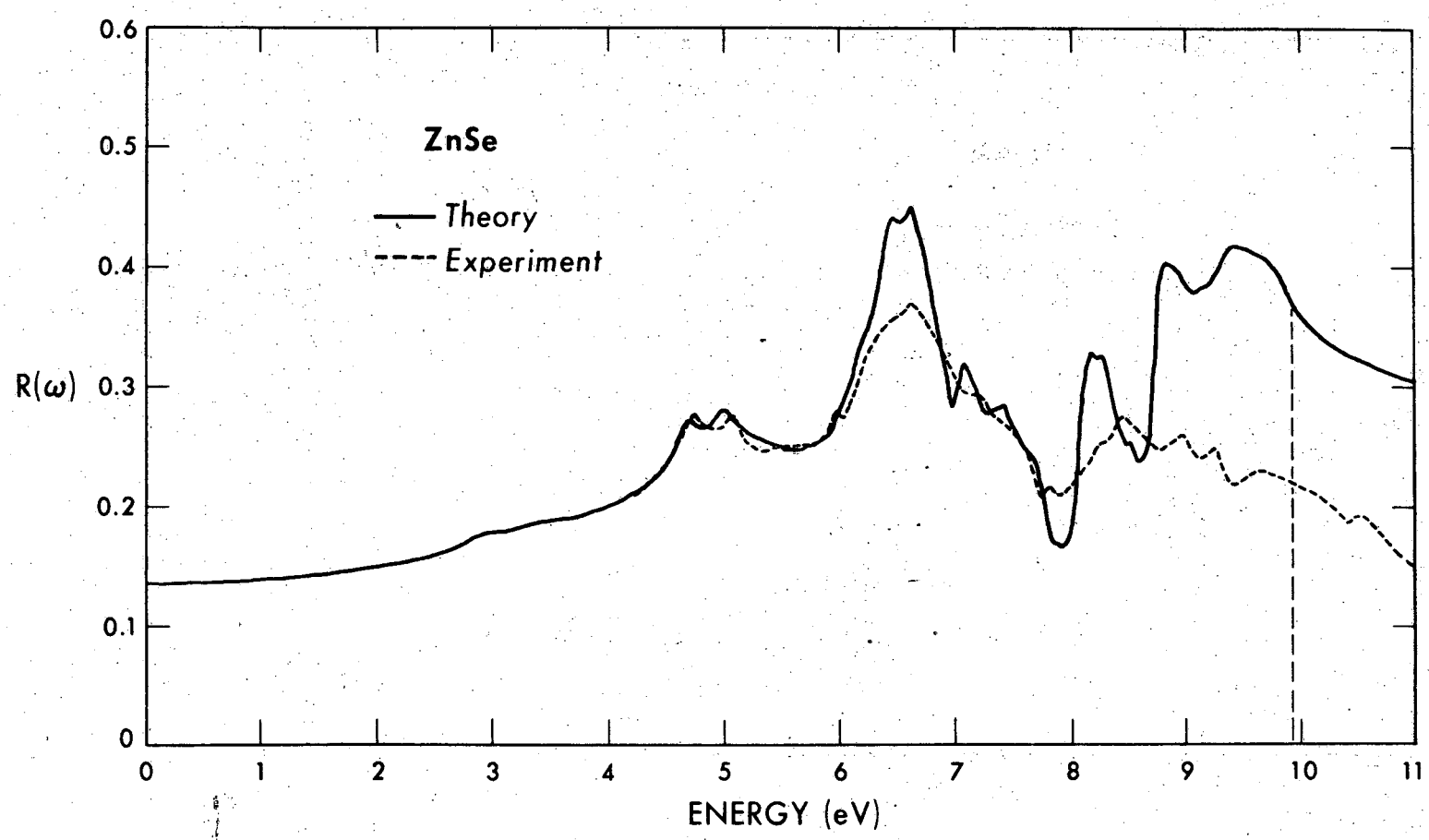

XBL 7011-7002

FIgure 24

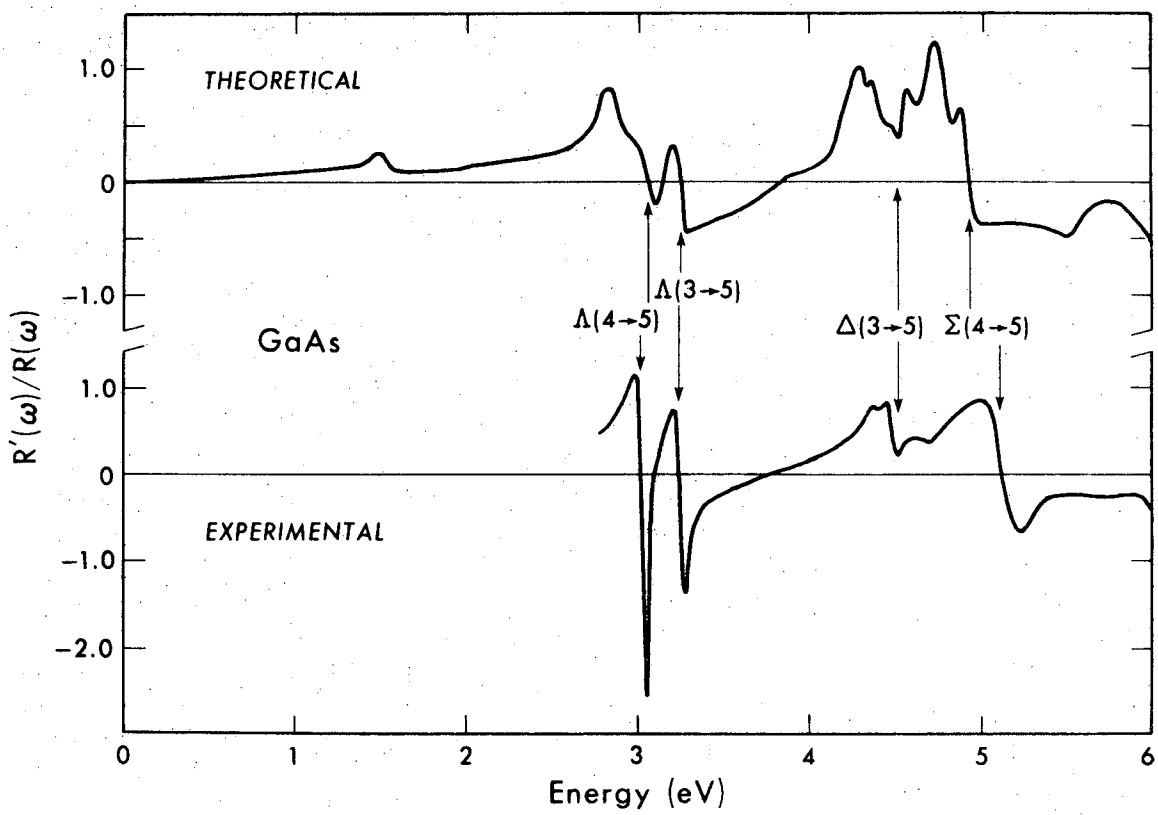
THEORETICAL
EXPERIMENTAL
GaAs
Λ(4→5)
Λ(3→5)
Δ(3→5)
Σ(4→5)
R'(ω)/R(ω)
Energy (eV)
1.0
0
-1.0
-2.0
0
1
2
3
4
5
6
XBL 7011-7007

Figure 25

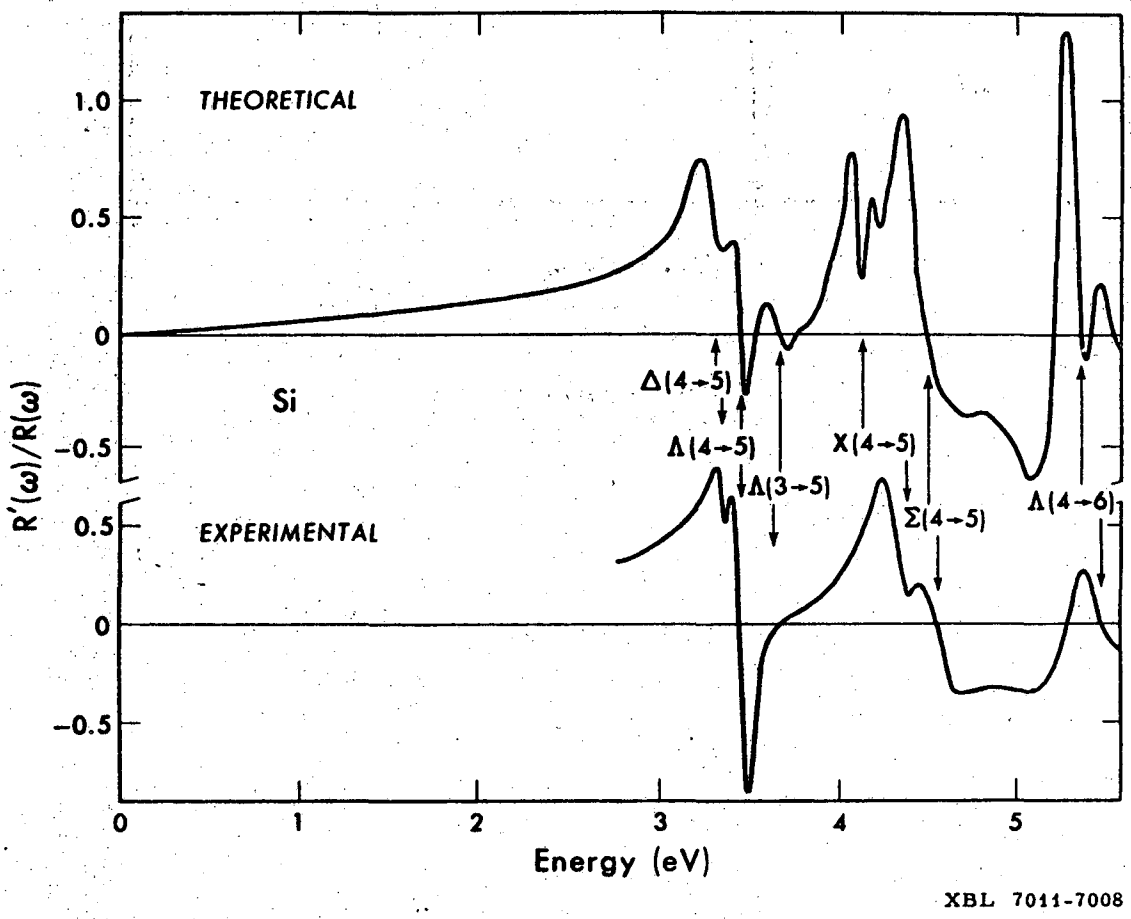
THEORETICAL
EXPERIMENTAL
Si
R'(ω)/R(ω)
Energy (eV)
Δ(4→5)
Λ(4→5)
Λ(3→5)
X(4→5)
Σ(4→5)
Λ(4→6)
1.0
0.5
0
-0.5
0
1
2
3
4
5
XBL 7011-7008

Figure 26

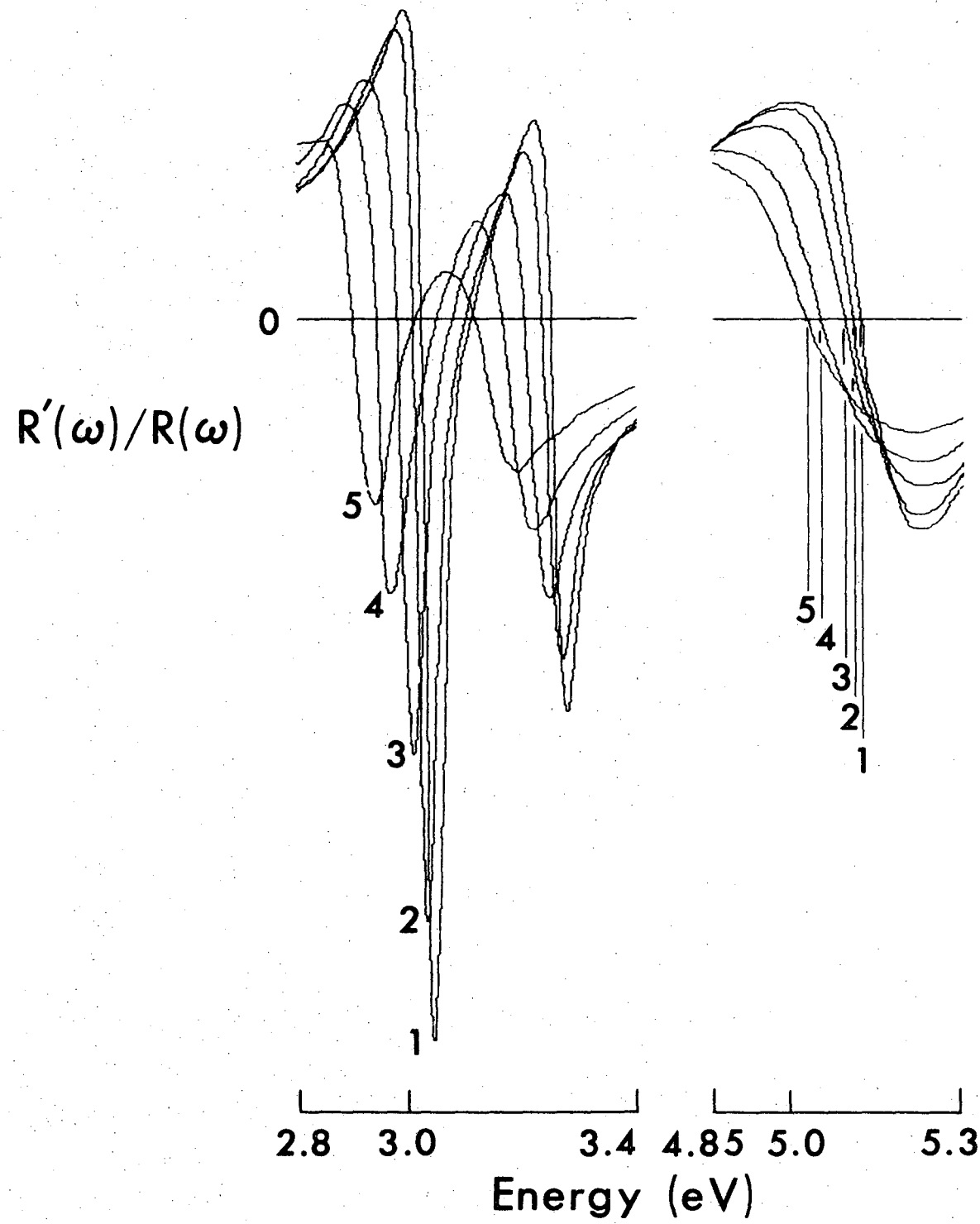

XBL 7011-7009

Figure 27

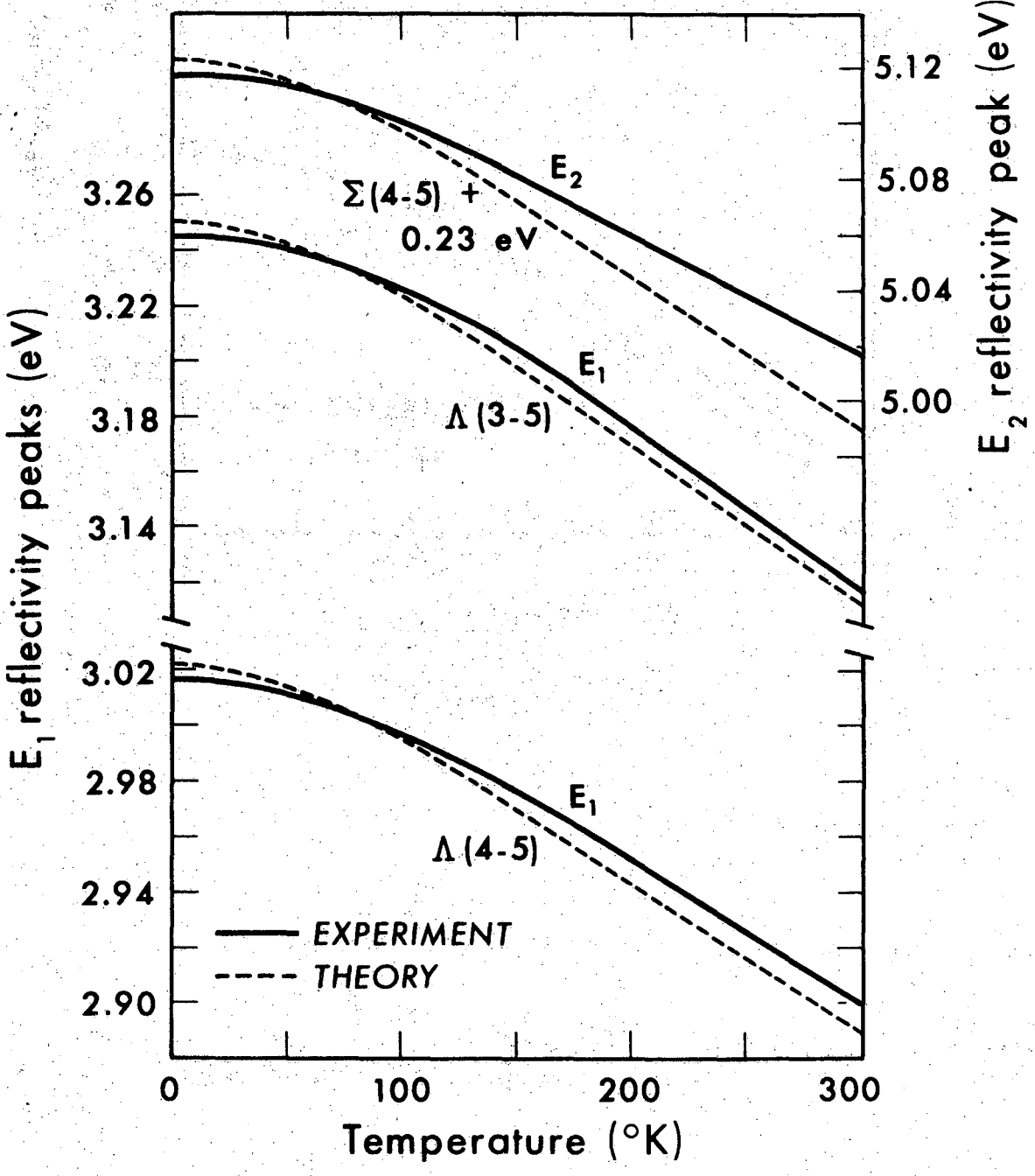

XBL 7011-7010

Figure 28

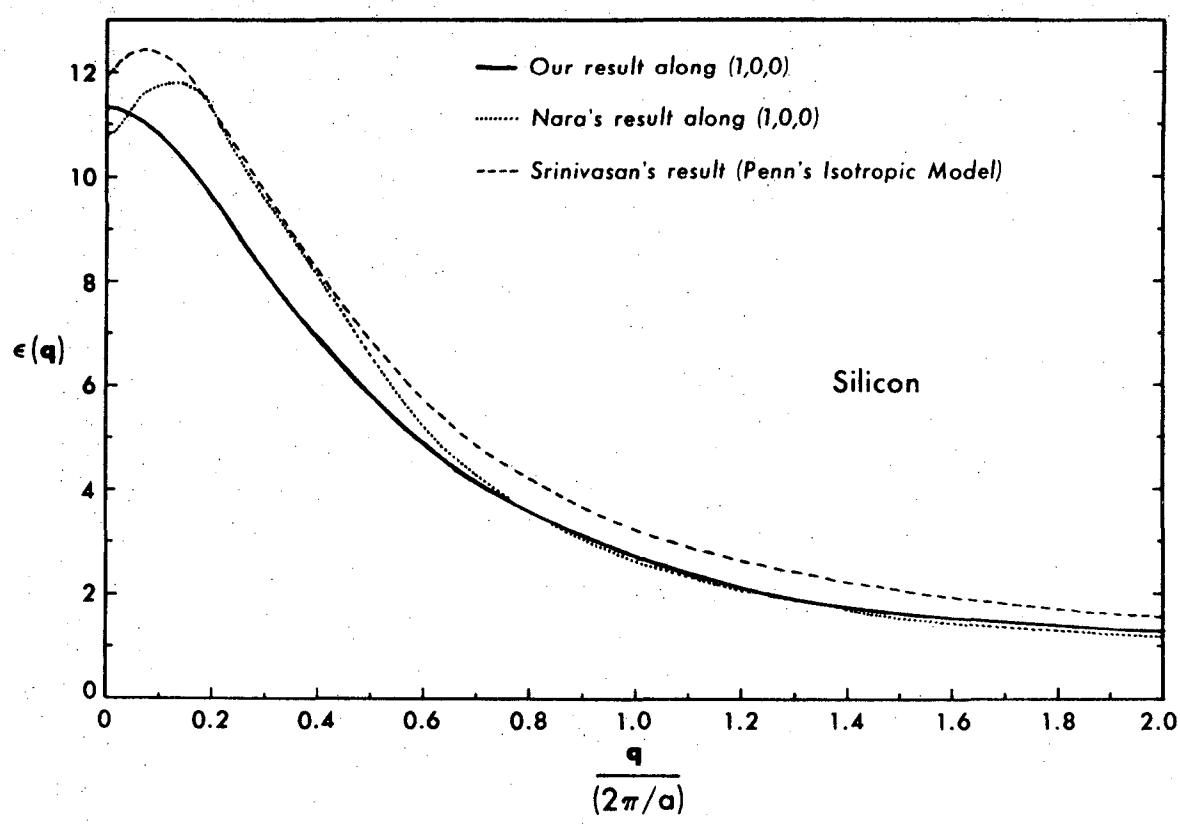

XBL 7011-6980

Figure 29

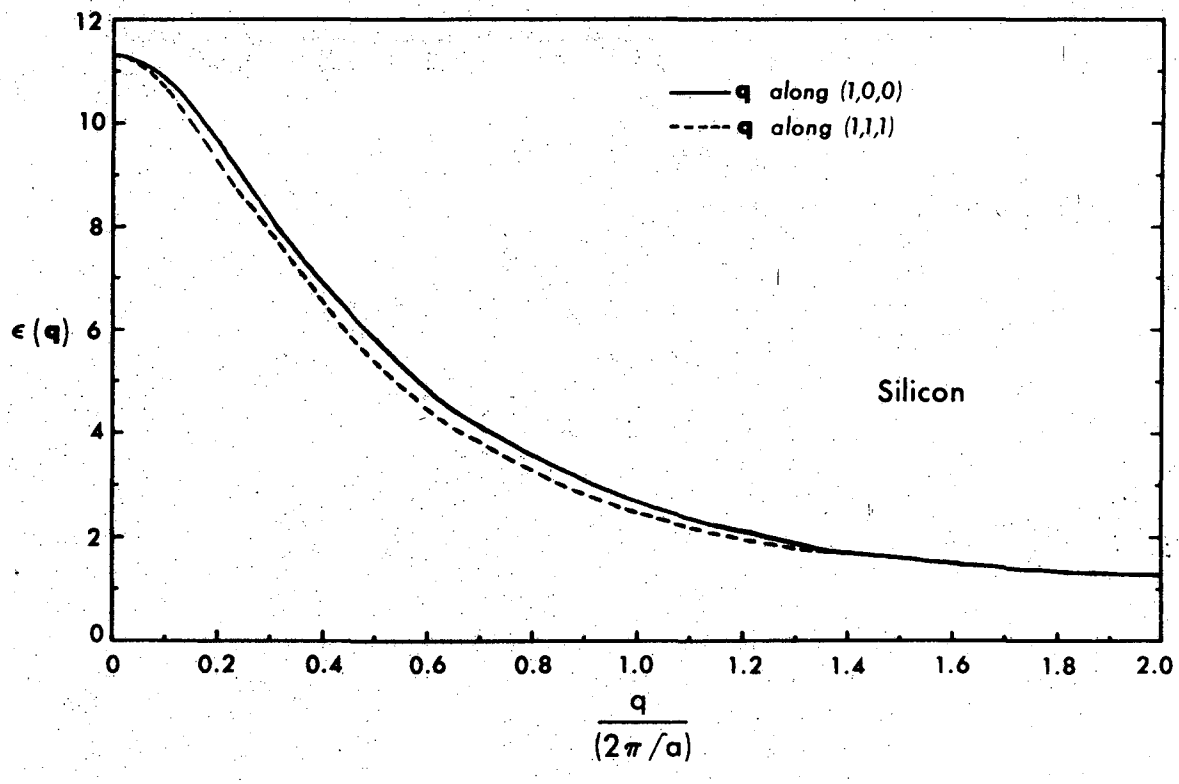

XBL 7011-6973

Figure 30

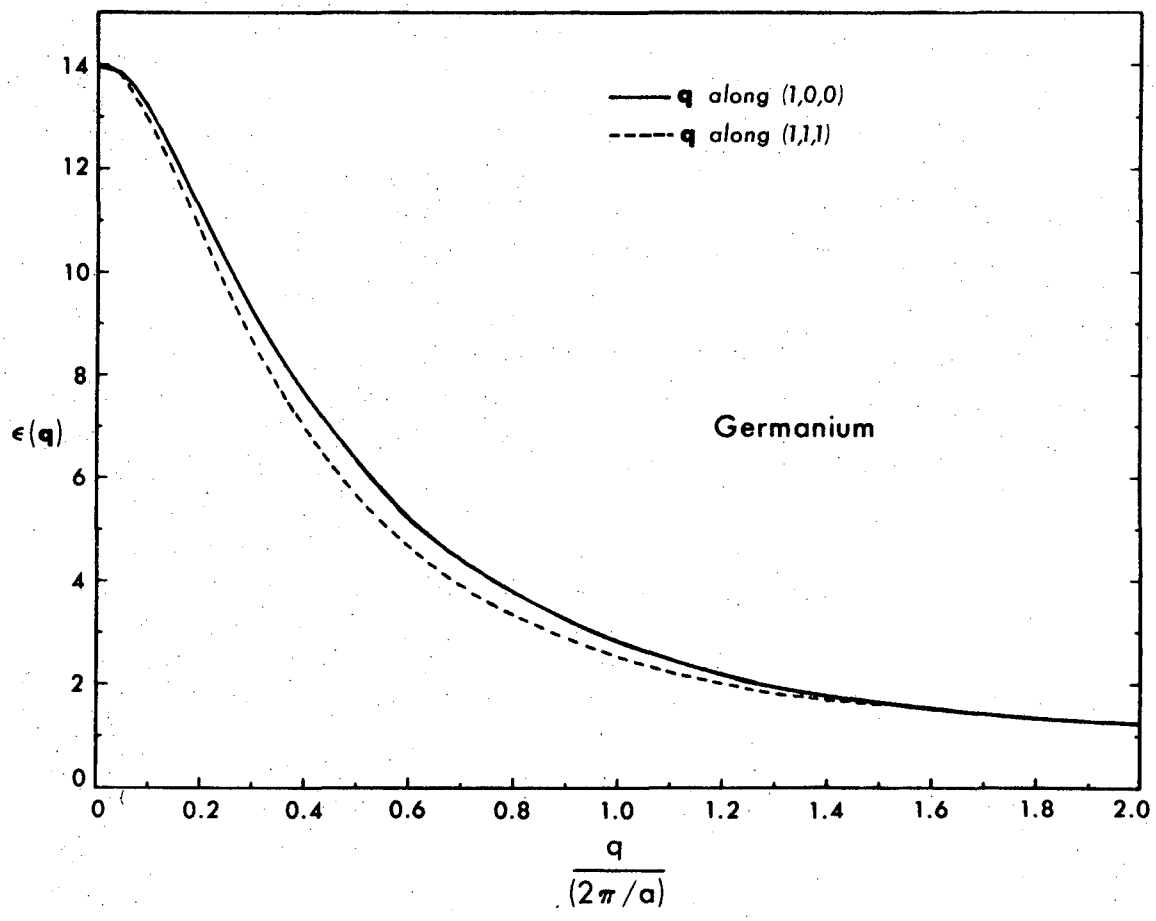

XBL 7011-6979

Figure 31

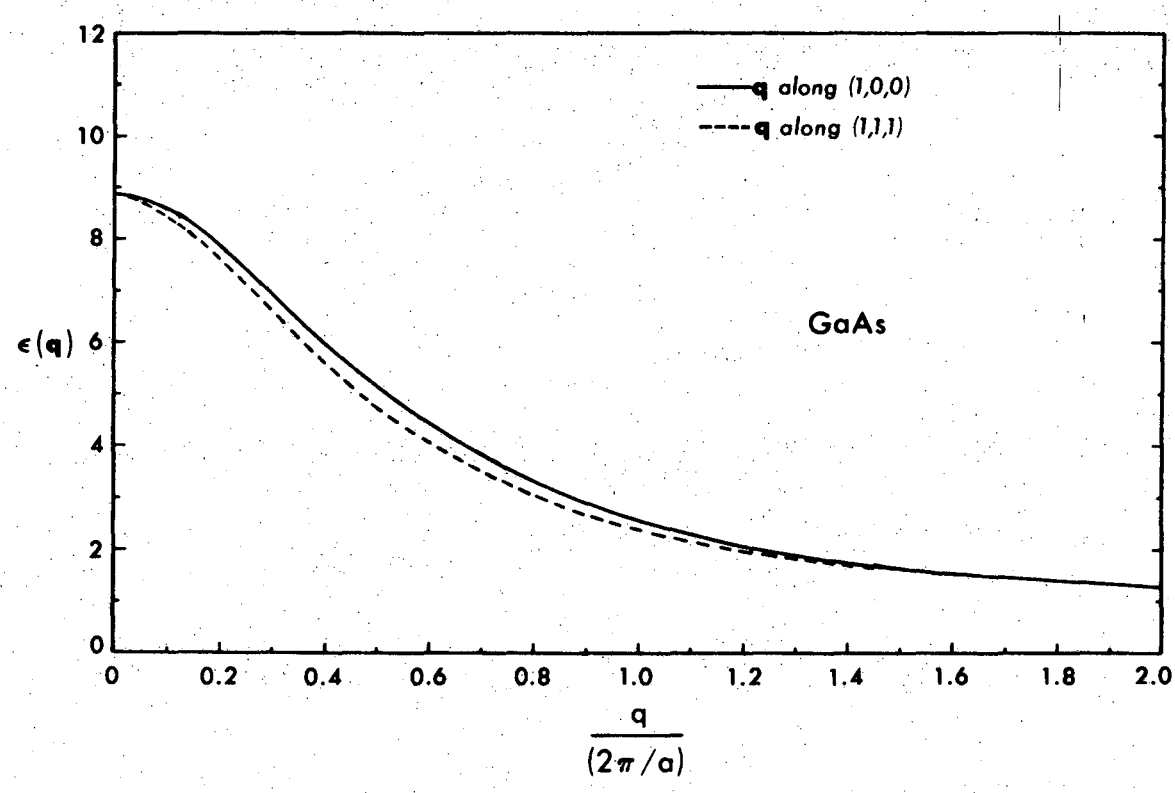

XBL 7011-6971

Figure 32

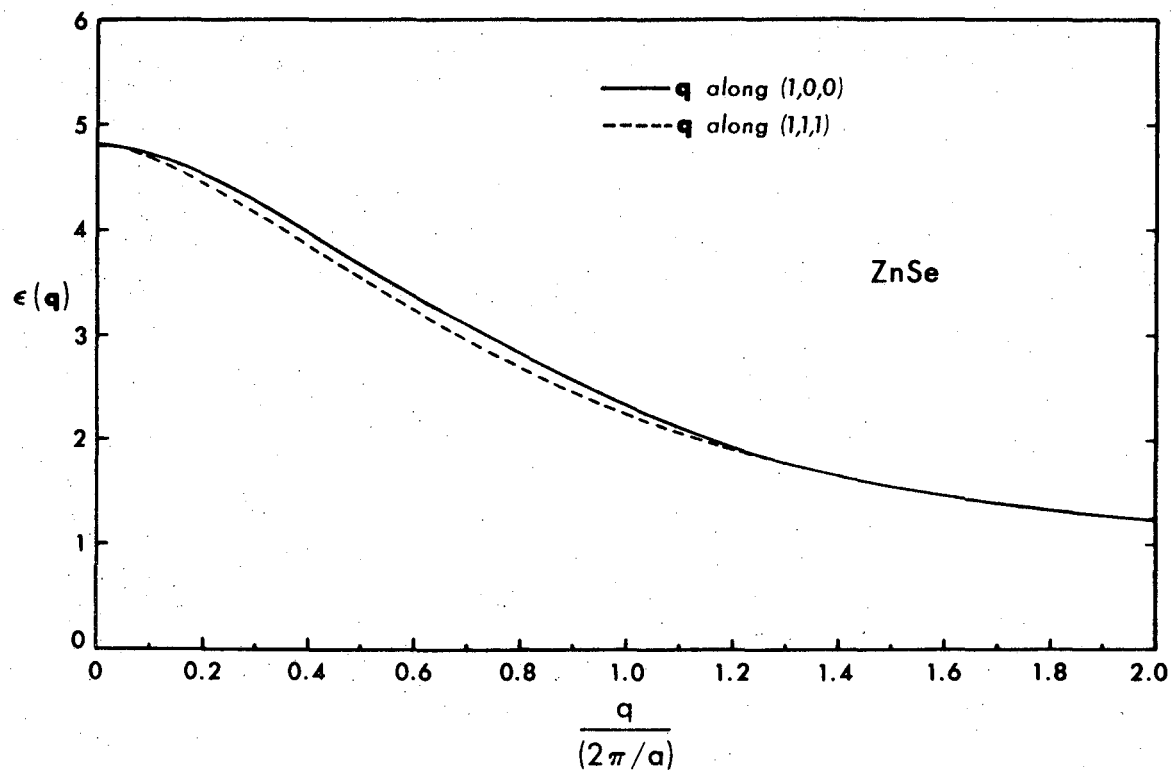

XBL 7011-6972

Figure 33

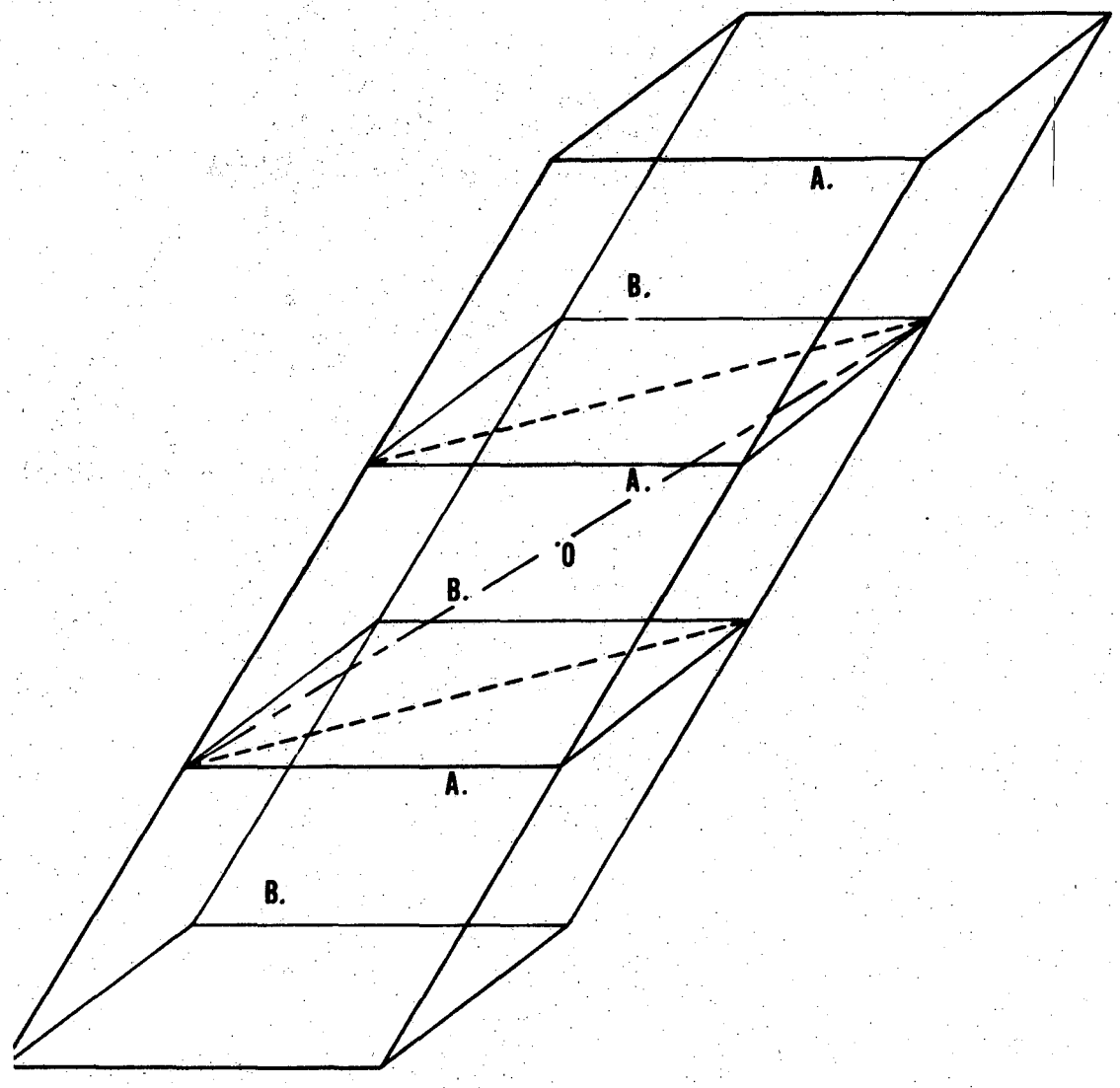

XBL 7011-6983

Figure 34

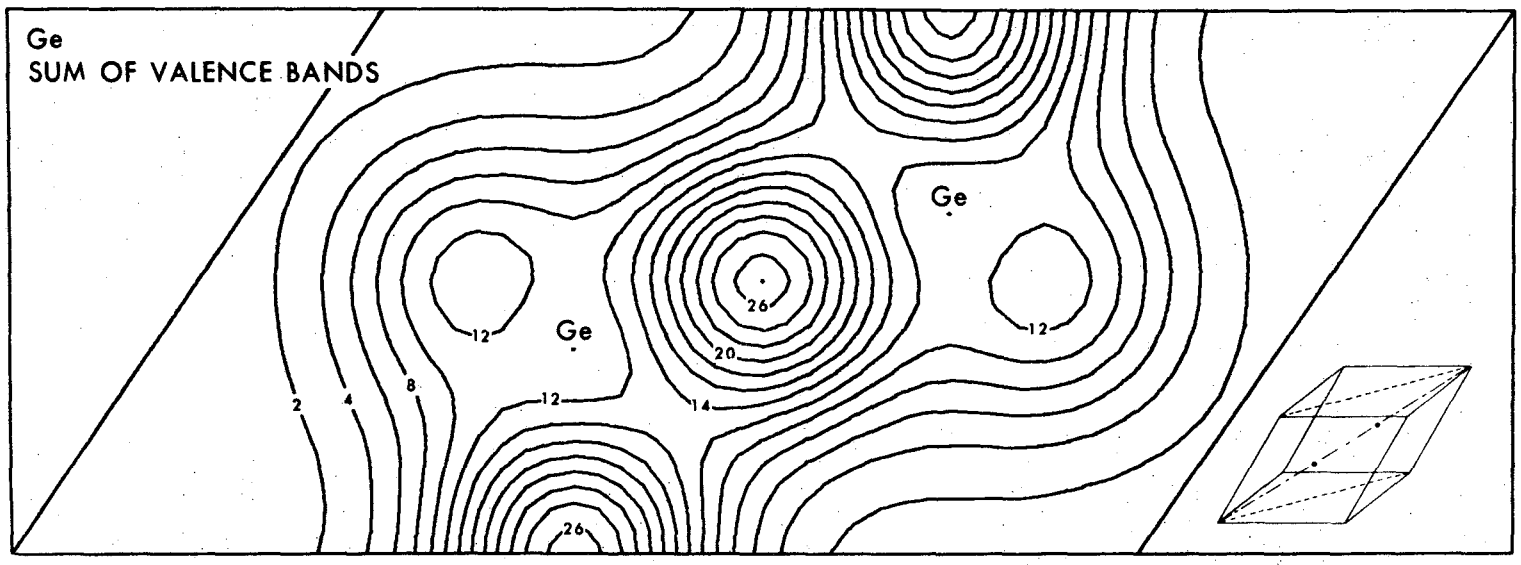

Figure 35

XBL 7011-7011

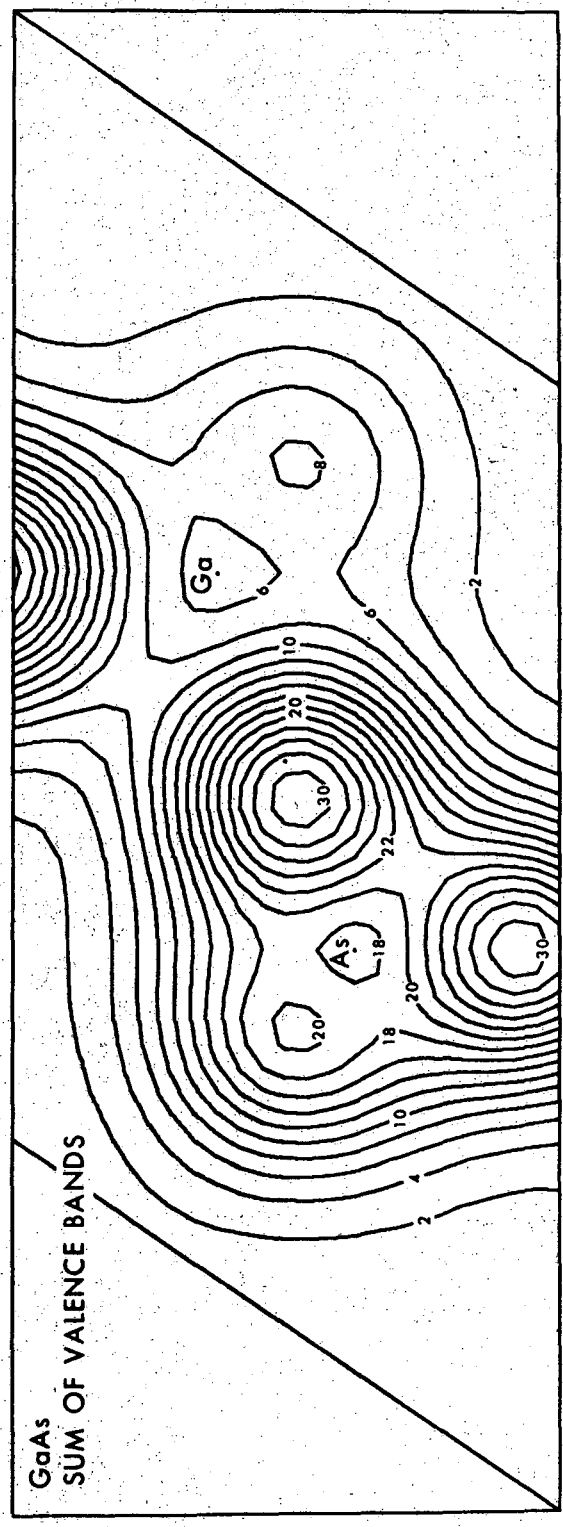

XBL 7011-7012

Figure 36

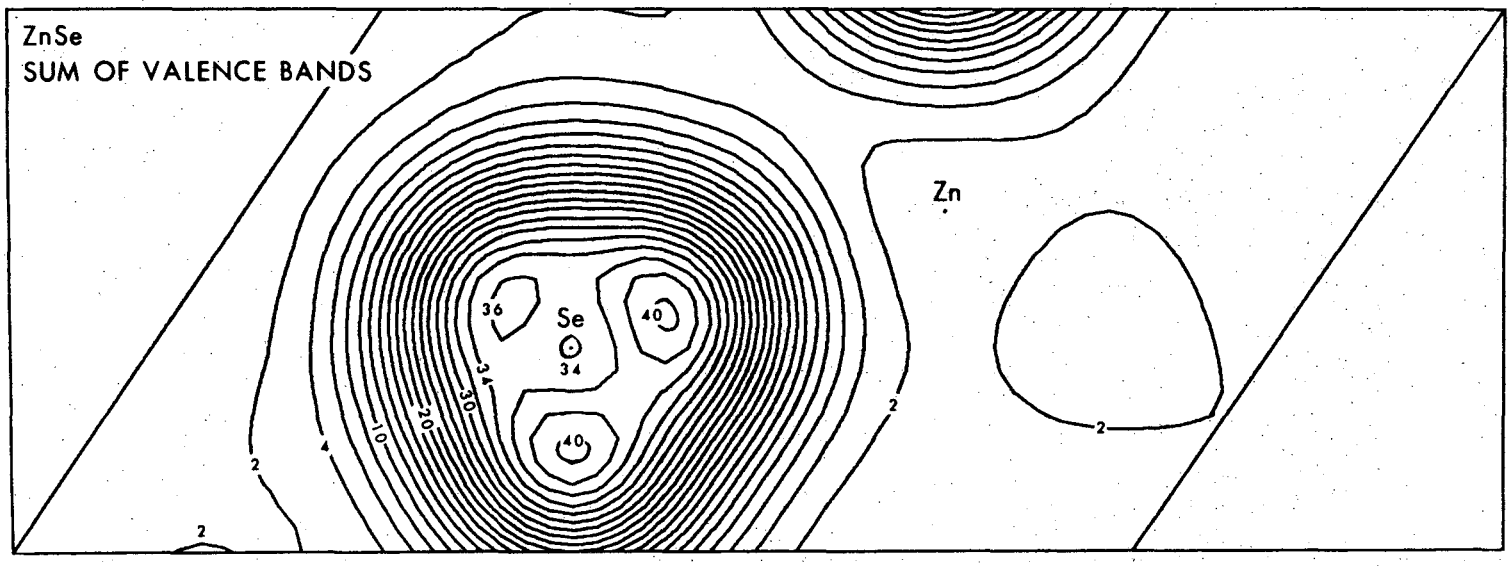

XBL 7011-7013

Figure 37

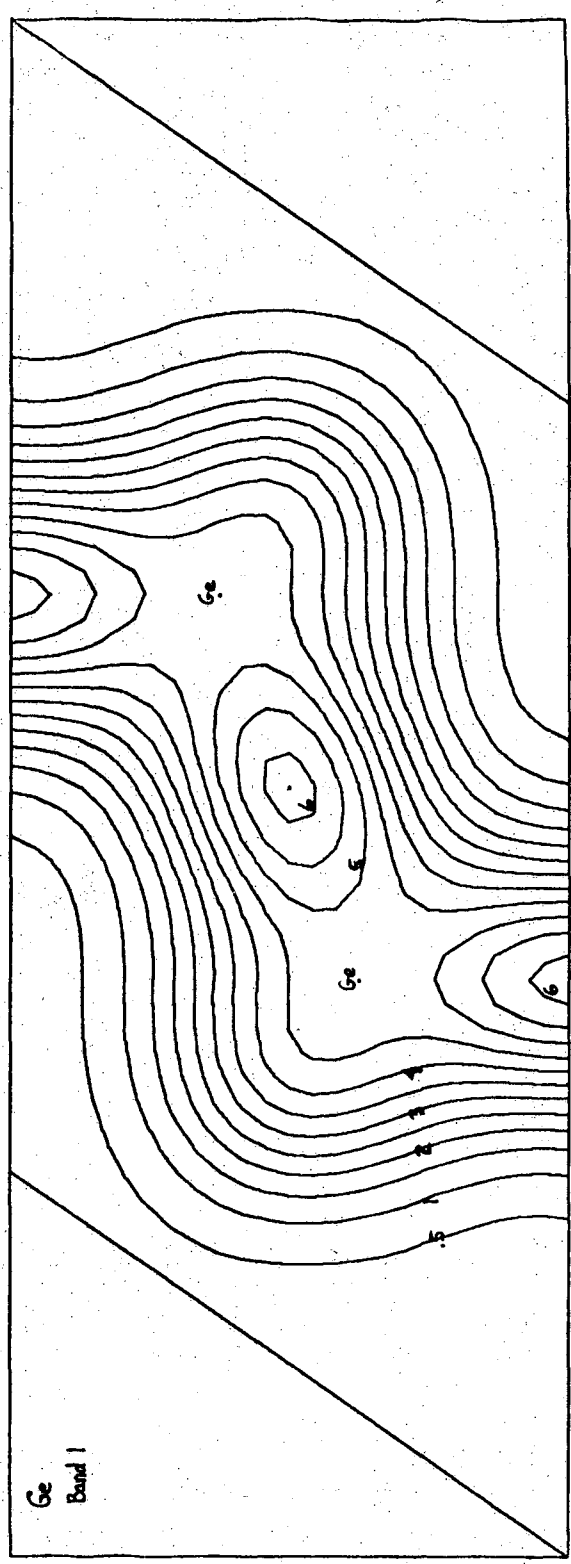

XBL 7011-6984

Figure 38

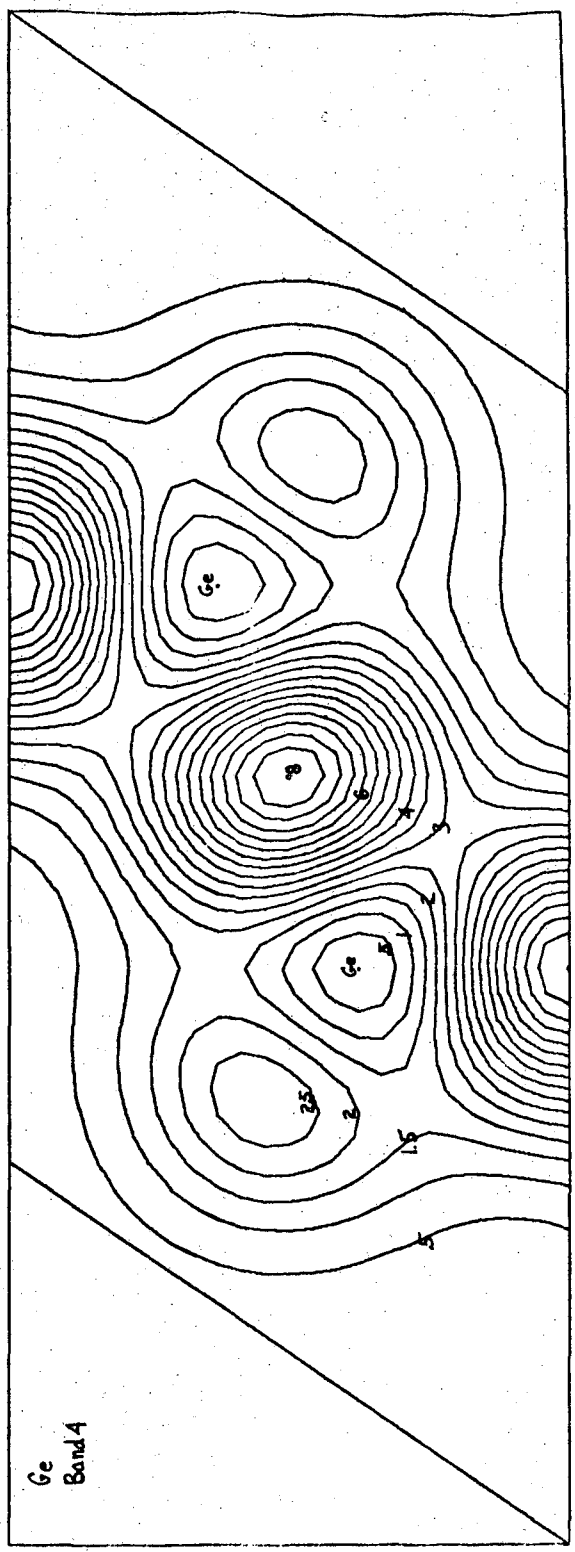

XBL 7011-6985

Figure 39

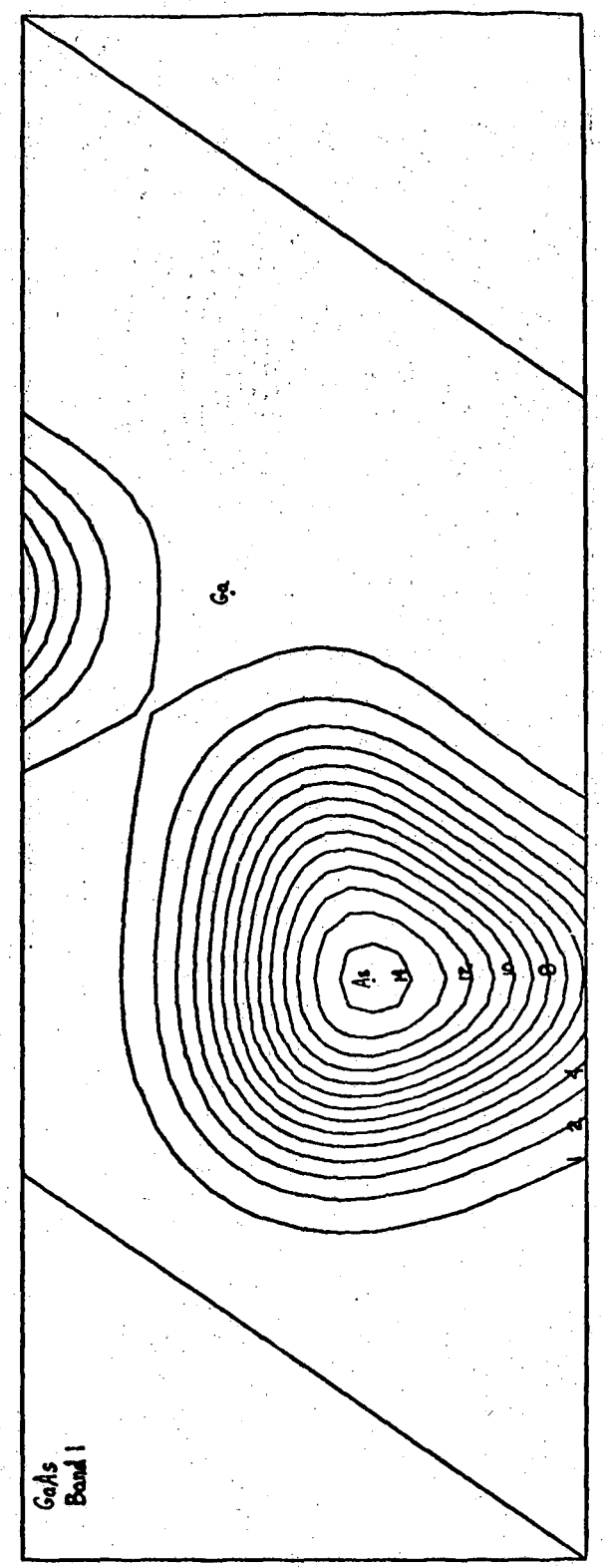

XBL 7011-6986

Figure 40

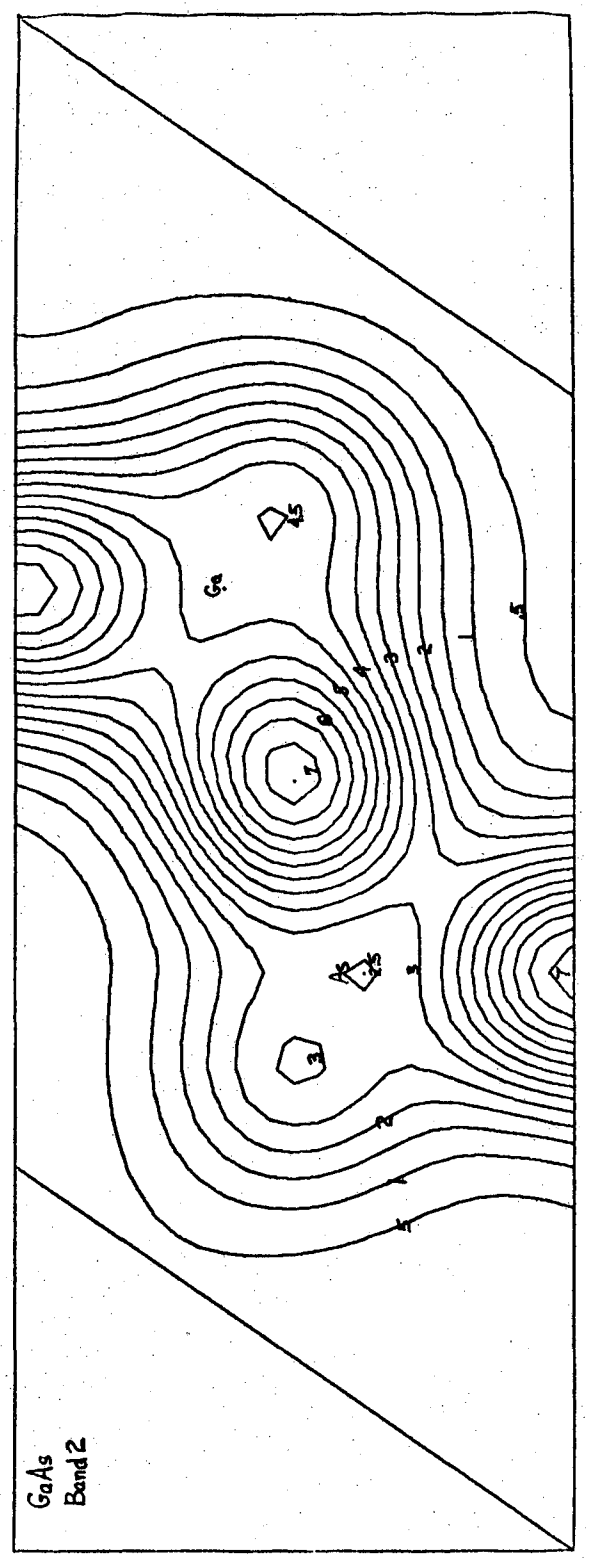

XBL 7011-6987

Figure 41

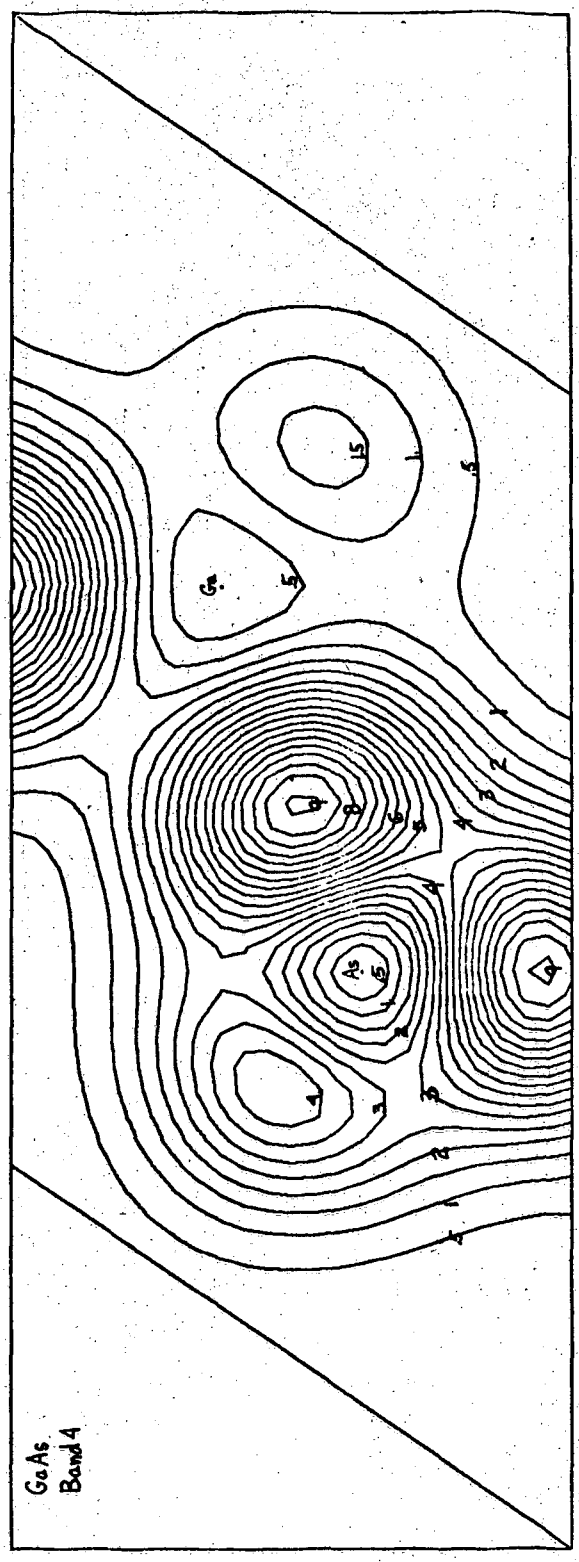

XBL 7011-6988

Figure 42

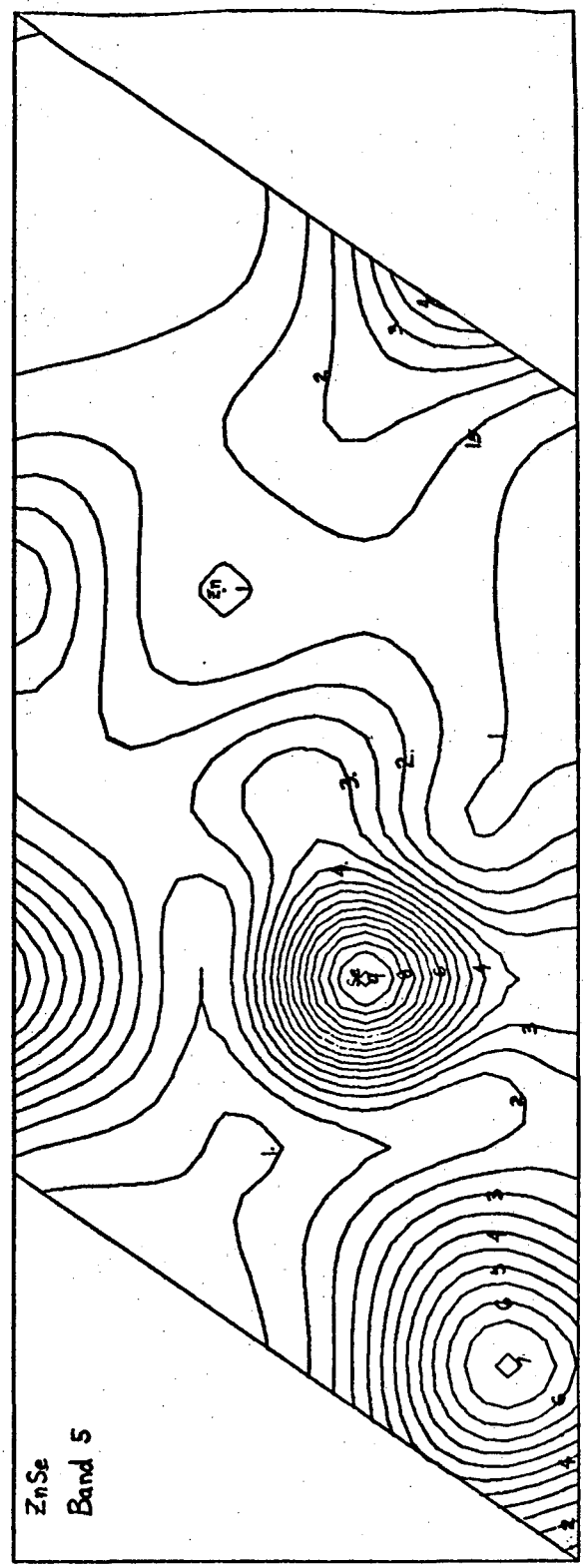

XBL 7011-6989

Figure 43

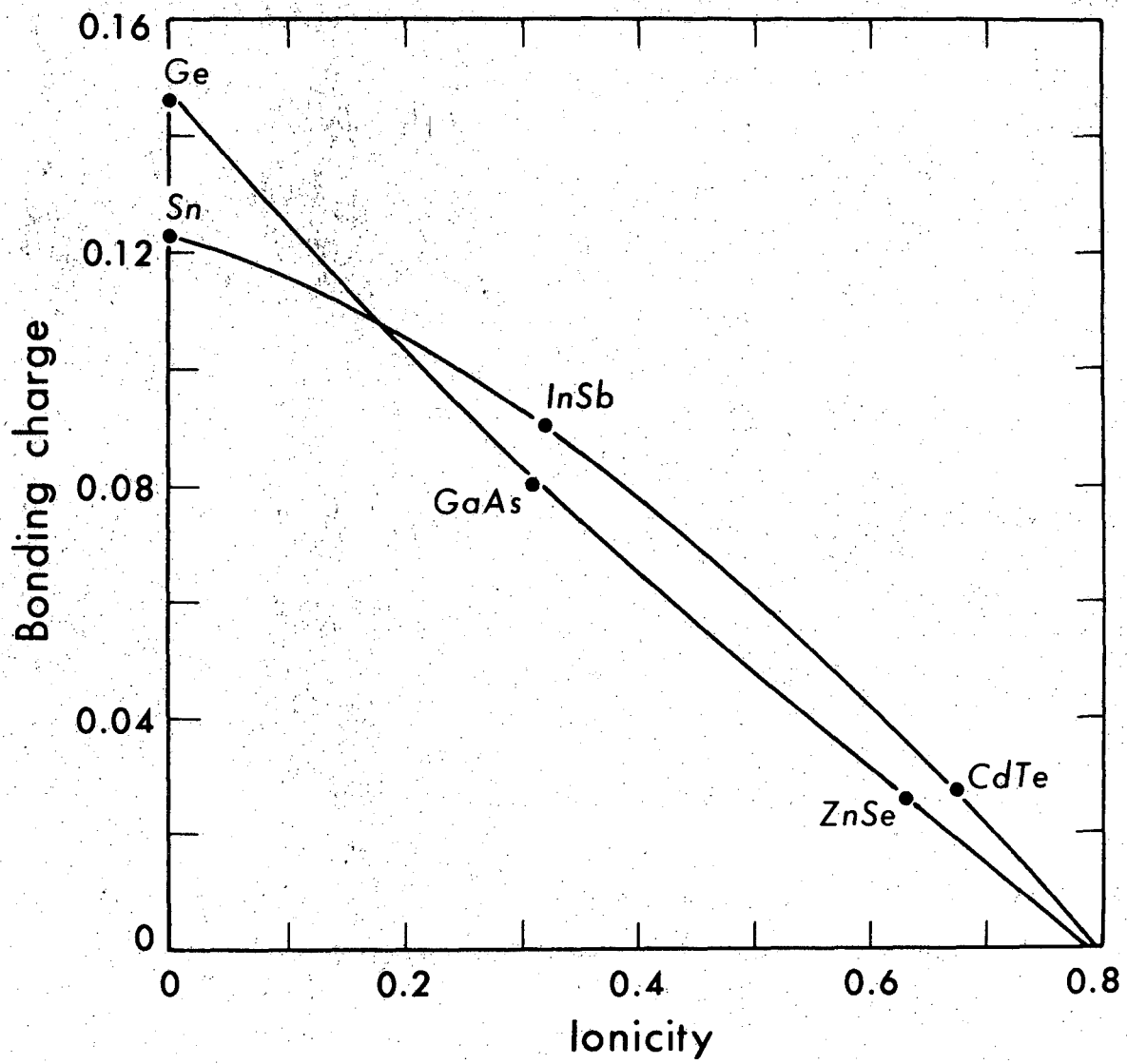

XBL 7011-7014

Figure 44

LEGAL NOTICE

TECHNICAL INFORMATION DIVISION
LAWRENCE RADIATION LABORATORY
UNIVERSITY OF CALIFORNIA
BERKELEY, CALIFORNIA 94720